

Mathematical Modelling of CD19 B Cell Reconstitution in  
Children After Insult to the Immune System

Soumya Perinparajah

A thesis submitted to University College London for the degree of

DOCTOR OF PHILOSOPHY

Infection, Immunity and Inflammation Research and Training Department

UCL Great Ormond Street Institute of Child Health

22 May 2023

I, Soumya Perinparajah, confirm that the work presented in this thesis is my own. Where information has been derived from other sources, I confirm that this has been indicated in the thesis.

# Abstract

An insult to the immune system is followed by a period of immune reconstitution. During recovery, patients are immunocompromised and susceptible to infection, and routine blood tests are performed for clinical monitoring. Children display heterogeneity in their recovery from such insults due to ongoing development and maturation. Non-linear mixed effects (NLME) modelling is widely used to fit a model to observed data (e.g., repeated measurements of a biomarker) related to co-variates. In addition, NLME models can be made mechanistic by incorporating prior knowledge to estimate biologically meaningful parameters.

In this thesis, mechanistic NLME models were constructed to quantify B cell reconstitution in children after four insults to the immune system: haematopoietic stem cell transplantation (HSCT), rituximab therapy for Epstein-Barr virus (EBV) reactivation post-HSCT, viral dynamics of EBV reactivation and rituximab biosimilar therapy for rheumatological disease.

A novel model of CD19<sup>+</sup> cell reconstitution post-HSCT was first constructed. To scale CD19<sup>+</sup> cell dynamics for age, prior biological knowledge was used to build a B cell maturation function. A Hill-type function was included to estimate the time delay between HSCT and bone marrow output of CD19<sup>+</sup> cells. The drug effect of rituximab was then incorporated to create a kinetic pharmacodynamic (K-PD) model to identify the pharmacodynamics of rituximab on B cell reconstitution post-HSCT in patients with EBV reactivation. In addition, a simplified version of the K-PD model was used to identify the pharmacodynamics of rituximab biosimilars on B cells. Finally, a modified version of a published human immunodeficiency virus (HIV) model was integrated with the rituximab K-PD model to create a new model quantifying the viral dynamics of EBV reactivation. Other analyses included developing a Cox proportional hazards model for time to first EBV reactivation event post-HSCT and sensitivity analysis of a previously reported EBV model.

# Impact Statement

After an insult to the immune system, it can take several years for immune system function to be restored. In the meantime, patients are immunocompromised and susceptible to infection. This research aimed to develop mathematical models to quantify B cell recovery in children following HSCT, the administration of drugs affecting the immune response and EBV reactivation. Whilst constructed using data from children, the scaling of age-related effects at the structural level of these models widens their scope for application across the age range including extrapolation to infants and adults. It is hoped that this work will ultimately contribute to the improvement of patients' health outcomes.

In Chapter 2, factors associated with CD19<sup>+</sup> cell recovery in children after HSCT were identified, which can inform the stratification of patients into those with good or poor CD19<sup>+</sup> cell reconstitution to guide treatment decisions. Another application of the model could be as a tool to predict individualised patient trajectories of CD19<sup>+</sup> cell reconstitution based on these factors thereby having implications for personalised medicine. For the models developed in Chapters 3, 4 and 5, their impact centres on their ability to now be used to simulate different clinical scenarios to inform optimal dosing for their respective indications. From the rituximab model developed in Chapter 3, simulations of varying dosing regimens of rituximab would provide simulated profiles of CD19<sup>+</sup> cell suppression over time for EBV reactivation post-HSCT. Similarly, using the rituximab biosimilar model in Chapter 5, simulations of varying dosing regimens of Truxima rituximab biosimilar can be performed to inform dose bioequivalence with rituximab for rheumatology indications. Lastly, simulations using the EBV viral dynamic model presented in Chapter 4 would reveal the interplay between the profiles of CD19<sup>+</sup> cell suppression and EBV VL over time.

In terms of disseminating research output, the results from the first part of Chapter 4, the Cox proportional hazards model of time to EBV reactivation in the first 100 days post-HSCT as well as the sensitivity analysis of a previously reported EBV viral kinetic model, have been published<sup>1</sup>. In addition, this doctoral work has been selected for both oral and poster presentation at the following conferences; the Lewis Sheiner Student Session at the Population Approach Group Europe meeting

in 2022 (oral), the Pharmacokinetics UK meetings in 2019 (poster) and 2020 (oral), the inaugural British Society for Immunology B Cell UK meeting in 2022 (poster) and the Great Ormond Street Hospital (GOSH) Conference 2019 (digital poster). Lastly, to promote open access and encourage further collaboration, model code will be made available on a suitable online platform.

# Acknowledgements

Firstly, I would like to thank my supervisors Professor Joe Standing, Professor Nigel Klein, Dr James Yates and Dr Amy Cheung. I have been incredibly fortunate to be your student. Your knowledge, guidance and patience have carried me through the past four years.

I would also like to thank the MRC and our industrial collaborator, AstraZeneca, for funding this work, as well as acknowledge the support of the UCL-Birkbeck Doctoral Training Programme. Thank you to James Yates for your supervision during my placement at AstraZeneca and to Amos Burke at Addenbrookes Hospital for your enthusiasm for this project.

This project would not have been possible without the patient data that were made available. Thank you to all the patients and their families who consented to share their data to enable this research project and to the GOSH Drive DRE team, in particular John Booth and Mohsin Shah, for extracting the data.

It has been an honour to study for a PhD at the UCL Great Ormond Street Institute of Child Health. I have collaborated with many clinicians and scientists as part of this work and for their time, collaboration and knowledge, I particularly thank: Juliana Silva, Reem Elfeky and the rest of the GOSH BMT Unit, Helen Payne for your seminal naive B cell output work, Oscar Charles and the London Pharmacometrics Interest Group.

I am grateful to have worked alongside so many wonderful colleagues and students. To all my office mates at ICH in room 646 and PUW141/142, Vania de Toledo and to all past and present members of the Standing Group, thank you for the good times shared together and for all your support.

To my friends, thank you for all your understanding and encouragement – see you all soon, I promise!

Finally, a special thank you to my family. Your sacrifices, perseverance, love and belief have allowed me to pursue this PhD journey. To my husband, Stefan - you have been unwavering throughout and you have come to my rescue countless times as I have worked on this PhD. I could not have done this without you. Thank you.

# Research Paper Declaration Form


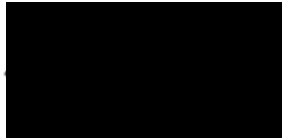
## UCL Research Paper Declaration Form: referencing the doctoral candidate's own published work(s)

Please use this form to declare if parts of your thesis are already available in another format, e.g. if data, text, or figures:

- have been uploaded to a preprint server;
- are in submission to a peer-reviewed publication;
- have been published in a peer-reviewed publication, e.g. journal, textbook.

*This form should be completed as many times as necessary. For instance, if you have seven thesis chapters, two of which containing material that has already been published, you would complete this form twice.*

<b>1. For a research manuscript that has already been published</b> (if not yet published, please skip to section 2):		
<b>a) Where was the work published?</b> (e.g. journal name)	Frontiers in Immunology	
<b>b) Who published the work?</b> (e.g. Elsevier/Oxford University Press):	Frontiers	
<b>c) When was the work published?</b>	12/07/2022	
<b>d) Was the work subject to academic peer review?</b>	Yes	
<b>e) Have you retained the copyright for the work?</b>	Yes	
[If no, please seek permission from the relevant publisher and check the box next to the below statement]:		
<input type="checkbox"/> I acknowledge permission of the publisher named under 1b to include in this thesis portions of the publication named as included in 1a.		
<b>2. For a research manuscript prepared for publication but that has not yet been published</b> (if already published, please skip to section 3):		
<b>a) Has the manuscript been uploaded to a preprint server?</b> (e.g. medRxiv):	Please select.	<b>If yes, which server?</b> Click or tap here to enter text.
<b>b) Where is the work intended to be published?</b> (e.g. names of journals that you are planning to submit to)	Click or tap here to enter text.	
<b>c) List the manuscript's authors in the intended authorship order:</b>	Click or tap here to enter text.	
<b>d) Stage of publication</b>	Please select.	

<b>3. For multi-authored work, please give a statement of contribution covering all authors (if single-author, please skip to section 4):</b>			
<p>Author list:  Soumya P. Kania (SPK), Juliana M. F. Silva (JMFS), Oscar J. Charles (OJC), John Booth (JoB), S.Y. Amy Cheung (SYAC), James W. T. Yates (JWTY), Austen Worth (AW), Judith Breuer (JB), Nigel Klein (NK), Persis J. Amrolia (PJA), Paul Veys (PV), Joseph F. Standing (JFS).</p> <p>SPK, SYAC, JWTY and JFS designed the study. JMFS, AW, PJA and PV collected the data. JBo extracted the data. SPK, JMFS and OJC analysed the data. SPK, JMFS, OJC, SYAC, JWTY, JBr, NK and JFS interpreted the data and wrote the manuscript. All authors contributed to the article and approved the submitted version.</p>			
<b>4. In which chapter(s) of your thesis can this material be found?</b>			
Chapter 4: Dynamics of EBV Reactivation in Children Post-HSCT			
<b>5. e-Signatures confirming that the information above is accurate (this form should be co-signed by the supervisor/ senior author unless this is not appropriate, e.g. if the paper was a single-author work):</b>			
<b>Candidate:</b>	 Soumya Perinparajah	<b>Date:</b>	22/12/2022
<b>Supervisor/ Senior Author (where appropriate):</b>	 Joseph F. Standing	<b>Date:</b>	22/12/2022



# Other Scientific Contributions

In addition to the work presented in this thesis and the research paper declared above, I have been involved in the following publications whilst studying for the degree of Doctor of Philosophy.

- Elfeky R, Builes N, **Perinparajah S**, Standing J, Chiesa R, Lucchini G, Lazareva A, Gabelli M, Amrolia P, Rao K. O155 The Great Ormond Street (GOS) Paediatric Co-Morbidity Score for Outcome Post-Hematopoietic Stem Cell Transplantation. The 46<sup>th</sup> Annual Meeting of the European Society for Blood and Marrow Transplantation: Physicians Oral Session (O010-O173). *Bone Marrow Transplant* **55**, 158–159 (2020). doi: 10.1038 / s41409-020-01119-3.
- **Perinparajah S**, Silva J, Worth A, *et al.* 126 Pharmacodynamics of rituximab on B cells in paediatric post-HSCT patients with EBV. *Archives of Disease in Childhood* 2019; 104:A50

# List of Abbreviations

---

AAV	ANCA-associated vasculitis
AIC	Akaike Information criterion
ALC	Absolute lymphocyte count
ANCA	Anti-neutrophil cytoplasmic antibody
APC	Antigen presenting cell
ATG	Anti-thymocyte globulin
AUC	Area under curve
BAL	B-cell acute lymphoma
BCR	B cell receptor
BL	Burkitt Lymphoma
BLQ	Below limit of quantification
BMT	Bone marrow transplant
BSV	Between subject variability
CBT	Cord blood transplant
CD4	Cluster of Differentiation 4
CD8	Cluster of Differentiation 8
CD19	Cluster of Differentiation 19
CD20	Cluster of Differentiation 20
CD27	Cluster of Differentiation 27
CHOP	Cyclophosphamide, doxorubicin, vincristine and prednisolone
CI	Confidence Interval
CLL	Chronic lymphocytic leukaemia
CMV	Cytomegalovirus
Ct	Cycle threshold
CTL	Cytotoxic T cell
CWRES	Conditionally weighted residuals

---

DAS28	Disease Activity Score using 28 joints
DLBCL	Diffuse large B cell lymphoma
DNA	Deoxyribonucleic acid
DRE	Digital Research Environment
DV	Dependent variable
EBMT	European Society for Blood and Marrow Transplantation
EBV	Epstein-Barr virus
EMA	European Medicines Agency
EULAR	European League Against Rheumatism
FDA	Food and Drug Administration
G-CSF	Granulocyte colony-stimulating factor
GOSH	Great Ormond Street Hospital
GPA	Granulomatosis with polyangitis
GvHD	Graft versus host disease
Haplo	Haploidentical
HCV	Hepatitis C virus
HHV	Human herpes virus
HSC	Haematopoietic stem cell
HSCT	Haematopoietic stem cell transplant
HIV	Human immunodeficiency virus
HLA	Human leukocyte antigen
HR	Hazard ratio
HTLV-1	Human T cell leukaemia virus
Ig	Immunoglobulin
IIV	Inter individual variability
IPRED	Individual prediction
IR	Immune reconstitution
IVIg	Intravenous immunoglobulin
K-PD	Kinetic-pharmacodynamic
KREC	Kappa-deleting recombination excision circle
LLOQ	Lower limit of quantification
MAC	Myeloablative conditioning
MALT	Mucosa-associated lymphoid tissue
MHC	Major histocompatibility complex
MIC	Minimal intensity conditioning
MFD	Matched familial donor

---

MH	Malignant haematological
MMFD	Mismatched familial donor
MMUD	Mismatched unrelated donor
MPA	Microscopic polyangitis
MSD	Matched sibling donor
MUD	Matched unrelated donor
NHL	Non-Hodgkin's B cell lymphoma
NHS	National Health Service
NLME	Non-linear mixed effects
NMH	Non-malignant haematological
NONMEM	Non-linear mixed effects modelling
ODE	Ordinary differential equation
OFV	Objective function value
PBSCT	Peripheral blood stem cell transplant
PBPK	Physiologically based pharmacokinetic
pcVPC	Prediction-corrected visual predictive check
PD	Pharmacodynamic
PH	Proportional hazards
PID	Primary immunodeficiency
PK	Pharmacokinetic
popPK	Population pharmacokinetic
PKPD	Pharmacokinetic-pharmacodynamic
PRED	Population prediction
PsN	Perl-speaks-NONMEM
PTLD	Post-transplant lymphoproliferative disorder
PV	Pemphigus vulgaris
qPCR	quantitative polymerase chain reaction
RA	Rheumatoid arthritis
REC	Research Ethics Committee
RIC	Reduced intensity conditioning
RMSD	Root mean squared distance
RSE	Relative standard error
RTX	Rituximab
SARS-CoV-2	Severe acute respiratory syndrome-coronavirus 2
SCID	Severe combined immunodeficiency
SCM	Stepwise covariate modelling

---

TCR	T cell receptor
TREC	T cell receptor excision circle
TV	Typical value
VD	Viral dynamic
VDJ	Variability, diversity and joining
VK	Viral kinetic
VL	Viral load
VPC	Visual predictive check

---

# Contents

<b>Abstract</b>	<b>2</b>
<b>Impact Statement</b>	<b>3</b>
<b>Acknowledgements</b>	<b>5</b>
<b>Research Paper Declaration Form</b>	<b>6</b>
<b>Other Scientific Contributions</b>	<b>8</b>
<b>List of Abbreviations</b>	<b>9</b>
<b>1 Introduction</b>	<b>26</b>
1.1 The Haematopoietic System . . . . .	26
1.2 The Immune System . . . . .	27
1.3 B Cells . . . . .	28
1.4 Insult to the Immune System . . . . .	29
1.5 Haematopoietic Stem Cell Transplantation . . . . .	29
1.5.1 Indications . . . . .	29
1.5.2 Types of HSCT . . . . .	30
1.5.3 Pre-HSCT Conditioning . . . . .	31
1.5.4 Post-HSCT Clinical Outcomes . . . . .	31

<i>CONTENTS</i>	14
1.6 Immune Reconstitution . . . . .	32
1.7 Mathematical Modelling . . . . .	33
1.7.1 Concepts . . . . .	33
1.7.2 Pharmacometrics . . . . .	34
1.8 Mathematical Modelling of Immune Reconstitution . . . . .	35
1.9 Research Aims . . . . .	36
<b>2 B Cell Reconstitution After HSCT</b>	<b>37</b>
2.1 Introduction . . . . .	37
2.1.1 B Cell Reconstitution . . . . .	37
2.1.2 Bone Marrow Output . . . . .	38
2.1.3 Scaling . . . . .	39
2.1.4 Aim . . . . .	39
2.1.5 Objectives . . . . .	39
2.2 Methods . . . . .	40
2.2.1 Ethics Statement . . . . .	40
2.2.2 Data . . . . .	40
2.2.3 Non-linear Mixed Effects Modelling . . . . .	41
2.2.4 Model Building . . . . .	44
2.2.5 Software . . . . .	50
2.3 Results . . . . .	50
2.3.1 Patient Characteristics . . . . .	50
2.3.2 Structural Model . . . . .	51
2.3.3 Model Fitting . . . . .	53
2.3.4 Parameter Estimates . . . . .	53
2.3.5 Covariate Effects . . . . .	54
2.3.6 Model Evaluation . . . . .	56
2.4 Discussion . . . . .	61

<i>CONTENTS</i>	15
<b>3 Rituximab Pharmacodynamics in EBV Reactivation</b>	<b>65</b>
3.1 Introduction . . . . .	65
3.1.1 Epstein-Barr Virus . . . . .	65
3.1.2 EBV Reactivation . . . . .	66
3.1.3 Rituximab . . . . .	67
3.1.4 Aim . . . . .	71
3.1.5 Objectives . . . . .	71
3.2 Methods . . . . .	71
3.2.1 Data . . . . .	71
3.2.2 Rituximab Therapy . . . . .	72
3.2.3 Incorporating Rituximab Effect . . . . .	73
3.3 Results . . . . .	74
3.3.1 Patient Characteristics . . . . .	74
3.3.2 Model Fitting . . . . .	76
3.3.3 Parameter Estimates . . . . .	77
3.3.4 Covariate Effects . . . . .	78
3.3.5 Model Evaluation . . . . .	79
3.4 Discussion . . . . .	82
<b>4 Dynamics of EBV Reactivation After HSCT</b>	<b>88</b>
4.1 Introduction . . . . .	88
4.1.1 Viral Dynamic Models . . . . .	88
4.1.2 EBV Dynamic Models . . . . .	89
4.1.3 Aims . . . . .	91
4.1.4 Objectives . . . . .	91
4.2 Methods . . . . .	92
4.2.1 Data . . . . .	92



<i>CONTENTS</i>	16
4.2.2 EBV Viraemia and Rituximab Therapy . . . . .	93
4.2.3 Cox Proportional Hazards Model . . . . .	93
4.2.4 Sensitivity Analysis . . . . .	96
4.2.5 Viral Dynamic Model Building . . . . .	99
4.3 Results . . . . .	101
4.3.1 Patient Characteristics . . . . .	101
4.3.2 Clinical Outcomes . . . . .	102
4.3.3 Cox-PH Model . . . . .	103
4.3.4 Sensitivity Analysis . . . . .	108
4.3.5 Viral Dynamic Model . . . . .	108
4.4 Discussion . . . . .	115
<b>5 Rituximab Biosimilar Pharmacodynamics in Rheumatology</b>	<b>124</b>
5.1 Introduction . . . . .	124
5.1.1 Biosimilars . . . . .	124
5.1.2 Rituximab Biosimilars . . . . .	125
5.1.3 Aim . . . . .	127
5.1.4 Objectives . . . . .	127
5.2 Methods . . . . .	127
5.2.1 Data . . . . .	127
5.2.2 Rituximab and Biosimilar Administration . . . . .	129
5.2.3 Model . . . . .	129
5.3 Results . . . . .	129
5.3.1 Patient Characteristics . . . . .	129
5.3.2 Model Fitting . . . . .	130
5.3.3 Parameter Estimates . . . . .	132
5.3.4 Model Evaluation . . . . .	133
5.4 Discussion . . . . .	133

<i>CONTENTS</i>	17
<b>6 Conclusions</b>	<b>138</b>
6.1 Future Work . . . . .	139
<b>References</b>	<b>141</b>

# List of Figures

2.1	Flow diagram of study patients. GOSH, Great Ormond Street Hospital; BMT, Bone Marrow Transplant; EBV, Epstein-Barr virus; HSCT, Haematopoietic stem cell transplant. . . . .	41
2.2	Decrease in absolute number of CD27- IgD+ naive B cells (per microlitre blood) with age. Data points extracted from Morbach <i>et al</i> <sup>54</sup> , blue line is the local regression curve and grey area is the 95% confidence interval. . . . .	47
2.3	Decline in fraction of naive B cells expressing Ki67 with age in healthy South African children. Data from Payne <i>et al</i> <sup>146</sup> , blue line is local regression curve and grey area is 95% confidence interval. . . . .	48
2.4	Raw data used for model-building. Each coloured line is an individual patient and the black dotted line represents the LLOQ of the assay used to measure CD19 <sup>+</sup> cell counts ( $10 \times 10^6$ cells/L). The thick black line is the local regression curve, and the grey shaded area is the 95% confidence interval. . . . .	52
2.5	Schematic of final model of CD19 <sup>+</sup> cell reconstitution. The central compartment represents the concentration of CD19 <sup>+</sup> cells as measured in the peripheral blood at time $t$ (days) after HSCT. New B cells produced by the bone marrow enter at zero-order rate $\lambda$ and die at first-order rate $\mu$ . The B cell maturation function was applied to $\lambda$ and $\mu$ to scale for age-related effects, and a sigmoidal Hill-type function was used to account for the delay in bone marrow output after HSCT. . . . .	53
2.6	Proportion of thymic output/bone marrow output with time since HSCT. Blue line represents bone marrow output using Hill-type delay function in current model of CD19 <sup>+</sup> cell reconstitution post-HSCT and red line represents thymic output using Hoare function in model of CD4 <sup>+</sup> T cell reconstitution post-HSCT <sup>106</sup> . . . . .	55

2.7	Goodness-of-fit plots. A) Observed CD19 <sup>+</sup> cell counts vs Population Predicted CD19 <sup>+</sup> cell counts. B) Observed CD19 <sup>+</sup> cell counts vs Individual Predicted CD19 <sup>+</sup> cell counts. C) CWRES vs Time. D)  IWRES  vs Individual Predicted CD19 <sup>+</sup> cell counts. Blue lines are the local regression curves and red datapoints are those that were BLQ. . . . .	58
2.8	Prediction-corrected Visual Predictive check for final model stratified by age groups in order of infants, children and adolescents. Black dots are observed data and the solid red line is the observed median. The dotted red lines are the observed 2.5th, 50th and 97.5th percentiles and the grey shaded area are the 95% prediction intervals. The bottom part of the panel shows the proportion of the total data that were BLQ.	59
3.1	Chimeric structure of rituximab. CD20 <sup>+</sup> , cluster of differentiation 20; IgG, immunoglobulin G. . . . .	69
3.2	Flow diagram of study patients. Box in blue represents patients considered for current study (n = 59). GOSH, Great Ormond Street Hospital; BMT, Bone Marrow Transplant; EBV, Epstein-Barr virus; HSCT, Haematopoietic stem cell transplant. .	72
3.3	Raw data used for model-building (n = 55). Each coloured line is an individual patient and the black dotted line represents the LLOQ of the assay used to measure CD19 <sup>+</sup> cell counts (10 x 10 <sup>6</sup> cells/L). The thick black line is the local regression curve, and the grey shaded area is the 95% confidence interval . . . . .	76
3.4	Schematic of kinetic-pharmacodynamic model of rituximab. First compartment represents the serum compartment for rituximab dosing by intravenous infusion, where rituximab decays at rate $k_e$ and is assumed to increase CD19 <sup>+</sup> cell death rate, $\mu$ , denoted by '+' sign. Second compartment represents CD19 <sup>+</sup> cells produced by the bone marrow at zero-order rate $\lambda$ and dying at first -order rate $\mu$ . A B cell maturation function was applied to $\lambda$ and $\mu$ to scale for age-related effects, and a sigmoidal Hill-type function was used to account for the delay in bone marrow output after HSCT. . . . .	77
3.5	Goodness-of-fit plots. A) Observed CD19 <sup>+</sup> cell counts vs Population Predicted CD19 <sup>+</sup> cell counts. B) Observed CD19 <sup>+</sup> cell counts vs Individual Predicted CD19 <sup>+</sup> cell counts. C) CWRES vs Time. D)  IWRES  vs Individual Predicted CD19 <sup>+</sup> cell counts. Black lines are lines of unity, blue lines are the local regression curves and red datapoints are those that were BLQ. . . . .	80

3.6	Visual predictive check of final rituximab model. Black dots are observed data and the solid red line is the observed median. The dotted red lines are the observed 2.5th, 50th and 97.5th percentiles and the grey shaded area are the 95% prediction intervals. The bottom panel shows the proportion of total data that were BLQ. . . . .	81
4.1	Flow diagram of study patients. Box in blue represents patients in current study ( $n = 59$ ). GOSH, Great Ormond Street Hospital; BMT, Bone Marrow Transplant; EBV, Epstein-Barr virus; HSCT, Haematopoietic stem cell transplant. . . . .	92
4.2	$AUC_{0-100}$ for $CD19^+$ cells for one patient. Black dots represent measurements of $CD19^+$ cells at 21, 43 and 78 days post-HSCT. Zero $CD19^+$ cells were assumed to be present at day 0 (day of HSCT). Pink shaded region is the AUC calculated using the trapezoidal rule. . . . .	94
4.3	Schematic of Akinwumi model of EBV kinetics <sup>320</sup> . Blue boxes are B cell compartments, orange boxes are CTL compartments. CTL, cytotoxic T cell. . . . .	96
4.4	Violin plot of median peak EBV VL stratified by number of rituximab doses received. Black horizontal line represents median peak EBV VL for the dose number and box represents interquartile range. Black dots represent median peak EBV VLs lying outside the interquartile range and coloured shape represents the distribution of the data. . . . .	103
4.5	EBV VL against time since EBV reactivation, stratified by early CD4 T cell reconstitution, as defined by Admiraal <i>et al</i> <sup>49</sup> . Curves are from spline regression (2df) of EBV VL with time, with VL measurements normalised to two weeks before EBV reactivation. Points are an individual patient's measured VL and grey shaded region signifies VL measurements below 40,000 copies/mL, the threshold to treat with rituximab. . . . .	104
4.6	Kaplan-Meier curves of cumulative fraction of patients with EBV reactivation in first 100 days post-HSCT stratified by type of serotherapy (ATG or alemtuzumab) and EBV serostatus of recipient (negative or positive). P values were calculated using the log-rank test and denote the difference between the two subgroups. Shaded regions show 95% confidence interval. . . . .	107
4.7	Plot to show sensitivity of parameters when parameter value is set to 10, evaluated using RMSD. Log RMSD has been plotted for presentation purposes. RMSD, root mean squared distance. . . . .	109

- 4.8 Simulated EBV VL trajectories, using  $B_m$  compartment as a proxy for EBV VL. Sensitivity of EBV VL shown for the variation of six parameters over the range of values 0.00001-1000, where  $\beta$  parameter represents reference model fit and all other parameters are sensitive parameters. B, one billion; M, one million; K, 1000. . . . . 110
- 4.9 Schematic of model of EBV dynamics and CD19<sup>+</sup> cell dynamics post-HSCT. . . . . 110
- 4.10 Raw EBV VL measurements in viral dynamic model-building dataset ( $n = 30$ ). Each coloured line represents EBV VL trajectory for an individual patient. The black dotted line is the LLOQ of the assay used to measure EBV VL (200 copies/mL). The thick black line is the local regression curve, and the grey shaded area is the 95% confidence interval. X-axis shows time since HSCT (days). . . . . 111
- 4.11 Raw data used for building viral dynamic model. Each coloured line is an individual patient and the black dotted line represents LLOQ of the EBV VL assay (200 copies/mL). The thick black line is the local regression curve, and the grey shaded area is the 95% confidence interval. X-axis shows time since EBV reactivation, where each patient's VL measurements were normalised to the start of their reactivation event. . . . . 112
- 4.12 Individual trajectories of EBV VL, CD19<sup>+</sup> cell and CD4<sup>+</sup> cell counts and rituximab dosing for 16 patients. Black line is EBV VL, blue line is CD19<sup>+</sup> cell count, brown line is CD4<sup>+</sup> cell count and black dots indicate rituximab administrations. Dotted black line represents the lower limit of detection of the EBV VL assay (200 copies/mL). CD4<sup>+</sup> cell counts were predicted using a published PD model for CD4<sup>+</sup> cell reconstitution post-HSCT in children<sup>106</sup> and CD19<sup>+</sup> cell counts were predicted using the Chapter 3 K-PD model for the effect of rituximab on CD19<sup>+</sup> cell reconstitution post-HSCT in children. For EBV VL, observed measurements spanning from three weeks pre- to seven weeks post-HSCT were plotted, and were linearly interpolated to obtain a continuous range of data points for 0-100 days post-HSCT. In the absence of a published mathematical model for CD8<sup>+</sup> cell reconstitution post-HSCT and a sparsity of observed CD8<sup>+</sup> cell counts disabling linear interpolation, CD8<sup>+</sup> cell counts were not visualised. . . . . 113
- 4.13 Goodness-of-fit plots for EBV viral dynamic model. A) Observed EBV VL vs Population Predicted EBV VL. B) Observed EBV VL vs Individual Predicted EBV VL. C) CWRES vs Time after HSCT. D) |IWRES| vs Individual Predicted EBV VL. Blue lines are the local regression curves and red data points are EBV VL measurements that were BLQ. . . . . 116

- 4.14 Prediction-corrected Visual Predictive check for viral dynamic model. Black dots are observed EBV VLs and the solid red line is the observed median. The dotted red lines are the observed 2.5th, 50th and 97.5th percentiles and the grey shaded area are the 95% prediction intervals. The bottom panel shows the proportion of total data that were BLQ. . . . . 117
- 5.1 Flow diagram of study patients. EBV, Epstein-Barr virus; HSCT, Haematopoietic stem cell transplant; mAb, Monoclonal antibody. . . . . 128
- 5.2 Raw data used for model-building ( $n = 25$ ). Each coloured line is an individual patient and the black dotted line represents the LLOQ of the assay used to measure CD19<sup>+</sup> cell counts ( $10 \times 10^6$  cells/L). The thick black line is the local regression curve, and the grey shaded area is the 95% confidence interval. . . . . 131
- 5.3 Goodness-of-fit plots. A) Observed CD19<sup>+</sup> cell counts vs Population Predicted CD19<sup>+</sup> cell counts. B) Observed CD19<sup>+</sup> cell counts vs Individual Predicted CD19<sup>+</sup> cell counts. C) CWRES vs Time after first dose/observation. D) |IWRES| vs Individual Predicted CD19<sup>+</sup> cell counts. Black lines are lines of unity, blue lines are the local regression curves and red datapoints are those that were BLQ. . . . . 134
- 5.4 Prediction-corrected Visual predictive check of rituximab biosimilars model. Black dots are observed data and the solid red line is the observed median. The dotted red lines are the observed 2.5th, 50th and 97.5th percentiles and the grey shaded area are the 95% prediction intervals. The bottom panel shows the proportion of total data that were BLQ. . . . . 135

# List of Tables

2.1	Models tested for B cell maturation function. $w(t)$ is the naive B cell count per $\mu L$ blood at age $t$ . $z(t)$ denotes the fraction of naive B cells expressing Ki67 at age $t$ . . .	49
2.2	Functions tested to estimate delay in recovery of bone marrow output of CD19 <sup>+</sup> cells after HSCT. . . . .	49
2.3	Patient characteristics for model-building dataset for CD19 <sup>+</sup> cell model. PID, primary immunodeficiency; NMH, non-malignant haematological ; MH, malignant haematological; BM, bone marrow; PBSC, peripheral blood stem cell; CB, cord blood; MAC, myeloablative conditioning ; MIC, minimal intensity conditioning; RIC, reduced intensity conditioning. . . . .	51
2.4	Estimated parameter values. Setpoint parameter derived by dividing $\lambda$ by $\mu$ . $\lambda$ , CD19 <sup>+</sup> cell production rate constant; $\mu$ , CD19 <sup>+</sup> cell death rate constant; $\gamma$ , Steepness of slope of CD19 <sup>+</sup> cell recovery; $T_{50}$ , Time to half-maximal output of CD19 <sup>+</sup> cells from bone marrow; RSE, relative standard error; BSV, between-subject variability; CI, confidence interval. . . . .	54
2.5	Covariate effects identified using SCM. PID, primary immunodeficiency; MAC, myeloablative conditioning; RSE, relative standard error; CI, confidence interval. . .	56
3.1	Current licensure for rituximab. EMA, European Medicines Agency; FDA, Food and Drug Administration. NHL, Non-Hodgkin's B cell lymphoma; CLL, Chronic lymphocytic leukaemia; RA, Rheumatoid arthritis; MPA, Microscopic polyangitis; GPA, Granulomatosis with polyangitis; PV, Pemphigus vulgaris; DLBCL, Diffuse large B cell lymphoma; BL, Burkitt's lymphoma; BAL, B-cell acute lymphoma. . . .	67
3.2	Patient and transplant characteristics for model-building dataset for rituximab model. * denotes one patient who did not receive serotherapy. . . . .	75



3.3	Estimated parameter values. Setpoint parameter was derived by dividing $\lambda$ by $\mu$ . $\lambda$ , CD19 <sup>+</sup> cell production rate constant; $\mu$ , CD19 <sup>+</sup> cell death rate constant; $\gamma$ , Steepness of slope of CD19 <sup>+</sup> cell recovery; $T_{50}$ , Time to half-maximal output of CD19 <sup>+</sup> cells from bone marrow; $k_e$ , Rituximab elimination rate constant; $E_{max}$ , Apparent maximum killing effect of rituximab on CD19 <sup>+</sup> cells; $ED_{50}$ , Rituximab dose producing 50% of apparent maximum killing effect; RSE, relative standard error; BSV, between-subject variability; CI, confidence interval. . . . .	78
3.4	Covariate effects identified using SCM. $T_{50}$ , Time to half-maximal output of CD19 <sup>+</sup> cells from bone marrow; PID, primary immunodeficiency; MAC, myeloablative conditioning; RSE, relative standard error; CI, confidence interval. . . . .	79
4.1	Collinearity diagnostics for covariates during Cox-PH model building. ATG, anti-thymocyte globulin; AUC, area under the curve; ALC, absolute lymphocyte count; IR, immune reconstitution, RTX, rituximab. Early IR of all immune cell subsets was calculated using previously defined threshold of early immune reconstitution, $\geq 50 \times 10^6$ cells/L <sup>66</sup> . . . . .	95
4.2	Parameter values used to obtain reference fit of Akinwumi model. <sup>a</sup> Assumption; parameters are measured per week expect for $n$ and $\beta$ that are dimensionless. . . .	97
4.3	Patient and transplant characteristics for model-building datasets for Cox-PH model and NLME Model.* denotes one patient who did not receive serotherapy in the dataset for the Cox-PH model. Of the 38 patients who had EBV reactivation in the first 100 days post-HSCT, eight patients were excluded from the viral dynamic model dataset as they did not receive rituximab in the first 100 days post-HSCT. . .	101
4.4	Univariate Cox-PH model for time to first EBV reactivation in first 100 days post-HSCT. PID, primary immunodeficiency; HSC, haematopoietic stem cell; PBSC, peripheral blood stem cell; BM, bone marrow; EBV, Epstein-Barr virus; $AUC_{0-100}$ , area under the curve from day of HSCT to 100 days post-HSCT; ALC, absolute lymphocyte count; MSD, matched sibling donor; MFD, matched familial donor; MUD, matched unrelated donor; MMFD, mismatched familial donor; MMUD, mismatched unrelated donor; Haplo, haploidentical donor; MAC, myeloablative conditioning; MIC, minimal-intensity conditioning; RIC, reduced-intensity conditioning; ATG, anti- thymocyte globulin. HR, hazard ratio; CI, confidence interval. – denotes a continuous variable. . . . .	105

- 4.5 Multivariate Cox-PH model for time to first reactivation in first 100 days post-HSCT. PID, primary immunodeficiency; HSC, haematopoietic stem cell; PBSC, peripheral blood stem cell; BM, bone marrow; EBV, Epstein-Barr virus;  $AUC_{0-100}$ , area under the cell-time curve from 0-100 days post-HSCT; ATG, anti- thymocyte globulin. HR, hazard ratio; CI, confidence interval. – denotes a continuous variable. . . . . 106
- 4.6 Estimated parameter values from EBV viral dynamic model.  $\lambda$ , CD19<sup>+</sup> cell production rate constant;  $\mu$ , CD19<sup>+</sup> cell death rate constant;  $\gamma$ , Steepness of slope of CD19<sup>+</sup> cell recovery;  $T_{50}$ , Time to half-maximal output of CD19<sup>+</sup> cells from bone marrow;  $k_e$ , Rituximab elimination rate constant;  $E_{max}$ , Maximum killing effect of rituximab on CD19<sup>+</sup> cells;  $ED_{50}$ , Rituximab dose producing 50% of maximum killing effect;  $k$ , Infected CD19<sup>+</sup> cell production rate constant;  $\delta$ , Infected CD19<sup>+</sup> cell death rate constant;  $q$ , CTL killing rate of infected cells;  $N$ , Viral burst size;  $c$ , Viral clearance rate;  $r$ , CTL proliferation rate constant;  $d$ , CTL death rate constant; RSE, relative standard error; BSV, between-subject variability; CI, confidence interval. . . . . 114
- 5.1 Current licensure for rituximab biosimilars. EMA, European Medicines Agency; FDA, Food and Drug Administration. NHL, Non-Hodgkin's B cell lymphoma; CLL, Chronic lymphocytic leukaemia; RA, Rheumatoid arthritis; MPA, Microscopic polyangitis; GPA, Granulomatosis with polyangitis; PV, Pemphigus vulgaris. . . . 125
- 5.2 Patient characteristics for model-building dataset for rituximab biosimilars model. All patients received rituximab biosimilar. \* denotes 4 patients who received reference rituximab as well as rituximab biosimilar. . . . . 130
- 5.3 Estimated parameter values. Setpoint, number of CD19<sup>+</sup> cells at steady state in absence of rituximab biosimilar derived by  $\lambda$  divided by  $\mu$ ;  $\lambda$ , CD19<sup>+</sup> cell production rate constant;  $\mu$ , CD19<sup>+</sup> cell death rate constant;  $k_e$ , elimination rate constant of rituximab biosimilar;  $E_{max}$ , maximum killing effect of rituximab biosimilar on CD19<sup>+</sup> cells;  $ED_{50}$ , rituximab biosimilar dose producing 50% of maximum killing effect. . . 132

# Chapter 1

## Introduction

### 1.1 The Haematopoietic System

The haematopoietic system is comprised of the tissues and organs responsible for producing all the blood and immune cells required by the human body. In a life-long process called haematopoiesis, starting during embryonic development and continuing throughout adulthood, blood stem cells known as haematopoietic stem cells (HSCs) proliferate and differentiate into a range of cellular components that defend the body against infection and disease<sup>2</sup>. Haematopoiesis encompasses the formation and maturation of HSCs, as well as their activation and proliferation. The major sites of haematopoiesis are in the primary lymphoid organs, the bone marrow and the thymus, in secondary lymphoid organs which include the spleen and lymph nodes, and peripheral organs such as mucosa-associated lymphoid tissue (MALT)<sup>3</sup>. As well as providing the anatomical space for the process, the specialised microenvironment of these sites make up the HSC niche, acting as the “soil” for haematopoiesis<sup>4</sup>. Key components include cytokines such as growth factors, the presence of various haematopoietic and non-haematopoietic cells in the stroma, blood vessels and nerve fibres<sup>5,6</sup>. The two cornerstones of HSCs are their properties of self-renewal and multipotency<sup>7</sup>. They differentiate in the bone marrow into multi-potent progenitor cells then into either common myeloid progenitor cells or common lymphoid progenitor cells, which give rise to cells of myeloid and lymphoid lineage respectively. Cells of myeloid lineage consist of erythrocytes, platelets and a range of immune cells, which are described in the next section. Erythrocytes transport oxygen to tissues and organs around the body, and platelets work with proteins in blood plasma to form blood clots<sup>8</sup>. Cells of lymphoid lineage include natural killer cells, T lymphocytes and B lymphocytes (more commonly known as T cells and B cells), which together provide cell-mediated immunity and antibody-mediated immunity<sup>9</sup>.

The cells formed downstream of the common myeloid and lymphoid progenitor cells, that make up the immune system, are introduced below.

## 1.2 The Immune System

Myeloid cells constitute the innate arm of the immune system conferring short-term immunity, as they respond quickly to provide a non-specific immune response against pathogens. These include neutrophils and a range of other phagocytes such as basophils, eosinophils, mast cells and macrophages<sup>10</sup>. These cell subsets can reside in tissue, circulate in the blood or circulate in the lymphatic system<sup>8</sup>. In conjunction with the complement system, the primary role of myeloid cells is to engulf and ingest antigens to kill them or process them for antigen presentation to T cells<sup>8</sup>. Lymphoid cells make up the adaptive arm of the immune system responsible for conferring long-term, or acquired, immunity against pathogens due to their unique ability to develop immunological memory. This allows the adaptive immune system to mount a more specific and specialised immune response against an antigen upon encountering it for a second or subsequent time<sup>9</sup>. Based on the cell surface receptors they express, T cells can be categorised into Cluster of Differentiation 4 (CD4<sup>+</sup>) T cells and Cluster of Differentiation 8 (CD8<sup>+</sup>) T cells, also known as helper T cells and cytotoxic T cells respectively. Both types of T cell express T cell receptors (TCR) that recognise antigen, where the antigen is in the form of a peptide bound to one of the two classes of human major histocompatibility complex (MHC) proteins<sup>11</sup>. MHC proteins are expressed on the surface of antigen presenting cells (APCs) such as dendritic cells, macrophages and B cells, and serve to process and display antigen to the appropriate T cells to be killed, or to recruit or activate other immune cells<sup>8,11</sup>. CD8<sup>+</sup> T cells and CD4<sup>+</sup> T cells recognise peptide bound to MHC Class I and Class II molecules respectively<sup>8,10</sup>. With regards to their development, T cells undergo several stages of differentiation starting in the thymus with TCR rearrangement followed by positive and negative selection to ensure that TCRs recognise foreign peptide and not self-peptide. Mature T cells migrate to the periphery where they are activated to proliferate by binding to foreign peptide. Each TCR is composed of two polypeptide chains formed via a mechanism called DNA recombination in the variable (V), diversity (D) and joining (J) genes in the TCR, known as VDJ recombination<sup>10</sup>. This results in a diverse TCR repertoire able to recognise and respond to a wide range of antigens originating from bacteria, viruses, parasites and fungi<sup>12</sup>. The same genetic mechanism also plays a role in B cell development in the formation of immunoglobulins (Ig), more commonly known as antibodies, found on the surface of B cells.

As B cells are the focus of this thesis, they will be discussed in greater detail in the next section.

### 1.3 B Cells

B cells are so called as they were first discovered in an organ called the *Bursa* of Fabricius in 1965, the site of haematopoiesis in chickens<sup>13</sup>. In humans, B cells have a key function in adaptive immunity through their roles as antibody-producing cells to neutralise antigens and as APCs in association with T cells<sup>14</sup>. As with T cell development, B cell development requires many cytokines and transcription factors. Starting in the bone marrow, the common lymphoid progenitor cell gives rise to a pro-B cell and VDJ recombination occurs in the Ig molecule on its cell surface<sup>10</sup>. In terms of its structure, the Ig molecule is made up of two types of protein chain, light chains and heavy chains. On the pre-B cell, the pre-B cell receptor (BCR) is comprised of the heavy  $\mu$  chain expressed on the cell surface, as well as the surrogate light chain<sup>8</sup>. Rearrangement occurs in the light chains. During this process, kappa-deleting recombination excision circles (KRECs), DNA structures, are formed during VDJ recombination of the pre-BCR. Signalling through the pre-BCR triggers proliferation and differentiation into immature B cells that express a functional BCR with IgM, a subtype of Ig. At this stage, three mechanisms of central tolerance take place to eliminate autoreactive B cells via receptor editing, clonal deletion and clonal anergy<sup>15</sup>. If B cells have been positively selected, they emerge from the bone marrow into the periphery. In the absence of survival signals, B cells will die soon after exiting the bone marrow. In the absence of antigen, they mature in the peripheral blood. Alternatively, on encountering antigen, they become activated to differentiate in a germinal centre structure found in secondary lymphoid organs, which requires the assistance of follicular T helper cells<sup>16,17</sup>. Here, the processes of clonal expansion, somatic hypermutation, affinity maturation and class-switch recombination take place to produce memory B and antibody-producing plasma cells with highly antigen-specific BCRs able to recognise a wide range of epitopes<sup>18</sup>. Akin to the TCR repertoire, the formation of such a diverse BCR repertoire allows for the production of antigen-specific antibody. Indeed, a simplified definition of B cells is a population of cells with clonally diverse Ig on their cell surface<sup>18</sup>. As is the case for other immune cells, the expression of specific molecules on the surface of B cells at different stages of their development can be identified using flow cytometry to characterise different populations of B cells, known as immunophenotyping<sup>19</sup>. Cluster of Differentiation 19 (CD19) is a protein expressed continuously from the pro-B cell stage to the early stages of plasma cell differentiation while Cluster of Differentiation 20 (CD20) is expressed from the pre-B cell stage to plasma cell stage; both are cell surface markers used to confirm B cell lineage<sup>18,20</sup>. In addition, class-switched memory B cells express CD27 whereas naive B cells do not. In the treatment of B cell disorders, immunotherapeutic drugs can be targeted towards CD20 and CD19 such as the monoclonal antibodies rituximab and blinatumomab respectively<sup>21–23</sup>.

In this thesis, we model the time course of B cell recovery following various insults to the immune

system. These insults are explained in the sections below.

## 1.4 Insult to the Immune System

An insult to the immune system can be defined as an event that causes damage to the cells, tissues or organs of the immune system. This could occur due to medical intervention by way of a procedure or administration of drugs affecting the immune response such as immunosuppressants, anti-lymphocyte monoclonal antibodies and other immunomodulating drugs<sup>24,25</sup>. In addition, the biological mechanism of some infections cause insult to the immune system such as human immunodeficiency virus (HIV), which destroys  $CD4^+$  T cells, and Epstein-Barr virus (EBV), which results in uncontrolled proliferation of B cells<sup>26,27</sup>. Following an insult to the immune system, an individual is said to be immunosuppressed or immunocompromised, which refers to the weakened state of their immune system rendering them more susceptible to infection and disease<sup>28</sup>.

The four insults to the immune system that we will focus on, corresponding to the following four chapters of this thesis, are:

- Haematopoietic stem cell transplantation (HSCT) in children
- The administration of the monoclonal antibody rituximab for children with EBV reactivation post-HSCT
- The viral dynamics of EBV reactivation after HSCT in children
- The administration of rituximab biosimilars for children with rheumatological disease.

As HSCT concerns three of the four chapters, it is explained below. Further details of the other three insults (rituximab, EBV reactivation and rituximab biosimilars) are given in their respective chapters.

## 1.5 Haematopoietic Stem Cell Transplantation

### 1.5.1 Indications

When HSCs are dysfunctional or cause disease, it is possible to replace them with healthy HSCs in a procedure called haematopoietic stem cell transplantation (HSCT). As they are multi-potent and self-renewing, the transplanted HSCs will go on to proliferate in the bone marrow of the patient

to produce correctly functioning cells of the blood or immune system thereby repopulating the haematopoietic system as a whole or in part<sup>29</sup>. Indications for HSCT include malignant haematological disorders such as leukaemia and lymphoma, non-malignant haematological disorders such as anaemia, primary immunodeficiencies exemplified by severe combined immunodeficiency (SCID), metabolic disorders such as Hurler's syndrome and finally, autoimmune diseases such as systemic lupus erythematosus<sup>30</sup>. Depending on the indication for HSCT, the biological mechanism by which the HSCT is curative differs. For example, for a leukaemia patient undergoing HSCT, the donor's T cells recognise the patient's malignant cells as foreign and mount an immune response against them to destroy them. In addition, they receive high dose chemotherapy as part of their treatment before HSCT to ablate the malignant cells. In contrast, for a SCID patient, the donor HSCs proliferate to produce the missing or faulty cells to restore immune system function thereby correcting for the underlying genetic defect.

### 1.5.2 Types of HSCT

A HSCT may be referred to as a bone marrow transplant (BMT), peripheral blood stem cell transplant (PBSCT) or cord blood transplant (CBT) depending on the source of the healthy HSCs from bone marrow, peripheral blood or umbilical cord blood respectively. The method used to extract, or harvest, HSCs is contingent on the location of the healthy HSCs. For a BMT, a bone marrow aspiration is performed, in which a needle is inserted directly into the bone marrow of the iliac crest, a bone in the pelvis. In the case of a PBSCT, the patient is administered daily subcutaneous injections of granulocyte-colony stimulating factor (G-CSF) for the period of 4-7 days pre-HSCT to stimulate the bone marrow to produce more HSCs and mobilise them to the blood<sup>30</sup>. Blood is then passed through an apheresis machine, which separates out HSCs and removes them from the circulation, and returns the remaining blood to the patient. Lastly, for a CBT, HSCs are collected from the umbilical cord and placenta of a newborn baby, then frozen and stored in blood banks for future use. A further important categorisation of HSCTs is determined by the donor type. If autologous, the patient's own HSCs are extracted, stored then re-infused on the day of HSCT. In a syngeneic HSCT, HSCs from a patient's identical twin are used. The third and most common type of HSCT is with an allogeneic donor, who is related or unrelated to the patient. The donor is matched to the patient using histocompatibility testing on the basis of the human leukocyte antigen (HLA) system encoding for MHC molecules. While a matched sibling donor (MSD), matched familial donor (MFD) or matched unrelated donor (MUD) are desirable for optimal HLA matching, a mismatched familial donor (MMFD) or mismatched unrelated donor (MMUD) can also be used<sup>29</sup>. In addition, there is the option to use a haploidentical donor, who shares half the HLA genes as the patient. A recent study by the European Society for Blood and Marrow Transplantation (EBMT) documented numbers of both allogeneic and autologous HSCTs

continuing to increase, the number of CBTs gradually decreasing, and PBSC to be the preferred HSC source<sup>31</sup>. On a national level, according to the British Society of Blood and Marrow Transplantation and Cellular Therapy, 1397 first allogeneic HSCTs were performed in 2020 of which 292 (20.9%) were in children<sup>32</sup>.

### 1.5.3 Pre-HSCT Conditioning

In the days and weeks leading up to HSCT, the patient will receive a combination of chemotherapy, radiotherapy using total body irradiation and anti-lymphocyte antibodies, collectively known as a conditioning regimen. If the conditioning regimen is well tolerated by the patient, this increases the chance of the donor HSCs homing to the patient's bone marrow to actively undergo successful haematopoiesis, which is called engraftment<sup>33</sup>. The purpose of this is three-fold; to ablate malignant cells to reduce risk of disease relapse, to suppress the patient's immune system to counter graft rejection and reduce the risk of Graft versus Host Disease (GvHD), and to make space in the bone marrow for engraftment of the donor HSCs<sup>34,35</sup>. For some patients, conditioning may not be administered such as patients with SCID<sup>36</sup>. There are various types of conditioning regimen, which vary in their intensity and toxicity, namely myeloablative conditioning (MAC), minimal-intensity conditioning (MIC) and reduced-intensity conditioning (RIC). The conditioning regimen for an individual child's HSCT is chosen depending on factors such as their age and the HSCT indication<sup>35</sup>. Typical components of a conditioning regimen include chemotherapeutic drugs such as cyclophosphamide, busulfan and fludarabine and anti-lymphocyte antibodies to deplete T and B lymphocytes such as anti-thymocyte globulin (ATG) or alemtuzumab<sup>35</sup>. To complement a pre-HSCT conditioning regimen, a post-HSCT regimen prophylactic for GvHD can also be administered consisting of drugs such as mycophenolate mofetil, ciclosporin and tacrolimus<sup>37</sup>. Similarly, pre-emptive treatment strategies for other complications such as reactivation of EBV and cytomegalovirus (CMV) may also be implemented for some patients featuring drugs such as rituximab and ganciclovir<sup>38,39</sup>.

### 1.5.4 Post-HSCT Clinical Outcomes

Improvements in clinical practice, specifically in conditioning regimen protocols, HLA typing, supportive care and treatment of infections, have decreased the rates of mortality and morbidity post-HSCT. Recent data from Great Ormond Street Hospital (GOSH) for Children for HSCTs undertaken in 2020 demonstrate an overall survival rate of 83% (50/60) and a disease-free survival rate of 78% (21/27) at one year post-HSCT for all HSCT indications<sup>40</sup>. HSCT is a safe and effective procedure, presenting a curative treatment for many life-threatening diseases but the procedure is not without its limitations. The most common complication following HSCT is the development of acute or chronic GvHD, whereby the donor's T cells attack the patient's HSCs; 10% (6/60) of



patients at GOSH experienced grade 3 or grade 4 GvHD, the most severe types, in 2020, in line with published findings<sup>40–43</sup>. The greater the mismatch in HLA between the donor and recipient, the greater the chance that the recipient develops GvHD, which can occur in the skin, liver and gut<sup>30</sup>. During the post-HSCT period while immune reconstitution occurs, patients remain in an immunocompromised state and the type of opportunistic infections they encounter can be characterised<sup>44,45</sup>. During the first 30 days post-HSCT before engraftment has occurred, low levels of neutrophils allow the propagation of fungal infections such as *Aspergillus* and *Candida*<sup>46,47</sup>. In the second phase, spanning from 30 to 100 days post-HSCT, bacterial infections from *Staphylococcus* and Gram negative *Bacillus* are more commonly encountered as well as the reactivation of latent viruses such as EBV, CMV, adenovirus, human herpes virus 6 (HHV6) and *Varicella zoster*<sup>1,48–50</sup>. In the third and final phase from 100 days post-HSCT onward, adaptive immune function is slowly restored decreasing the overall incidence of infections but some viral infections are still seen at this late stage such as *Varicella zoster*<sup>51,52</sup>.

## 1.6 Immune Reconstitution

The decline and subsequent recovery of the immune system after insult can be tracked by measuring immune cell counts using flow cytometry in clinical laboratories using blood samples from routine blood tests<sup>53–57</sup>. Concentrations of the different immune cell subsets must return to age-specific normalised values in order to maintain and mount a protective response against pathogens<sup>58–60</sup>. This recovery process is called immune reconstitution, and is typically quantified by either measuring the time taken for lymphocyte subsets to reach pre-specified concentrations, i.e. the rate of reconstitution or measuring the concentration of lymphocyte subsets at specific time-points post-insult, i.e. the extent of reconstitution<sup>61–63</sup>. In both of these approaches, we consider immune cells to be biomarkers indicating the health of the immune system, where a biomarker is defined as a “characteristic that is measured and evaluated as an indicator of normal biologic processes, or pharmacological responses to a therapeutic intervention”<sup>64,65</sup>. In the context of HSCT, reconstitution of the innate immune system components, neutrophils and platelets, occurs in the short-term in the weeks to several months following HSCT<sup>66,67</sup>. In contrast, the reconstitution of B cells and T cells takes much longer and can last up to several years post-HSCT<sup>62,68</sup>. By its nature, the process of HSCT gives rise to chimerism, defined as the biological phenomena of cells from two different organisms co-existing simultaneously in the same body. Following allogeneic HSCT, measuring haematopoietic host-donor chimerism indicates the extent to which the donor HSCs have replaced the patient’s haematopoietic system<sup>69</sup>. The varying states of chimerism are microchimerism (less than 1% of recipient’s cells detected), split chimerism (one or more recipient-derived cell lineages as well as one or more donor-derived cell lineages), mixed chimerism (5-95% of cells are donor-derived) and

lastly, complete chimerism (100% of cells are donor-derived), indicating complete haematopoietic replacement<sup>70</sup>. Monitoring chimerism alongside immune reconstitution is instructive to clinicians, allowing them to intervene accordingly in the management of post-HSCT patients, e.g. a drop in donor chimerism may precede disease relapse, and could be prevented by modulating the treatment strategy<sup>71,72</sup>.

We focus on B cell reconstitution in this thesis, which will be explained further in Chapter 2.

## 1.7 Mathematical Modelling

### 1.7.1 Concepts

Mathematical modelling is a process in which real-life systems and relations in these systems are expressed using mathematics<sup>73</sup>. This allows the important aspects of the structure and behaviour of a system to be quantified, with the aim of gaining insights into its key relationships. A mathematical model itself is typically comprised of equations where the different terms correspond to the input(s) (also called independent variables), the output(s) (also called dependent variables) and parameters, which are variables that are not directly measured but are estimated from observed measurements<sup>74</sup>. Models are fitted to observed measurements of the system, along with measurements of covariates. Covariates are factors specific to individuals of a population that influence the observed data thereby explaining a large portion of their variability<sup>74,75</sup>. Parameter estimates are values estimated from both the observed measurements as well as the covariates. An inherent feature of observed data is the error generated when measuring them, commonly referred to as ‘noise’, arising from human error when recording the measurements and systematic error from the equipment taking the measurements<sup>74</sup>. This error is accounted for in the equations of the mathematical model by including an error term. As all models generally oversimplify a system, they are often caveated by assumptions to address the model’s limitations, and it is deemed that “all models are wrong but some are useful”<sup>76,77</sup>. Therefore, a range of models are fitted to the data to find which of them best describes the data. Coupled with mathematical modelling is simulation, which is the imitation of the dynamics of a system over time<sup>78</sup>. While a model looks backward in time, simulation looks forward in time<sup>74</sup>. After developing a mathematical model, it can be used for simulation in various ways. For example, in model evaluation, data not used in model development are generated, or simulated, using either interpolation or extrapolation with a view to internal or external validation<sup>75</sup>. In addition, model-based inferences can be made by testing a range of hypotheses and predicting future scenarios<sup>75</sup>. As modelling and simulation are both performed by computers using statistical software, it is possible to extensively test the conditions

and parameters of a system under real-world conditions to ensure that the mathematical model is robust and has maximum impact when implemented in practice for its desired application(s).

### 1.7.2 Pharmacometrics

One of the major applications of mathematical modelling and simulation is in the area of clinical pharmacology, where it is termed pharmacometrics, defined as the “branch of science concerned with mathematical models of biology, pharmacology, disease, and physiology used to describe and quantify interactions between xenobiotics and patients, including beneficial effects and side effects resultant from such interfaces”<sup>79</sup>. In pharmacometrics, mathematical models are typically based on ordinary differential equations (ODEs) that describe the relationship between observed data (e.g. serum drug concentration) and covariates (e.g. timing and number of doses given), most commonly following drug administration<sup>74</sup>. These ODEs form the structural model, and compartments are specified to represent physiological or abstract regions of tissues or cells into which the drug is administered and has its effect, whether direct or indirect<sup>75</sup>. An important consideration in mathematical modelling is accounting for the difference between model-predicted data and observed data, which is done by including a statistical model<sup>75</sup>. In addition, to intrinsically capture the influence of covariates on the parameters, a covariate model is developed<sup>75</sup>. The modelling technique used widely in pharmacometric research, and in this thesis, is non-linear mixed effects (NLME) modelling. It will be explained in greater detail in Chapter 2.

Pharmacometrics is used to characterise the pharmacokinetics (PK) of a drug, defined as “what the body does to the drug” or drug exposure, as well as pharmacodynamics (PD), defined as “what the drug does to the body” or drug response<sup>80</sup>. The key processes determining the PK of a drug are absorption, distribution, metabolism and excretion, and the therapeutic effect of a drug is governed by its physico-chemical properties<sup>81</sup>. The PD of a drug is inherently linked to its PK. Modelling both PK and PD using pharmacokinetic-pharmacodynamic (PK-PD) modelling remains the gold standard to inform clinical trials and practice<sup>82–84</sup>. When PK data cannot feasibly be collected or are absent, PD data can be modelled with a kinetic-pharmacodynamic (K-PD) approach, where some assumptions are made regarding PK<sup>85,86</sup>. Where drug is not administered into a system and therefore no pharmacological effect is present, mechanistic PD models can be used to describe biological processes of normal physiology or of pathology such as cell turnover, homeostatic feedback, disease activity and viral dynamics<sup>80,82,87–89</sup>. A typical PK dataset consists of drug concentrations over time from which drug-related PK parameters are estimated such as clearance ( $CL$ ), volume of distribution ( $V$ ) and elimination half-life ( $t_{1/2}$ ). A PD dataset can comprise of longitudinal concentrations of a biomarker or measurements of a disease score reflecting clinical outcome, from which system-specific PD parameters are estimated, e.g., the maximal drug effect ( $E_{max}$ ), dose produc-

ing 50% of maximal drug effect ( $ED_{50}$ ), production rate constant ( $k_{in}$ ) and death rate constant ( $k_{out}$ )<sup>80,81,89</sup>. Other types of pharmacometric approaches include physiologically-based PK (PBPK) models, disease-progression models, Bayesian models and model-based meta-analysis<sup>75,90–92</sup>.

The methodology of pharmacometrics is employed across all stages of drug development from discovery and pre-clinical studies to the three phases of clinical trials as well as post-marketing studies, forming the so-called “learn-confirm” cycles of drug development<sup>93,94</sup>. As a result, pharmacometrics informs clinical trial design, dose optimisation and determining off-label dosing in special populations<sup>83</sup>.

## 1.8 Mathematical Modelling of Immune Reconstitution

To date, most studies of immune reconstitution use survival analysis, which measures the fraction of a population that reach an endpoint, or outcome, over time<sup>90</sup>. The time period is the time between a starting point, e.g. an insult to the immune system such as HSCT, and a terminating event, e.g. immune reconstitution<sup>95</sup>. In its most simplest form, the impact of one predictor variable on the outcome of interest is studied, often visualised by a Kaplan-Meier survival curve<sup>96</sup>. Predictor variables that are commonly explored post-HSCT in relation to immune reconstitution are those that contribute towards clinical outcomes such as donor type, stem cell source and conditioning regimen<sup>66,97,98</sup>. In addition, the use of multivariable Cox proportional hazards models allows for the adjustment of the effect of multiple predictor variables to identify factors that are more strongly associated with immune reconstitution<sup>66,99</sup>.

While survival analysis is the gold standard in clinical practice to inform prognosis, it does not allow for the interrogation of the biological mechanisms dictating immune reconstitution post-HSCT<sup>100</sup>. Using a mechanistic mathematical modelling, by way of pharmacometrics, gives insight into the underlying biological processes whilst considering additional aspects such as the non-linearity of these processes, the covariates contributing to the heterogeneity of HSCTs and the variability in immune reconstitution between different patients<sup>63,90</sup>. Indeed, one strand of pharmacometric research is its application in the therapeutic areas of immunology and infectious diseases<sup>63,101,102</sup>. For example, it has been used to model T cell reconstitution both post-HSCT and after HIV infection, the effects of drugs commonly administered in the HSCT setting as part of conditioning and prophylactic GvHD regimens and viral kinetics<sup>103–111</sup>.

As they are a specialised population displaying heterogeneity and variability in their response to drugs, conducting pharmacometric studies in children, in particularly for drugs that are commonly administered off-label, can inform the optimisation and personalisation of paediatric drug regimens and therefore, improve efficacy of treatment.

## 1.9 Research Aims

The overarching aim of the research detailed in this thesis was to use a mathematical modelling approach to investigate the reconstitution of B cells in children following various insults to the immune system. In the models presented in the following four chapters, retrospective electronic data from children were used to construct models with an emphasis on scaling B cell dynamics for age and incorporating prior knowledge to estimate biologically meaningful parameters. Measurements of CD19<sup>+</sup> cell counts were used as a biomarker to indicate recovery of B cells for Chapters 2, 3 and 5, while measurements of EBV viral load (VL) were used for Chapter 4 as a biomarker of EBV reactivation. Chapter 2 describes a novel mechanistic NLME model to quantify CD19<sup>+</sup> cell reconstitution post-HSCT, incorporating prior biological knowledge to scale for age-related effects. Building on this model, Chapter 3 presents a K-PD model to quantify the pharmacodynamics of rituximab on CD19<sup>+</sup> cell reconstitution in patients with EBV post-HSCT. The first part of Chapter 4 focusses on the development of a multivariable Cox proportional hazards model to assess time to first EBV reactivation in the first 100 days post-HSCT. In the second part of Chapter 4, sensitivity analysis of a previously reported mathematical model of EBV viral kinetics is performed and a mechanistic NLME model of EBV viral kinetics is developed. Finally, Chapter 5 presents a K-PD model to quantify the pharmacodynamics of rituximab biosimilars on CD19<sup>+</sup> cell reconstitution in children with rheumatological diseases.

## Chapter 2

# B Cell Reconstitution After HSCT

### 2.1 Introduction

#### 2.1.1 B Cell Reconstitution

All cells of B lineage express CD19<sup>+</sup> from pro-B to plasma cell stages of B cell development therefore B cell reconstitution is monitored by measuring the number of CD19<sup>+</sup> cells longitudinally<sup>20,21</sup>. The period of B cell reconstitution post-HSCT can last up to three years<sup>34,112,113</sup>, with recovery recapitulating ontogenic B cell maturation as seen by rising B cell numbers then a gradual decrease to age-normalised values in peripheral blood<sup>114–116</sup>. The number of total B cells normalise in the first six months after HSCT, comprised mostly of naive or transitional B cells, which are the first B cell subset to emerge in the peripheral blood between one to two months post-HSCT<sup>117–119</sup>. Despite being present in large numbers, they are functionally immature compared to memory B cells, which have been demonstrated to be deficient for up to two years after HSCT<sup>120–122</sup>. Functional B cell reconstitution is further delayed by poor T cell reconstitution post-HSCT, given the requirement of T cell help to produce memory or plasma B cells<sup>123</sup>. This results in a lower capacity of the remaining B cells to generate antigen-specific antibody leading to a global reduction in immunoglobulin levels<sup>45,122,124</sup>.

Furthermore, the complexity of B cell reconstitution post-HSCT is an inherent product of the numerous patient-, donor-, transplant-, disease- and drug-related factors at play including the age of the patient, conditioning regimen received, stem cell source, serotherapy, and development of GvHD<sup>125</sup>. Administration of alemtuzumab as prophylactic GvHD conditioning has been associated with sometimes delaying B cell reconstitution<sup>98,122</sup>. With regards to conditioning, if the indication

for HSCT is a malignant or non-malignant haematological disorder, a MAC regimen is favoured over RIC for donor chimerism and increased likelihood of successful B cell reconstitution<sup>97,126,127</sup>. There is also an association with GvHD, with patients with higher grades of acute GvHD or chronic GvHD reported to experience significantly impaired B cell reconstitution<sup>121,128</sup>. With regards to stem cell source, cord blood has been shown to result in the fastest B cell reconstitution compared to peripheral blood and bone marrow in the short-term post-HSCT, in part explained by the greater number of B cell progenitor cells<sup>62,66,129,130</sup>. In addition, B cell reconstitution is further exacerbated by the administration of B cell depletive therapies such as rituximab for EBV reactivation.

### 2.1.2 Bone Marrow Output

As there is a degree of chimerism after HSCT, new B cells can originate from both the patient or the donor, arising from either the production of naive B cells from HSCs in the bone marrow or from expansion of mature B cells in the peripheral blood. Whilst the return of B cell counts to age-normalised B cell values might suggest restoration of the B cell compartment, it does not guarantee that bone marrow output of new B cells is restored<sup>131</sup>. To further interrogate the underlying biology of B cell reconstitution with respect to bone marrow output, we must therefore consider more direct measures of bone marrow output. Kappa-deleting recombination excision circles (KRECs) are stable non-dividing DNA structures formed during VDJ recombination of the light chains in the pre-BCR. Present in approximately 50% of newly produced B cells leaving the bone marrow, KRECs have been quantified experimentally as a biomarker of *de novo* production of B cells in the bone marrow<sup>132–134</sup>. Similarly, their T cell counterparts, TCR excision circles (TRECs), are formed during recombination of TCRs and have been measured in relation to T cell reconstitution following HSCT and HIV infection<sup>106,110,135,136</sup>. In addition, an assay to simultaneously quantify TRECs and KRECs post-HSCT has been established and applied to both adults and children<sup>131,137</sup>, with other studies using a similar experimental approach to study T and B cell reconstitution in various disease settings<sup>138–142</sup>.

For successful regeneration of a functional B cell compartment, the production of new B cells in the bone marrow must be complemented by the proliferation of these cells as well as the expansion of mature B cells in peripheral blood. One marker of cell proliferation is Ki67, a protein found in the nucleus of normal and leukaemic cells that is associated with the cell cycle<sup>143</sup>. In naive T cells, quantification of Ki67 expression in adults and children has shown a decline with respect to age<sup>135,144,145</sup>. Furthermore, Payne *et al* have recently reported a decrease in Ki67 levels in naive B cells with increasing age in the context of HIV infection in children, with applicability to HSCT. In this study, the authors observed a peak naive B cell output at one year of age then a decrease thereafter to stable levels<sup>146</sup>.

### 2.1.3 Scaling

The World Health Organisation has defined paediatric clinical pharmacology as a “scientific discipline that involves all aspects of the relationship between drugs and humans during growth, development and maturation”<sup>81</sup>. In order to meet this goal, scaling is required, which is the process of standardising PK and PD data between species and within humans using age and size<sup>147</sup>. The paediatric population encompasses neonates, infants, children and adolescents, and within this diverse age group, there is continual growth, development and maturation of organs, enzymes and major body systems which affect PK and PD<sup>148,149</sup>. Furthermore, as with other special populations, children are commonly administered medicines on an off-label basis, i.e. for indications they are not licensed for<sup>150</sup>. Therefore, scaling is of particular importance in paediatric pharmacometric studies to account for ontogeny, to help explain the heterogeneity and variability often observed in children’s response to medication in comparison to adults, and to ultimately ensure that a safe, optimal and efficacious dose is administered to a paediatric patient, no matter their age or size<sup>151–153</sup>.

In pharmacometric models, scaling is applied to individual PK and PD parameters using mathematical functions, often derived from biological prior information<sup>154,83</sup>. While scaling is more commonly implemented in PK models<sup>153,155</sup>, it is increasingly being considered for PD, given its key role in determining the potency, efficacy and therapeutic index of a drug<sup>80,156</sup>. Two frequently used scaling approaches are maturation functions to account for the development of enzymes and organs involved in drug metabolism and elimination, and allometric scaling to translate pre-clinical PK data to humans or to extrapolate adult PK data to paediatrics<sup>157,158</sup>. In this thesis, the developing immune system was considered, to which mechanistic biological prior knowledge was applied to scale PD parameters for age-related effects<sup>82,106,159,160</sup>.

### 2.1.4 Aim

This project aimed to develop a mechanistic NLME model to quantify CD19<sup>+</sup> cell reconstitution post-HSCT in children, scaling for age-related effects and estimating the time delay between HSCT and CD19<sup>+</sup> cell production by the bone marrow.

### 2.1.5 Objectives

- Clean patient electronic data of retrospective CD19<sup>+</sup> cell counts and other covariates
- Use published prior biological knowledge to develop a B cell maturation function to allow scaling of model parameters for age-related effects



- Test appropriate mathematical functions to account for the time delay in  $CD19^+$  cell production by the bone marrow after HSCT
- Construct NLME model of  $CD19^+$  cell reconstitution and identify factors that affect this recovery
- Evaluate model by performing diagnostic checks to compare model-predicted and observed data

## 2.2 Methods

### 2.2.1 Ethics Statement

Research conducted as part of this doctoral thesis involved human participants and was issued ethical approval by the Great Ormond Street Hospital for Children (GOSH) NHS Trust for the project “*Extrapolation of haematopoiesis dynamics following cytotoxic insult to personalise paediatric drug development*” (original REC reference 17/LO/0008, later updated to 21/LO/0646: *Use of routine GOSH data for research, R&D reference 18IR20*). In addition, this study utilised the GOSH Digital Research Environment (DRE) with access to previously collected, non-identifiable clinical information. This is covered under the ethical approval, 17/LO/0008 and 21/LO/0646. Written informed consent from the participants’ legal guardian/next of kin was not required to participate in this study in accordance with the national legislation and the institutional requirements.

### 2.2.2 Data

Retrospective electronic data from routine clinical practice were collected from children who underwent HSCT at the Bone Marrow Transplant Unit at GOSH between 2000 and 2016. Three inclusion criteria were used to identify patients; that they had:

- Measurements of  $CD19^+$  cell counts post-HSCT
- Undergone their first HSCT
- Not received rituximab for EBV reactivation post-HSCT (rituximab is a drug that depletes B cells and would therefore confound attempts to build a model of ‘normal’ B cell reconstitution post-HSCT in the absence of drugs affecting B cell dynamics).

The model-building dataset comprised  $CD19^+$  cell counts, measured in  $10^6$  cells/L of blood, from 359 children. A flow diagram of patients in the study is given in Figure 2.1. Data collected included

patient-specific, donor-specific and transplant-specific variables as well as measurements of immune cell subsets obtained by immunophenotyping using flow cytometry. Regarding sensitivity of the assay to detect lymphocytes, 10,000 events were targeted in the lymphocyte gate. Data extraction was performed by the GOSH DRE team and uploaded into the Aridhia DRE platform.

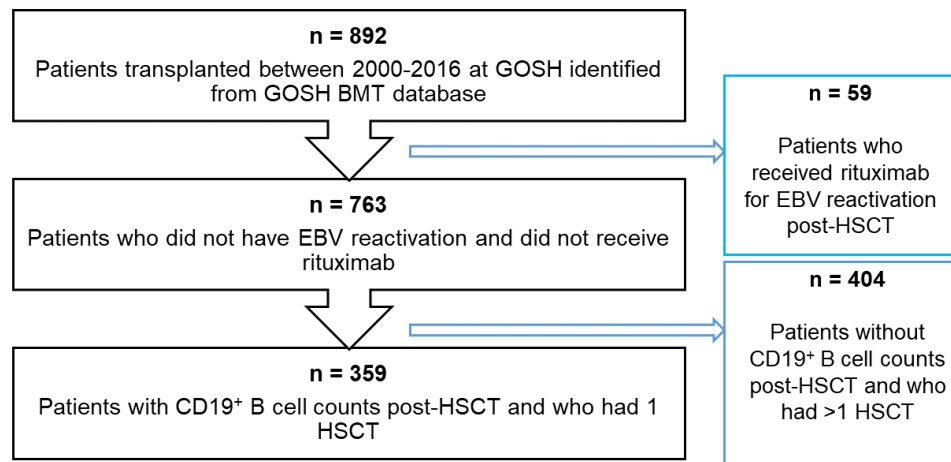


Figure 2.1: Flow diagram of study patients. GOSH, Great Ormond Street Hospital; BMT, Bone Marrow Transplant; EBV, Epstein-Barr virus; HSCT, Haematopoietic stem cell transplant.

### 2.2.3 Non-linear Mixed Effects Modelling

Where data is in the form of repeated measurements from a group of individuals from a population of interest, non-linear mixed effects (NLME) modelling allows the estimation of parameters both at the population and individual levels<sup>75,161</sup>. Some key advantages of NLME models are their ability to account for multiple levels of variability in a hierarchical framework and handle the often challenging characteristic features of paediatric clinical data, which are its non-linearity, sparsity and small sample sizes<sup>74</sup>.

The first component of an NLME model is the structural model, into which the effects of covariates are incorporated, and the second component, the statistical model, accounts for sources of variability, of which there are two main types. Inter-individual variability (IIV), or between-subject variability (BSV), is the difference between the mean population value of a parameter and the parameter value for an individual, and unexplained residual variability encompasses misspecification errors, bias and noise<sup>161</sup>.

To represent an NLME model in mathematical terms, let us consider a population NLME model to describe the change in the dependent variable of interest, CD19<sup>+</sup> cell count,  $y$ , with time.

$$y_j = f(\phi, t_j) + \epsilon_j, \quad \epsilon_j \sim \mathcal{N}(0, \sigma^2), \quad (2.1)$$

where  $y_j$  is the  $j$ th observation of the CD19<sup>+</sup> cell count  $y$ ,  $f(\phi, t_j)$  is a non-linear differentiable function based on the parameter vector  $\phi$  and time  $t_j$ , and  $\epsilon_j$  is the residual error, normally distributed with mean 0 and variance  $\sigma^2$ .

The parameter vector  $\phi$  refers to the fixed effects, i.e. parameters that have the same value for every individual in the population. To allow for deviation of the individual parameter values from the population parameter values (IIV), we can introduce random effects into the above model<sup>75</sup>. The parameter vector for the  $i$ th individual,  $\phi_i$ , is then given by

$$\phi_i = \mu + \eta_i, \quad \eta_i \sim \mathcal{N}(0, \Omega), \quad (2.2)$$

where  $\mu$  is the vector of fixed effects and  $\eta_i$  is the vector of random effect parameters for the  $i$ th individual normally distributed as per the variance-covariance matrix,  $\Omega$ . The diagonal elements of  $\Omega$  are the variances, and the off-diagonal elements are the covariances.

Combining the two equations above, the full mixed-effects model is then given by

$$y_{ij} = f(\phi_i, t_{ij}) + \epsilon_{ij}, \quad \epsilon_{ij} \sim \mathcal{N}(0, \sigma^2), \quad (2.3)$$

where the residual error is now  $\epsilon_{ij}$ , still normally distributed with mean 0 and variance  $\sigma^2$ .

In pharmacometrics, various software are available to fit NLME models to data for parameter estimation. In this thesis, we will use the Non-Linear Mixed Effects Modelling (NONMEM) software version 7.4.3, which employs algorithms to maximise the likelihood function to provide estimated values most likely to occur based on the observed data as well as their associated variability<sup>162</sup>. When an algorithm is used to fit a model in NONMEM, an objective function value (OFV) is usually provided as a measure of model fit, expressed as the -2 log likelihood. To instruct NONMEM to perform parameter estimation, a control stream of commands must be supplied including details of the model to be fitted and the model-building dataset. In line with the NLME framework described above, some examples of labels used in a typical NONMEM control stream are  $\theta$  (THETA) for the fixed effects parameters,  $\eta$  (ETA) for the IIV,  $\omega$  (OMEGA) for the variance of the IIV and  $\sigma$  (SIGMA) for the variance of the residual error<sup>163,164</sup>.

### 2.2.3.1 Covariate Model Building

To identify the factors influencing CD19<sup>+</sup> cell reconstitution, the relationships between various covariates and model parameters can be tested and quantified. Covariates can be categorical (dichotomous and polychotomous) or continuous, and can be parameterised using various functions. If the number of covariates is low, they may be tested manually by adding a covariate to a parameter one at a time to see if there is a corresponding decrease in OFV. However, a more commonly used automated method for covariate model-building is stepwise covariate modelling (SCM) implemented in Perl-speaks-NONMEM (PsN)<sup>165</sup>. In the forward search of the SCM approach, covariates are added into the base structural model one at a time to each parameter in a stepwise manner, based on statistical significance ( $p < 0.05$ ). This creates a new model for every parameter-covariate relationship being tested. Each of these new models is tested in a univariate manner with the null hypothesis that the covariate has no significant effect on the parameter. This continues until the addition of further covariates does not result in a significant improvement in the fit. In this way, the models are nested within the base model. During the subsequent backward elimination step, covariates identified as significantly improving the model fit are tested again at a higher significance level ( $p < 0.01$ ) and excluded if they no longer significantly improve the fit.

### 2.2.3.2 Handling Data Below the Lower Limit of Quantification

Every assay has a lower limit of quantification (LLOQ) below which measurements cannot accurately or precisely be recorded as the assay is no longer sensitive. The assays used in clinical laboratories to measure CD19<sup>+</sup> cell counts are no exception. When measurements are below the LLOQ, they are recorded as below limit of quantification (BLQ) and various methods are available to appropriately handle BLQ data. During immune reconstitution post-HSCT, BLQ measurements are common for all immune cell subsets, especially in the early post-HSCT period. In total, seven methods of dealing with BLQ data in pharmacometrics have been proposed<sup>166</sup>. During model-building, both the M5 and M3 methods were tested. The M5 method replaces all BLQ observations by LLOQ/2 while with the M3 method, the probability that the BLQ observations are indeed BLQ is calculated by integrating the probability density function between minus infinity and the LLOQ.

### 2.2.3.3 Model Evaluation

After building an NLME model, it is important to identify any model misspecification and biases. This is done by comparing the observed data to the model-predicted data (goodness-of-fit), testing assumptions made in the model-building process and simulating data using the final model. The

most common method is to use graphical evaluation to produce a suite of prediction-based and simulation-based diagnostic graphs<sup>167,168</sup>.

For the prediction-based diagnostic plots, a typical starting point is to plot the observed data (DV) against both the population predictions (PRED) and individual predictions (IPRED). If the model is an adequate description of the data, the data points should be scattered along the line of unity for both graphs. To test the assumption that the residual error follows a normal distribution with a mean of zero, the conditional weighted residuals (CWRES) are plotted against PRED or time, with the majority of residuals expected to be dispersed between  $\pm 2$  standard deviations of the mean and to be independent of time. Similarly, the individual weighted residuals (IWRES) can be plotted against IPRED to detect issues with the error model.

Regarding the simulation-based diagnostics, the most used graph of this type is the visual predictive check (VPC)<sup>169</sup>. It is produced by using the model-estimated parameter values to simulate a large number of datasets, followed by plotting the 95% prediction intervals around the simulated percentiles (usually as shaded areas) and comparing these to the observed percentiles (usually as lines). An alternative to the traditional VPC is the prediction-corrected VPC (pcVPC), which scales the observations and simulations using the model predictions<sup>170</sup>.

To check the reliability of parameter estimates, their relative standard error (RSE) is calculated and a bootstrap analysis can be performed. This technique samples the model-building dataset many times with replacement then fits the model to each of the samples thereby producing many parameter estimates. The median parameter estimate and its 95% confidence interval are then reported and compared with the original model estimates.

## 2.2.4 Model Building

### 2.2.4.1 B Cell Maturation Function

The age distribution of the 359 patients in the model-building dataset spanned 0-17 years. In addition to this inter-individual variability in age, the post-HSCT period when CD19<sup>+</sup> cell reconstitution occurs is parallel to the time period of ontogenic development and maturation of the immune system in children. Therefore, the effect of age must be considered at the level of the structural model to scale the observed CD19<sup>+</sup> cell dynamics for age.

First, let us consider the change in CD19<sup>+</sup> cell count ( $A$ ) over time ( $t$ ), which can be described by a turnover model as follows;

$$\frac{dA}{dt} = \lambda - \mu A, \quad (2.4)$$

where  $\lambda$  is the zero-order CD19<sup>+</sup> cell proliferation rate and  $\mu$  is the first-order CD19<sup>+</sup> cell death rate. Therefore at steady-state, when  $\frac{dA}{dt} = 0$ , the CD19<sup>+</sup> cell count is given by

$$A = \frac{\lambda}{\mu}, \quad (2.5)$$

according to which, the CD19<sup>+</sup> cell count would be identical for all individuals irrespective of their age. However, when looking to prior biological knowledge, this is not the case. Many studies have measured CD19<sup>+</sup> cell counts in healthy adults and children, and described a decline in the frequency and absolute number of total CD19<sup>+</sup> cell counts with age that then stabilises in adulthood<sup>54,58,59,119,171</sup>. In addition, quantification of the cell proliferation marker Ki67 in naive B cells of healthy children has shown that Ki67 declines with age suggesting that CD19<sup>+</sup> cell turnover,  $\mu$ , would also decrease with age thereby, in theory, increasing CD19<sup>+</sup> cell count<sup>146</sup>. Therefore, it can be deduced that the proliferation of CD19<sup>+</sup> cells,  $\lambda$ , must also decrease with age for there to be a net decrease in total CD19<sup>+</sup> cell count.

Similar to CD19<sup>+</sup> cells, CD4<sup>+</sup> cell dynamics exhibit a relationship with age<sup>60,135,145</sup>. Bains *et al* derived the following expression for the export of naive CD4<sup>+</sup> T cells from the thymus per day for a person at age  $t$ ;

$$\theta(t) = \frac{y(t)N(t)\tau}{\Delta(c - \tau)}, \quad (2.6)$$

where  $\theta(t)$  is the number of CD4<sup>+</sup> cells exported by the thymus per day,  $y(t)$  is the fraction of naive CD4<sup>+</sup> cells expressing Ki67,  $N(t)$  is the total naive CD4<sup>+</sup> cell population,  $\Delta$  is the duration of Ki67 expression, and  $c$  and  $\tau$  are constants representing the average TREC content of the thymocytes entering the peripheral naive pool and of the peripheral naive CD4<sup>+</sup> cell pool respectively<sup>136</sup>.  $N(t)$  is estimated from  $\frac{v(t)V(t)}{0.02}$ , where  $v(t)$  is the naive CD4<sup>+</sup> cell count per unit volume of blood and  $V(t)$  is the blood volume, under the assumption that 2% of the cells circulating in the blood are lymphocytes<sup>172</sup>.

From the equation above, omitting the constants gives the following expression:

$$\theta(t) = y(t)N(t). \quad (2.7)$$

Payne *et al* directly estimated the equivalent of the parameters described above for B cells by performing flow cytometry on B cells from the peripheral blood of healthy and HIV-infected South African children<sup>146</sup>. On the basis that B cell development shares similarities with T cell development, they then applied Bains *et al*'s mathematical model for thymic export of naive CD4<sup>+</sup>

cells to calculate naive B cell output from the bone marrow in HIV-uninfected and HIV-infected children<sup>146</sup>. Based on Bains *et al* and the age-dependent nature of CD19<sup>+</sup> cell dynamics, our aim was to develop a B cell maturation function for the effect of age on naive CD19<sup>+</sup> cell output from the bone marrow just as Bains *et al* developed a T cell maturation function to allow for age to affect the naive CD4<sup>+</sup> cell output from the thymus. Ultimately, this would allow the scaling of the rate constant of CD19<sup>+</sup> cell proliferation,  $\lambda$ , and the rate constant of CD19<sup>+</sup> cell death,  $\mu$  for age.

Since CD19<sup>+</sup> cells are being measured as a concentration, the units are in cells per unit volume of blood, i.e.  $\lambda = \frac{o}{V(t)}$ , where  $o$  is the number of CD19<sup>+</sup> cells exported by the bone marrow per day,  $\lambda$  is the zero-order CD19<sup>+</sup> cell proliferation rate and  $V(t)$  is the blood volume. As  $M(t) = w(t)V(t)$  (where  $M(t)$  is the total naive CD19<sup>+</sup> cell population and  $w(t)$  is the naive CD19<sup>+</sup> cell count per unit volume of blood), when we divide by  $V(t)$  to obtain cells/volume, we have the following expression for  $\lambda$ :

$$\lambda(t) \propto z(t)w(t), \quad (2.8)$$

where  $z(t)$  is the fraction of naive CD19<sup>+</sup> cells expressing Ki67.

Regarding  $\mu$ , it should be scaled for the fraction of naive B cells expressing Ki67 therefore it is multiplied by  $z(t)$ .

To build the B cell maturation function, expressions were derived for  $w(t)$ , the naive B cell count per unit volume of blood at age  $t$ , and  $z(t)$ , the fraction of naive B cells expressing Ki67 at age  $t$ . For  $w(t)$ , data were extracted from a published figure illustrating change with age in the count of naive (CD27<sup>-</sup> IgD<sup>+</sup>) B cells per  $\mu\text{l}$  of blood, seen in Figure 2.2<sup>54</sup>.

Using the *nls()* function in the *stats* package in the R environment, non-linear least squares was used to fit the data to three variations of an exponential decay model; mono-exponential decay

$$A(t) = \beta_0 \exp\{-\beta_1 t\}, \quad (2.9)$$

mono-exponential decay with constant

$$A(t) = \beta_0 \exp\{-\beta_1 t\} + \beta_2, \quad (2.10)$$

and bi-exponential decay

$$A(t) = \beta_0 \exp\{-\beta_1 t\} + \beta_2 \exp\{-\beta_3 t\}. \quad (2.11)$$

Model fit was assessed using the Akaike Information Criterion (AIC), and parameters from the

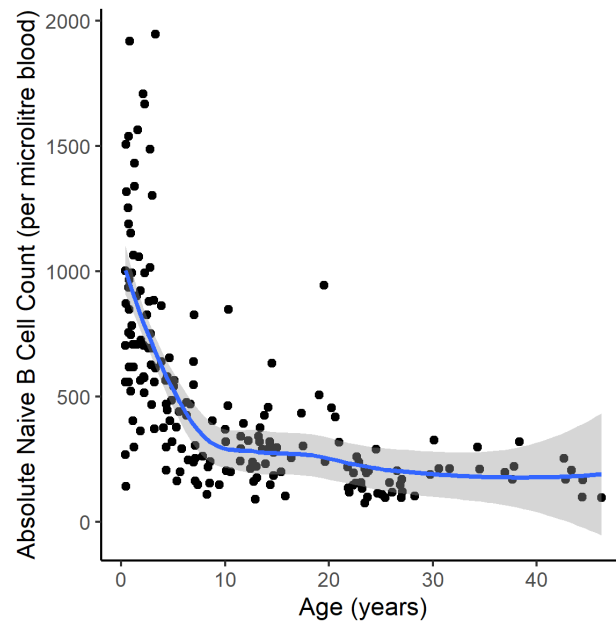


Figure 2.2: Decrease in absolute number of CD27- IgD+ naive B cells (per microlitre blood) with age. Data points extracted from Morbach *et al*<sup>54</sup>, blue line is the local regression curve and grey area is the 95% confidence interval.



model with the lowest AIC value were selected to form the following expression for change in naive B cell concentration with age,  $w(t)$ ,

$$w(t) = \frac{868 \cdot e^{(-0.187 \cdot t)} + 200}{200}. \quad (2.12)$$

For  $z(t)$ , the fraction of naive B cells expressing Ki67 with age, experimental data were available from Payne *et al* from quantification of Ki67 in naive B cells of healthy South African children shown in Figure 2.3<sup>146</sup>.

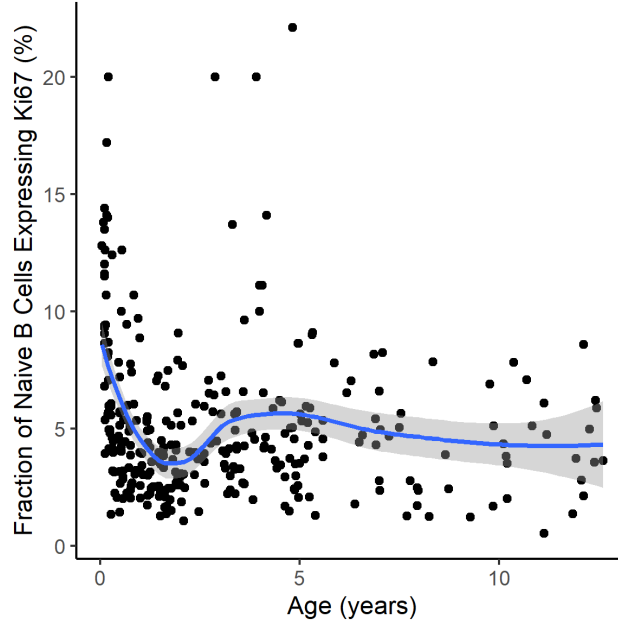


Figure 2.3: Decline in fraction of naive B cells expressing Ki67 with age in healthy South African children. Data from Payne *et al*<sup>146</sup>, blue line is local regression curve and grey area is 95% confidence interval.

Model fitting and selection was performed as described above for the Morbach data, providing the expression below,

$$z(t) = \frac{13.9 \cdot e^{(-7.25 \cdot t)} + 4.55}{4.55}. \quad (2.13)$$

While the product of both of these expressions form the complete B cell maturation function, the two individual components,  $w(t)$  and  $z(t)$ , can be thought of as maturation functions in their own right. Of note, both of the maturation functions are relative to the constant count of naive B cells

for adults and constant fraction of naive B cells expressing Ki67 for adults, and are therefore given as a proportion of the adult model.

The different models fitted to both datasets and their AIC values are given in Table 2.1; the mono-exponential decay model with a constant model best described the data for both maturation functions.

Table 2.1: Models tested for B cell maturation function.  $w(t)$  is the naive B cell count per  $\mu L$  blood at age  $t$ .  $z(t)$  denotes the fraction of naive B cells expressing Ki67 at age  $t$ .

Models Tested	AIC $w(t)$	AIC $z(t)$
Mono-exponential decay	2610	1649
Mono-exponential decay with constant	2598	1581
Bi-exponential decay	2600	1583

#### 2.2.4.2 Delay Function

Following HSCT, there is a delay before bone marrow output recovers and resumes *de novo* production of B cells<sup>98,118</sup>. To represent this biological delay in the mathematical model, two functions were considered, each introducing two new parameters. The first was a previously published sigmoidal function by Hoare *et al* originally used in the context of post-HSCT recovery of thymic output<sup>106</sup> and the second was a Hill equation. The equations of the functions and their associated parameters are summarised in Table 2.2.

Table 2.2: Functions tested to estimate delay in recovery of bone marrow output of CD19<sup>+</sup> cells after HSCT.

Equation	Parameters	Description
$y = \frac{1 - \exp(-2t/\lambda_h)}{1 + \exp(\lambda_r(1 - t/\lambda_h))}$	$\lambda_h$ (days) $\lambda_r$	Time to recovery of bone marrow output of CD19 <sup>+</sup> cells Rate of recovery in bone marrow output of CD19 <sup>+</sup> cells

Equation	Parameters	Description
$y = \frac{t^\gamma}{t^\gamma + T_{50}^\gamma}$	$T_{50}$ (days)	Time to half-maximal bone marrow output of CD19 <sup>+</sup> cells
	$\gamma$	Steepness of slope of CD19 <sup>+</sup> cell recovery

### 2.2.5 Software

Retrospective electronic data were extracted, anonymised and uploaded by the DRE team into a secure online Aridhia workspace created specifically for this doctoral research on the Microsoft Azure Cloud platform. Data cleaning, data exploration, data visualisation and model evaluation were carried out using R statistical software<sup>173</sup>, version 4.2.0, namely using the *tidyverse* collection of packages<sup>174</sup> and the *xpose4* package<sup>175,176</sup>. Models were implemented in NONMEM version 7.4.3, and details of subroutines and algorithms used are given in each chapter<sup>162</sup>. Perl speaks NONMEM (PsN) version 4.8.1 was used for covariate model building, producing visual predictive checks (VPCs) and performing non-parametric bootstrap for model evaluation<sup>165,177</sup>.

## 2.3 Results

### 2.3.1 Patient Characteristics

In total, 3126 measurements of CD19<sup>+</sup> cell counts from 359 children (median age at HSCT, 3.02 years; range, 0.08-17 years) were used for model-building, as visualised in Figure 2.4. The study period was for two years post-HSCT therefore a cut-off of 730 days post-HSCT was used for measurements of CD19<sup>+</sup> cell counts. The patients were representative of a typical paediatric HSCT cohort, with a range of HSCT indications including malignant and non-malignant conditions, varied sources of stem cells, and different types of donor and conditioning regimen. Patient characteristics are summarised in Table 2.3.

Table 2.3: Patient characteristics for model-building dataset for CD19<sup>+</sup> cell model. PID, primary immunodeficiency; NMH, non-malignant haematological ; MH, malignant haematological; BM, bone marrow; PBSC, peripheral blood stem cell; CB, cord blood; MAC, myeloablative conditioning ; MIC, minimal intensity conditioning; RIC, reduced intensity conditioning.

	Total Patients ( $n = 359$ )
<b>Age (years), median (range)</b>	3.0 (0.08 - 17.0)
<b>Gender, <math>n</math> (%)</b>	
Female	132 (36.7)
Male	227 (63.3)
<b>Diagnosis, <math>n</math> (%)</b>	
PID	160 (44.6)
NMH/MH/Other	199 (55.4)
<b>Donor Type, <math>n</math> (%)</b>	
Matched	259 (72.1)
Mismatched	100 (27.9)
<b>Cell Source, <math>n</math> (%)</b>	
BM	167 (46.5)
PBSC	130 (36.2)
CB	62 (17.3)
<b>Conditioning, <math>n</math> (%)</b>	
MAC	161 (44.8)
MIC/RIC/None	198 (55.2)
<b>Serotherapy, <math>n</math> (%)</b>	
Yes	90 (25.1)
No	269 (74.9)

### 2.3.2 Structural Model

Upon incorporating the B cell maturation function and the delay function, the final structural model was given by:

$$\frac{dA_1}{dt} = \lambda \cdot \left( \frac{T^\gamma}{T^\gamma + T50^\gamma} \right) - \mu(A_1), \quad (2.14)$$

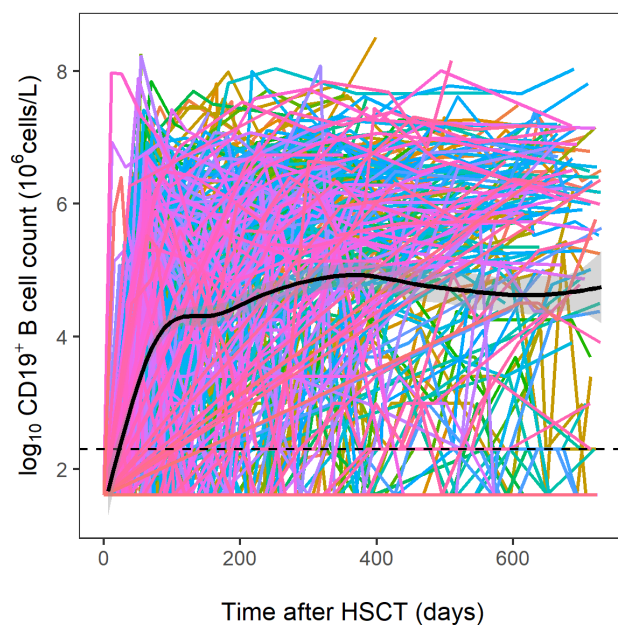


Figure 2.4: Raw data used for model-building. Each coloured line is an individual patient and the black dotted line represents the LLOQ of the assay used to measure  $\text{CD19}^+$  cell counts ( $10 \times 10^6$  cells/L). The thick black line is the local regression curve, and the grey shaded area is the 95% confidence interval.

where  $\lambda = TV_{\lambda} \cdot w(t) \cdot z(t)$  and  $\mu = TV_{\mu} \cdot z(t)$ , i.e. the B cell maturation function was applied *a priori* to  $\lambda$  and  $\mu$ .  $A_1$  represents the central B cell compartment. In total, there were four parameters to be estimated:  $\lambda$ , CD19<sup>+</sup> cell production rate constant;  $\mu$ , CD19<sup>+</sup> cell death rate constant;  $\gamma$ , Hill exponent for steepness of slope of CD19<sup>+</sup> cell recovery; and  $T50$ , time to half-maximal output of CD19<sup>+</sup> cells by the bone marrow. The model has been depicted as a schematic in Figure 2.5.

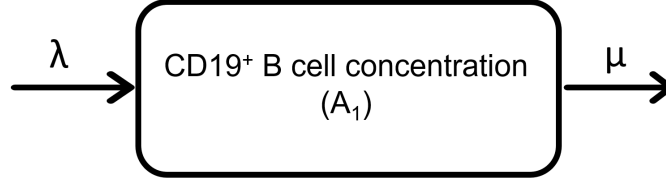


Figure 2.5: Schematic of final model of CD19<sup>+</sup> cell reconstitution. The central compartment represents the concentration of CD19<sup>+</sup> cells as measured in the peripheral blood at time  $t$  (days) after HSCT. New B cells produced by the bone marrow enter at zero-order rate  $\lambda$  and die at first-order rate  $\mu$ . The B cell maturation function was applied to  $\lambda$  and  $\mu$  to scale for age-related effects, and a sigmoidal Hill-type function was used to account for the delay in bone marrow output after HSCT.

### 2.3.3 Model Fitting

The one compartment turnover model was fitted to untransformed CD19<sup>+</sup> cell counts using the Laplacian conditional estimation with interaction algorithm in NONMEM version 7.4.3, with the ADVAN13 subroutine. The initial condition of the B cell compartment was set to  $5 \times 10^6$  cells/L (half of the LLOQ) on the day of HSCT. To handle the CD19<sup>+</sup> cell counts that were BLQ ( $n = 1111$ , 31.8%), both the M5 and M3 methods were tested, with the M3 method resulting in a greater reduction in OFV. A combined additive and proportional model best described the residual error. Both the Hill-type sigmoidal and Hoare functions were tested as possible mathematical representations of the delay in bone marrow output post-HSCT, with the sigmoidal Hill-type function producing a greater reduction in OFV.

### 2.3.4 Parameter Estimates

The parameter values estimated from the model-building dataset have been given in Table 2.4. Of note, the setpoint parameter was not estimated from the data but derived by dividing  $\lambda$  by  $\mu$  to provide a measure of the number of CD19<sup>+</sup> cells at steady-state. As another measure of CD19<sup>+</sup> cell turnover, a half-life for CD19<sup>+</sup> cells of 46.2 days was calculated using the estimate of  $\mu$  ( $t_{1/2} = \ln 2 / \mu$ ), with considerable variability for individual patients (range, 3.2 - 359.6 days). The model

predicted a mean delay of approximately two months for a child of median age 3.02 years to recover their bone marrow output after HSCT to 50% of its maximum capacity.

Table 2.4: Estimated parameter values. Setpoint parameter derived by dividing  $\lambda$  by  $\mu$ .  $\lambda$ , CD19<sup>+</sup> cell production rate constant;  $\mu$ , CD19<sup>+</sup> cell death rate constant;  $\gamma$ , Steepness of slope of CD19<sup>+</sup> cell recovery;  $T50$ , Time to half-maximal output of CD19<sup>+</sup> cells from bone marrow; RSE, relative standard error; BSV, between-subject variability; CI, confidence interval.

Parameter (Units)	Estimate (%RSE)	%BSV (%RSE)	Shrinkage (%)	Bootstrap Median (95% CI)
Setpoint (x 10 <sup>6</sup> cells/L)	*112 (-)	-	-	-
$\lambda$ (x 10 <sup>6</sup> cells/day)	1.68 (2.45)	115.76 (0.0011)	24.1	1.68 (1.36 - 2.05)
$\mu$ (cells/day)	0.015 (3.00)	113.58 (0.0061)	34.3	0.015 (0.013 - 0.018)
$\gamma$	4.17 (0.49)	-	-	4.17 (4.05 - 4.29)
$T50$ (days)	58.9 (1.07)	137.48 (0.0033)	32.1	58.3 (44.0 - 64.0)

The final parameter estimates tabulated above for the current model of CD19<sup>+</sup> cell reconstitution post-HSCT in children and the final parameter estimates from a published model of CD4<sup>+</sup> cell reconstitution post-HSCT in children<sup>106</sup> were used to plot the Hill-type and Hoare delay functions incorporated into these models respectively (Figure 2.6).

### 2.3.5 Covariate Effects

The covariates tested were a mixture of factors pertaining to the patient, donor, transplant, and drug administrations. Continuous covariates considered were age and CD4<sup>+</sup> T cell count. Categorical covariates considered were HSC source, serotherapy, gender, diagnosis of primary immunodeficiency, matched donor and myeloablative conditioning. All categorical covariates were dichotomous, with values set to 0 for the reference classification and 1 for the other classification. All parameter-covariate relationships were tested, and effects of covariates found to be significant were linearly parameterised by multiplication of the parameter by (1 + effect size).

Three covariates were found to significantly affect  $T50$  and were consequently incorporated into the

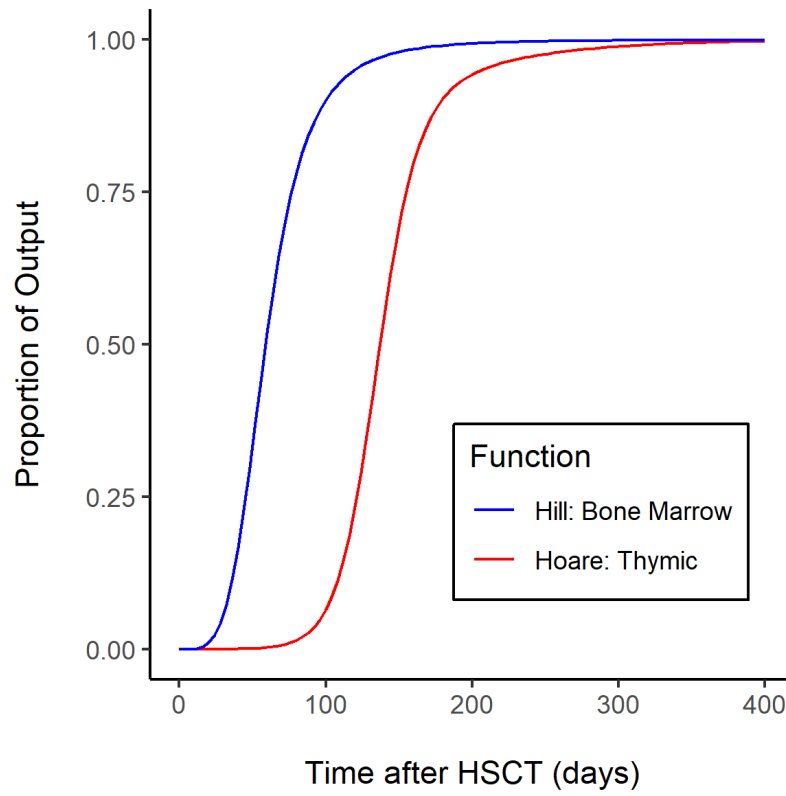


Figure 2.6: Proportion of thymic output/bone marrow output with time since HSCT. Blue line represents bone marrow output using Hill-type delay function in current model of  $CD19^+$  cell reconstitution post-HSCT and red line represents thymic output using Hoare function in model of  $CD4^+$  T cell reconstitution post-HSCT<sup>106</sup>.



base structural model. The three covariates are summarised in Table 2.5, and elaborated in turn below.

Table 2.5: Covariate effects identified using SCM. PID, primary immunodeficiency; MAC, myeloablative conditioning; RSE, relative standard error; CI, confidence interval.

Parameter	Covariate	Effect Size (% RSE)	Bootstrap Median (95% CI)
$T_{50}$	PID	-0.55 (0.16)	-0.55 (-0.595 - to -0.147)
$T_{50}$	MAC	0.17 (10.12)	0.17 (0.039 - 0.32)
$T_{50}$	Matched Donor	-0.001 (25.75)	0.007(-0.12 - 0.079)

### *PID*

Of the 359 study patients, 160 (44.6%) had an HSCT indication of PID and were identified as having a significantly different pattern of long-term  $CD19^+$  cell reconstitution compared to patients with other diagnoses. While the bone marrow of the typical patient required 58 days to recover to 50% of its maximum  $CD19^+$  cell production capacity, patients with PID required 32 days, i.e. a decrease of 55%, to recover their bone marrow output to the same extent.

### *MAC*

The time taken to recover 50% of bone marrow output was also affected by the type of conditioning regimen. Patients who received a MAC regimen ( $n = 161$ , 44.8%) took approximately 68 days to recover their bone marrow output to 50% capacity. This was a 17% increase compared to patients who received either RIC, MIC or no conditioning regimens who took 58 days.

### *Matched Donor*

More than two-thirds of the study patients received HSCs from a HLA-matched donor ( $n = 259$ , 72.1%). These patients were found to have a statistically significant but biologically negligible difference (an increase of 0.5 days) in the time taken to recover their bone marrow output to 50% capacity.

## 2.3.6 Model Evaluation

The series of goodness-of-fit plots in Figure 2.7 and the age-stratified prediction-corrected visual predictive checks (pcVPC) in Figure 2.8 were produced to evaluate the model. To construct the pcVPC, 200 datapoints were simulated from the parameter values estimated by the model. The

patients in the model-building dataset consisted of infants ( $< 2$  years,  $n = 148$ ), children ( $\geq 2$  years and  $< 12$  years,  $n = 189$ ), and adolescents ( $\geq 12$  years,  $n = 22$ ) therefore the pcVPC was stratified by age to ascertain the performance of the B cell maturation function. The fraction of data that were BLQ of  $10 \times 10^6/\text{L}$  are also visualised as part of the pcVPC.

In general, model evaluation indicated no discrepancies between the observed data and model-predicted data. On first glance, the local regression curve of the plot of observed data against population predictions may suggest refinement of the structural model, but can be explained by the inclusion of the BLQ observations in the plot. The plot of observed data against individual predictions demonstrated a good fit, with data clustering more along the line of unity. Regarding the residual error model, the plot of the conditional weighted residuals (CWRES) against time since HSCT showed a normal distribution with a mean of zero, with most of the data between  $\pm 2$  standard deviations of the mean and no pattern developing with time since HSCT. In addition, the plot of the absolute individually weighted residuals (IWRES) against individual predictions depicts most of the data points scattered along a flat line, with some perturbations due to the inclusion of the BLQ data.

The pcVPC demonstrates consistency between the observed data and simulated percentiles. There is considerable variability observed for adolescents due to the low number of patients in this age group compared to infants and children.

Lastly, the model parameter values were estimated with good precision, indicated by the low standard error. This was corroborated by performing a non-parametric bootstrap ( $n = 1000$ ), which generated median values comparable to the parameter estimates.

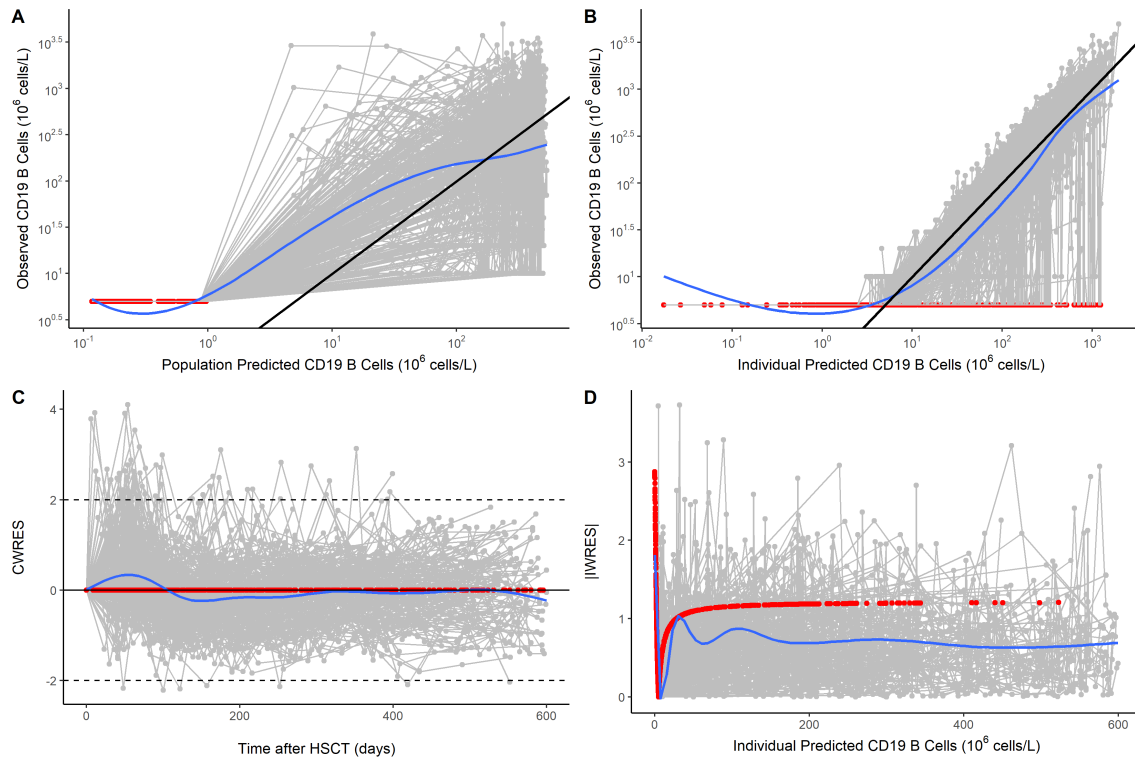


Figure 2.7: Goodness-of-fit plots. A) Observed CD19<sup>+</sup> cell counts vs Population Predicted CD19<sup>+</sup> cell counts. B) Observed CD19<sup>+</sup> cell counts vs Individual Predicted CD19<sup>+</sup> cell counts. C) CWRES vs Time. D) |IWRES| vs Individual Predicted CD19<sup>+</sup> cell counts. Blue lines are the local regression curves and red datapoints are those that were BLQ.

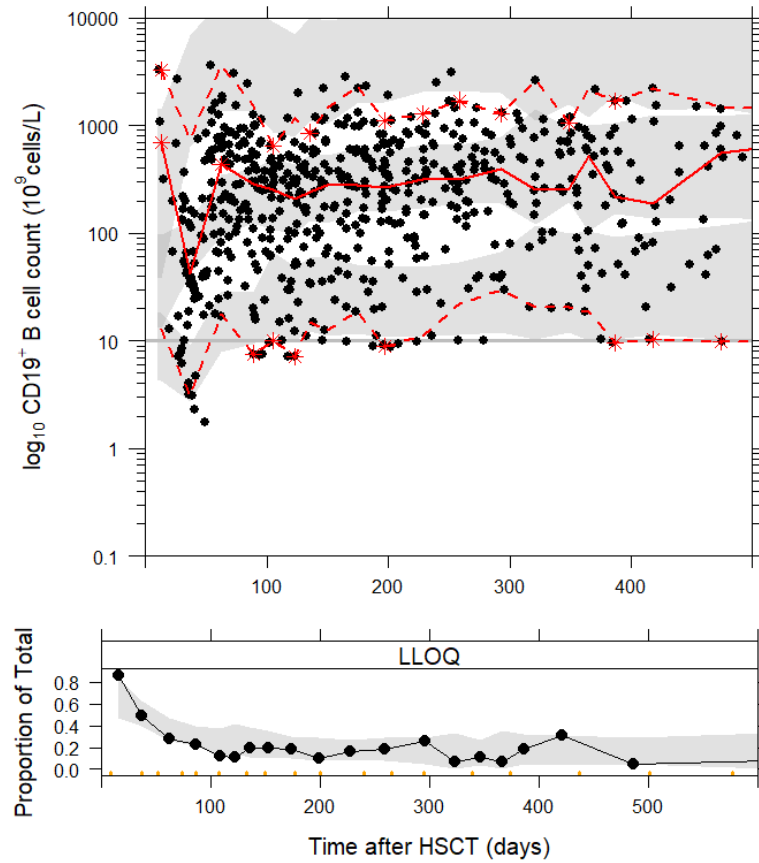
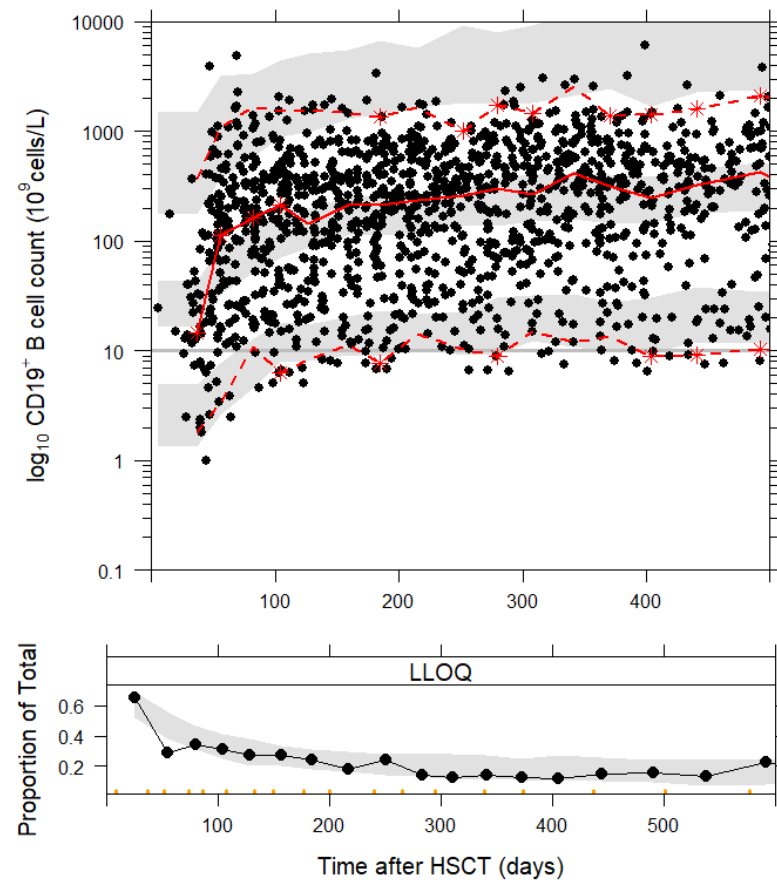
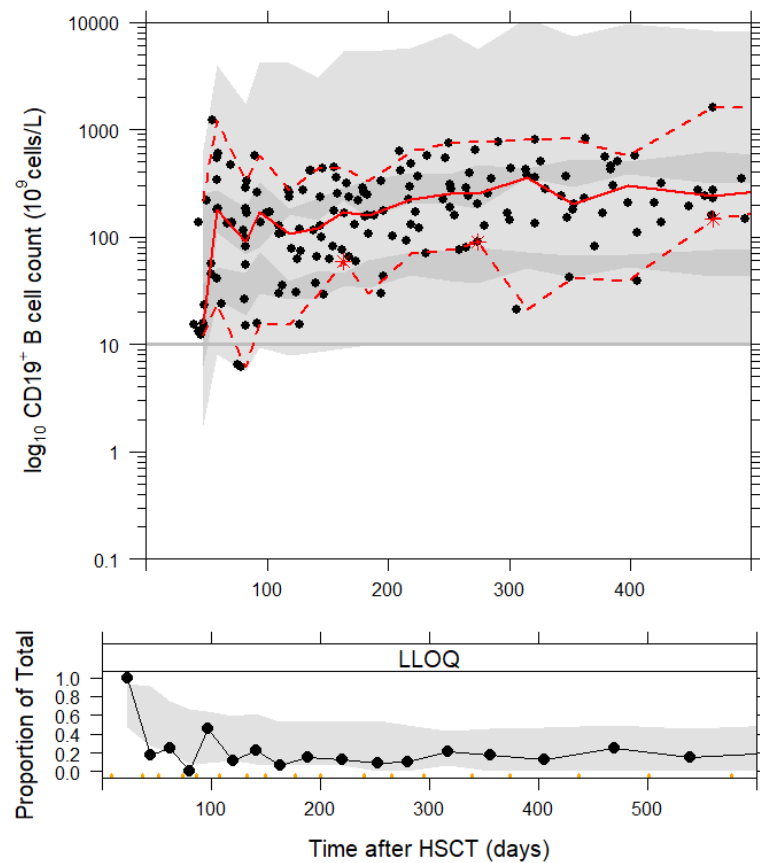


Figure 2.8: Prediction-corrected Visual Predictive check for final model stratified by age groups in order of infants, children and adolescents. Black dots are observed data and the solid red line is the observed median. The dotted red lines are the observed 2.5th, 50th and 97.5th percentiles and the grey shaded area are the 95% prediction intervals. The bottom part of the panel shows the proportion of the total data that were BLQ.





## 2.4 Discussion

The majority of previous studies of post-HSCT immune reconstitution have focussed on T cells and adult patient cohorts therefore we aimed to address the need to better understand B cell reconstitution in children post-HSCT using a modelling approach. To the best of the author's knowledge, this is the first mechanistic NLME model of CD19<sup>+</sup> B cell reconstitution post-HSCT in children. Prior biological knowledge was integrated into the model to scale for age-related effects and to quantify the delay in recovery of bone marrow output following HSCT. In addition, the effect of clinically relevant covariates was assessed, highlighting the model's potential to be used in clinical management as a tool to predict individualised patient trajectories of CD19<sup>+</sup> B cell reconstitution.

In general, the model estimated mean parameter values that were biologically plausible. Previous *in vivo* labelling studies have investigated B cell kinetics in humans in health and disease<sup>178,179</sup>. Assuming zero-order proliferation and first-order death, when the mean proliferation and disappear-

ance rates reported by Macallan *et al* for young healthy adults (35 years or younger) is multiplied by the absolute CD19<sup>+</sup> B cell count measured by Morbach *et al* for 19-25 year olds, we obtain average CD19<sup>+</sup> B cell production and turnover rates of approximately  $3.06 \times 10^6$  cells/day and 0.017 cells/day respectively for young healthy adults<sup>54,178</sup>. Notably, the derived turnover rate aligns with the model estimate of 0.015 cells/day (95% CI:0.013-0.018) for  $\mu$ , while the derived proliferation rate is higher than the model-estimated value of  $1.68 \times 10^6$  cells/L(95% CI:1.36-2.05) for  $\lambda$ . This perceived difference may be an artefact of the modelling methodology employed, which the authors indicated may result in higher proliferation rates, and the small sample size ( $n = 8$ ) as well as the lack of scaling of B cell proliferation and death rate parameters<sup>178</sup>. Similarly, Defoiche *et al* did not observe a significant difference in B cell kinetics between young and elderly healthy adults, again likely attributed to the absence of scaling to account for age-related effects<sup>179</sup>. Indeed, the final NLME model estimated a mean parameter value of  $4.55 \times 10^6$  cells/L for  $\lambda$  when the B cell maturation function was omitted, highlighting its essential role in scaling B cell dynamics for age. Interestingly, our estimate for  $\mu$  of 0.015 cells/day in children falls at the lower end of a range of B cell turnover rates measured in animals, namely sooty mangabeys (mean 0.018 cells/day)<sup>180</sup>, rhesus monkeys (mean 1.8 cells/day)<sup>181</sup>, mice (0.032-0.4 cells/day)<sup>182</sup> and sheep (0.09 cells/day)<sup>183</sup>, perhaps suggesting that elements of the mechanisms governing B cell homeostasis may be conserved across species. Furthermore, the assumption that CD19<sup>+</sup> B cell turnover follows a pattern of first-order kinetics is supported by both experimental and modelling studies<sup>184,185</sup>. In addition, the derived mean turnover half-life for CD19<sup>+</sup> B cells of 46.2 days (range, 3.2 - 359.9 days) is consistent with several reports that observed a half-life ranging from 12 days to 9 weeks<sup>178,179,184</sup>.

Despite the paucity of modelling studies of B cell reconstitution post-HSCT in children, we build on the recent findings of van der Maas *et al*, who used linear mixed effects modelling to identify donor age, recipient age and time after HSCT as significantly influencing B cell reconstitution in children post-HSCT<sup>186</sup>. With comparable inclusion criteria, the authors investigated the B cell counts of children from 0-18 years for up to two years post-HSCT, also excluding patients who received rituximab<sup>186</sup>. We have developed their work by including a B cell maturation function to account for the effect of age, used a non-linear modelling approach on a larger paediatric cohort (present model,  $n = 359$ ; van der Maas *et al*,  $n = 233$ ) and considered additional factors influencing B cell reconstitution using covariate model building.

To construct the B cell maturation function, work by Payne *et al* was leveraged, who were the first to quantify naive B cell output in HIV-uninfected and HIV-infected children by combining KREC levels, Ki67 expression and measurements of naive B cell counts<sup>146</sup>. By applying the authors' proposed model of naive B cell output to the post-HSCT setting, inferences on bone marrow output post-HSCT could be made and related to CD19<sup>+</sup> cell reconstitution, demonstrating its clinical relevance in this context<sup>146</sup>. With respect to the NLME model, the  $T50$  parameter, estimated to be

58 days, represented the time taken for the bone marrow to recover to 50% of its maximal output and is therefore a measure of long-term CD19<sup>+</sup> B cell reconstitution. This finding is in line with experimental studies that observed CD19<sup>+</sup> transitional B cells first appearing in the peripheral blood between one to two months post-HSCT<sup>98,118</sup>. Furthermore, the time delay of 58 days is consistent with KRECs measurements that correlated with the appearance of transitional B cells, indicative of B cell neogenesis at that timepoint<sup>137,139,187</sup>.

Using the SCM method, three covariates were identified as significantly affecting CD19<sup>+</sup> B cell reconstitution; PID diagnosis, MAC regimen and a matched donor. Patients with PID took 32 days to recover 50% of their maximum bone marrow output while patients with other diagnoses took 58 days. This is largely explained by the difference in age between the two patient groups; non-PID patients had a median age of 4.85 years at HSCT while PID patients had a much younger median age at HSCT of 1.75 years, which coincides with the age when peak bone marrow output is expected to occur in line with Payne *et al*<sup>146</sup>. Therefore, their much faster reconstitution can largely be attributed to the established biological mechanism of increased bone marrow at younger ages<sup>54,119,171</sup>. In addition, the majority of PID patients ( $n = 121$ , 75.6%) did not receive lymphocyte-depleting serotherapy drugs, which have been reported to delay B cell reconstitution by 54 days<sup>98</sup>, most likely due to their long half-lives<sup>188,189</sup>. Lastly, PID patients received either RIC, MIC or no conditioning, which are collectively less toxic to the bone marrow than MAC. Taken together, this may result in PID patients having a higher initial concentration of B cells at HSCT compared to their non-PID counterparts.

Another significant covariate was having a MAC regimen, which marginally increased the time to recover bone marrow output from 58 days to 68 days. A large proportion of patients who received MAC also had a stem cell source of BM ( $n = 100$ , 62.1%), which has been shown in some studies to result in slower B cell reconstitution compared to PBSC or CB seemingly corroborating our finding<sup>62,66</sup>. In contrast, others have reported favourable B cell reconstitution with a MAC regimen due to high donor chimerism therefore the interpretation of this result remains unclear<sup>126,127</sup>.

Covariate model building also revealed having a matched donor to be statistically significant, although its biological significance requires further investigation, given the negligible increase of 0.5 days to recover bone marrow output. It does not seem to be a question of selection bias (72% of patients had a matched donor,  $n = 259$ ) but perhaps indicates that a more granular classification of donor type beyond the dichotomous classification used would be warranted to correctly delineate the effect of donor type<sup>190</sup>.

In summary, a novel mechanistic NLME model of CD19<sup>+</sup> B cell reconstitution post-HSCT in children has been developed. Using relevant prior knowledge of immunobiology, a B cell maturation function was constructed to scale B cell dynamics for age, which enables the application of this model to data across the human lifespan. In addition, the model has potential for use in other



clinical scenarios where B cell recovery is expected after an insult to the immune system, for which disease-specific or mechanism-specific parameters that are biologically relevant may be added in place of the HSCT-related parameters. Despite being a single-centre study, the large paediatric cohort and resulting rich dataset allowed the estimation of parameters and covariates involved in CD19<sup>+</sup> B cell reconstitution with good precision. Nonetheless, there are limitations to this work. Although a portion of the data were BLQ ( $n = 1111$ , 31.8%), these were handled well using the M3 method. The model is yet to be validated using previously unseen patient data, whether internal data from GOSH or external data from another HSCT centre, which is necessary to assess predictive performance. The age-stratified pcVPC illustrates that the B cell maturation function accounts for age differences and that the simulated data captures the overall trend of the observed data. Model validation should help to reconcile the variability observed for the adolescent age group, of which there were only 22 in the dataset. Another possible limitation arises from the data used to construct the Ki67 component of the B cell maturation function, built using data from Ki67 quantification in naive B cells of healthy South African children<sup>146</sup>. Recent evidence has suggested variation in the maturation of the immune system depending on geographical location, attributed to differences in environmental stimuli and pathogens<sup>191,192</sup>. This may result in healthy South African children having more activated immune systems and could warrant further refinement of the maturation function to ensure consistency with the naive B cell component built using naive B cell counts measured in European children.

## Chapter 3

# Rituximab Pharmacodynamics in EBV Reactivation

### 3.1 Introduction

#### 3.1.1 Epstein-Barr Virus

First discovered in 1964 in lymphoma samples from children, Epstein-Barr virus (EBV), also known as human herpesvirus 4, is a member of the *Herpesviridae* family of viruses well-known for their propensity to establish lifelong infections in the host<sup>193</sup>. Other notable members include human CMV and *Varicella zoster* virus. In humans, EBV is transmitted via bodily fluids, blood transfusions and organ transplantation, and is the cause of infectious mononucleosis, B cell lymphomas and leukaemias such as Burkitt lymphoma and epithelial cancers such as nasopharyngeal carcinoma<sup>194–197</sup>. Its life cycle is characterised by lytic and latent phases of viral replication, with 90% of adults harbouring an asymptomatic latent EBV infection, usually acquired during childhood<sup>198</sup>. In terms of its genetic structure, an EBV virion has a double-stranded DNA genome enclosed by a protein capsid, which is surrounded by a protein tegument<sup>199</sup>. The outermost structural features of the virion are the envelope proteins found on its surface, which are responsible for attachment and entry into its target cells, epithelial cells and B cells, followed by uncoating, replication, assembly and release of the virus to infect further host cells<sup>199</sup>. Examples of interactions between key viral envelope glycoproteins with surface proteins of B cells include gp350 with CD21 and gp42 with MHC Class II<sup>200,201</sup>. Upon primary infection, EBV activates the B cell growth programme to trigger B cell proliferation, and immunocompetent hosts respond in parallel via the

priming of naive T cells by APCs that recognise EBV antigen as foreign peptide<sup>198,202</sup>. As a result, naive T cells differentiate into EBV-specific cytotoxic T cells and destroy the EBV-transformed blasting B cells thereby containing further propagation of the virus. To evade the host immune response and establish persistence, EBV expresses latency-associated genes to halt lytic replication and allow the virus to reside in resting memory B cells in peripheral blood thus maintaining a stable long-term viral reservoir<sup>27,199,203</sup>.

### 3.1.2 EBV Reactivation

In EBV-seropositive individuals, a circulating pool of EBV-specific cytotoxic T cells are sufficient to control periodic reactivations<sup>204</sup>. However in immunocompromised patients, reduced immune surveillance due to a reduced number of cytotoxic T cells leads to an opportunistic outgrowth of blasting EBV-infected B cells and consequently, a reversion to lytic replication and therefore reactivation of EBV. In the post-HSCT setting, EBV reactivation is the leading cause of post-transplant lymphoproliferative disorder (PTLD), with patients at higher risk if they receive selective T cell depletion with ATG, a RIC regimen, which usually incorporates ATG, or have low histocompatibility with their donor<sup>205–207</sup>. For this reason, EBV is monitored on a regular basis during the follow-up period post-HSCT, especially in the first three months when reactivation is most likely to occur. In the case of PTLD, EBV DNA can exist in both cell-associated and cell-free forms therefore sampling peripheral whole blood ensures that both forms are captured to allow for accurate measurement of EBV levels; EBV DNA is measured using quantitative real-time polymerase chain reaction (qPCR)-based assays followed by quantification of viral load (VL) using cycle threshold (Ct) values<sup>208</sup>.

While it is widely appreciated that elevated EBV VL is informative in diagnosing PTLD, there is no international agreement on the threshold of EBV VL that must be exceeded to begin treatment and it continues to be debated what order of magnitude of elevation in EBV VL is clinically meaningful<sup>209,210</sup>. VLs are not a direct measure of the amount of virus in the blood at any one time-point, as they are calculated indirectly from Ct values from qPCR assays which may be sufficiently reliable to monitor viral trends over time but may be inaccurate for accurately detecting PTLD onset<sup>208</sup>. In addition, there is no clear consensus on when, how often or which blood component is best to monitor such that VL measurements from two different laboratories cannot be compared due to inter-laboratory technical differences such as the viral reference strain used to generate standards or the DNA extraction method used<sup>210</sup>. In light of this, the World Health Organisation published the first International Standard for Epstein-Barr virus for Nucleic Acid Amplification Techniques to aid standardisation of assay results<sup>211</sup>. The predictive value of EBV viral loads is improved when considered in conjunction with cut-off thresholds for circulating T cells and absolute

lymphocyte count therefore they remain a mainstay of current treatment schema for the diagnosis and clinical management of EBV-related PTLT. No antiviral drugs or vaccines are available to cure EBV. Anti-inflammatory drugs can be prescribed to alleviate symptoms of pain and fever, and in patients with significant EBV viraemia post-HSCT, therapy is usually a combination of rituximab administration and reduction of immunosuppression, with EBV-specific CTLs or chemotherapeutic drugs considered in progressive cases<sup>208</sup>.

### 3.1.3 Rituximab

Rituximab is a chimeric monoclonal antibody that interacts with the CD20 transmembrane protein on the surface of B cells and targets it for depletion<sup>212</sup>. Originally approved in 1997 for the treatment of Non-Hodgkin's B cell lymphoma, rituximab was the first anti-cancer therapeutic antibody licensed by the Food and Drug Administration (FDA) in the United States, and was licensed a year later by the European Medicines Agency (EMA)<sup>213</sup>. It is now widely prescribed for a range of other conditions including B cell leukaemias and autoimmune diseases, and was recently approved for selected paediatric indications for the first time<sup>214</sup>. In addition, rituximab is commonly and increasingly prescribed for indications not covered by its licence, i.e. on an off-label basis<sup>215,216</sup>, including for EBV reactivation post-HSCT in both adults and children<sup>217–224</sup>. Manufactured by Roche, rituximab is marketed as MabThera in Europe and as Rituxan in the United States, China and Japan. The current licensure for rituximab has been summarised in Table 3.1.

Table 3.1: Current licensure for rituximab. EMA, European Medicines Agency; FDA, Food and Drug Administration. NHL, Non-Hodgkin's B cell lymphoma; CLL, Chronic lymphocytic leukaemia; RA, Rheumatoid arthritis; MPA, Microscopic polyangitis; GPA, Granulomatosis with polyangitis; PV, Pemphigus vulgaris; DLBCL, Diffuse large B cell lymphoma; BL, Burkitt's lymphoma; BAL, B-cell acute lymphoma.

EMA Approval - Patent Expiry	FDA Approval - Patent Expiry	Target Population	Indications
1998 - 2013	1997 - 2016	Adult	NHL, CLL, RA, MPA, GPA, PV

EMA Approval - Patent Expiry	FDA Approval - Patent Expiry	Target Population	Indications
2020 -	2019 -	Paediatric	MPA, GPA; previously untreated advanced stage CD20 <sup>+</sup> DLBCL, BL, BAL, BLL ( $\geq 6$ months to $<18$ years)

Following the expiration of rituximab's patent in 2013 and 2016 in Europe and the United States respectively, biosimilars of rituximab are emerging in clinical use<sup>225</sup>. A biosimilar is defined as a biological product that is highly similar to and has no clinically meaningful differences from an existing approved 'reference' product<sup>226</sup>. The administration of rituximab biosimilars for children with rheumatological disease will be explored in Chapter 5. Details of the PK and PD of rituximab are given below.

### 3.1.3.1 Pharmacokinetics

The structure of rituximab is comprised of a human-derived immunoglobulin G-1 (IgG-1) constant region and a murine-derived variable region, which has the capacity to bind specifically to two CD20<sup>+</sup> antigens via its antigen-binding domains (Figure 3.1). The baseline B cell count determines the level of circulating target CD20<sup>+</sup> antigen available to bind to rituximab hence greatly influences its efficacy. Given its chimeric nature, rituximab has the potential to trigger production of anti-drug antibodies<sup>227</sup> although this remains as a low risk, with immunogenicity reported as  $<1\%$  to  $10\%$  in the majority of cases<sup>228</sup>. It is usually administered via intravenous infusion, with a single dose constituting  $375\text{mg}/\text{m}^2$  and a typical regimen consisting of up to four doses given on a weekly basis. Regarding its absorption, rituximab is absorbed through lymph and blood vessels due to its size of  $150\text{kDa}$ <sup>229</sup> and is transported via convection to its pharmacological target, the CD20<sup>+</sup> antigen on the surface of B cells<sup>230</sup>. Circulating B cells are therefore targeted directly. The volume of distribution of rituximab at steady-state has been reported to range from  $6.62 - 9.6\text{L}$  suggesting a greater distribution in plasma than in tissue<sup>231,232</sup>, specifically in the blood and interstitial space<sup>233</sup>. Rituximab usually exhibits linear PK elimination but target-mediated drug disposition (TMDD) has been reported, and modelled, for rituximab in specific oncology indications and anti-neutrophil cytoplasmic antibody (ANCA)-associated vasculitis (AAV)<sup>234,235</sup>. This may be due to retention of rituximab by non-depleted B cells, such as those present in metabolic tumour volume, and different rates of rituximab clearance from different tissues<sup>234,236</sup>. The metabolism and elimination of rituximab is determined by a combination of specific binding to its target receptor, CD20<sup>+</sup>,

and non-specific binding, mediated by  $Fc_\gamma$  receptors, which can give rise to a biphasic PK profile displaying both linear and non-linear behaviour<sup>237</sup>. Metabolism of rituximab to peptides and amino acids is attributed to its non-specific binding pathway<sup>238</sup>. Specific binding of rituximab to  $CD20^+$  takes place until saturation is reached leading to a high initial time-dependent clearance and non-linear elimination followed by a second phase of non-specific binding of rituximab mediated by  $Fc_\gamma$  receptors resulting in slower time-independent clearance and linear elimination<sup>237,239,240</sup>. TMDD combined with phagocytosis via the reticuloendothelial system are thought to make up the routes of elimination<sup>239</sup>. The long elimination half-life observed for rituximab, which can be up to 4 weeks, is explained by its binding to the neonatal Fc receptor (FcRn), which serves as a protective mechanism against lysosomal degradation<sup>241</sup>.

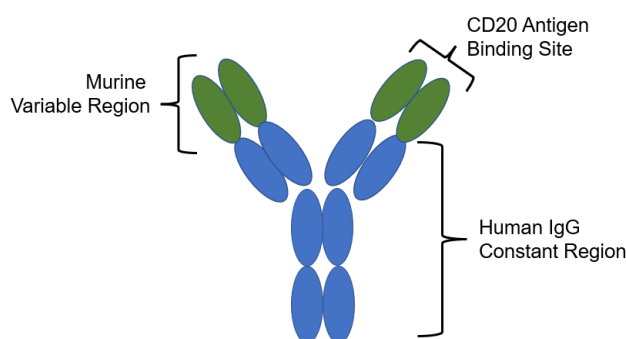


Figure 3.1: Chimeric structure of rituximab.  $CD20^+$ , cluster of differentiation 20; IgG, immunoglobulin G.

### 3.1.3.2 Pharmacodynamics

The primary PD effect of rituximab is depletion of all B cells expressing the  $CD20^+$  antigen, which includes pre-B cells, early immature B cells, naive B cells and mature memory B cells, whether they are malignant or not<sup>242</sup>. The mechanisms of B cell lysis are a combination of direct induction of apoptosis, antibody-dependent cellular cytotoxicity and complement-dependent cytotoxicity<sup>243</sup>. The resulting B cell suppression is profound and can last up to 6 months after cessation of therapy although B cell counts recover to normal levels in the long-term<sup>244</sup>. Variability in the clinical and biological response to rituximab with regards to extent and duration of B cell depletion has been documented due to disease activity, co-medications, variable dosing regimens, patient factors and biological mechanisms of resistance to rituximab<sup>245</sup>.

Given its mechanism of action, a common side-effect of rituximab administration is hypogammaglobulinaemia resulting from a reduced capacity for antibody production pertaining to the global

reduction in B cell counts. This is clinically managed by the administration of intravenous immunoglobulin (IVIg) to supplement or replace immunoglobulins<sup>246,247</sup>. Reconstitution of the B cell compartment following rituximab therapy is driven by pro-B cells and HSCs, which are both subsets of B cell precursors that do not express CD20<sup>+</sup> and are therefore not depleted by rituximab<sup>213</sup>. Similar to B cell reconstitution following HSCT<sup>118,248</sup>, ontogenic B cell reconstitution has been reported after rituximab administration driven by production of naive B cells from HSCs in the bone marrow<sup>249</sup>. This has even been observed in neonates whose mothers received rituximab before and during pregnancy for multiple sclerosis and related conditions<sup>250</sup>.

In recent years, confounding factors in the analysis of the exposure-response relationship have been recognised and characterised for monoclonal antibodies in immuno-oncology<sup>252</sup>, together with mitigation strategies. This may have relevance for rituximab given its complex PK.

### 3.1.3.3 Pharmacometric Models

A number of population PK models of rituximab have been developed to date, mainly for oncology and autoimmune disease. The majority of these were built using adult data, with a handful focussed on paediatrics<sup>185,214,253,254</sup>.

The first pharmacometric model of rituximab was the two compartment linear PK model reported by Ng *et al* in adult rheumatoid arthritis patients<sup>231</sup>, in which rituximab was dosed intravenously into the central compartment and had its effect in the peripheral compartment. Parameterised by clearance, volume and distribution rate constants between the two compartments, the authors found significant covariate effects of body surface area and gender on both clearance and volume.

Subsequent studies reported rituximab PK models for B cell leukaemias and lymphomas, in which rituximab was administered in combination with chemotherapy regimens such as the cyclophosphamide, doxorubicin, vincristine and prednisolone (CHOP) regimen<sup>232,255–257</sup> and fludarabine and cyclophosphamide<sup>258</sup>. With the exception of Muller *et al* who investigated elderly patients with DLBCL<sup>232</sup>, most study populations had a median age of approximately 50 years. All models used a two-compartment model structure, sometimes estimating additional PK parameters such as volume of distribution and reporting other covariate effects such as gender, body-mass index and body size<sup>232,240</sup>. Gibiansky *et al* characterised rituximab PK for patients administered a subcutaneous formulation in addition to the usual intravenous infusion<sup>240</sup>. Several models related rituximab PK to clinical outcomes such as tumour burden<sup>255,257</sup>. To represent the TMDD of rituximab, some models included a specific time-dependent clearance to account for TMDD, i.e., non-linear PK, as well as a non-specific time-independent clearance term to reflect linear PK<sup>240,256,258</sup>.

Rituximab PK models in the paediatric population are scarce with only two published models reported to date. Chen *et al* studied patients with nephrotic syndrome who were prescribed rituximab.

uximab off-label<sup>254</sup>, and Jamois *et al* conducted a Phase 2 study to determine dosing regimens of rituximab in paediatric patients with GPA/MPA, which ultimately led to regulatory approval of rituximab in paediatrics for the first time for these indications<sup>214</sup>. Whilst they did not develop a model, Barth *et al* described rituximab PK in children and adolescents with mature B-NHL using non-compartmental analysis<sup>253</sup>.

Of note, there are a distinct lack of rituximab PD models in the current literature, with no published adult models and one pediatric model by Pan *et al*<sup>185</sup>. To the best of the author's knowledge, there are no published adult or paediatric models for rituximab PD in post-HSCT patients with EBV reactivation.

PBPK approaches for modelling the PK of monoclonal antibodies such as rituximab have also been studied<sup>259,260</sup>, alongside the PK and PD studies described above.

In general, most previous pharmacometric models of rituximab have noted high interindividual variability in clinical response to rituximab.

### 3.1.4 Aim

This project aimed to develop a mechanistic NLME model to quantify the pharmacodynamics of rituximab on CD19<sup>+</sup> cell reconstitution in children with EBV reactivation post-HSCT.

### 3.1.5 Objectives

- Clean patient electronic data of retrospective CD19<sup>+</sup> cell counts, rituximab dosing and other covariates
- Incorporate mathematical function into Chapter 2 mechanistic NLME model of CD19<sup>+</sup> cell reconstitution post-HSCT to quantify rituximab drug effect
- Evaluate model by performing diagnostic checks to compare model-predicted and observed data

## 3.2 Methods

### 3.2.1 Data

Retrospective electronic data from routine clinical practice were collected from children who underwent HSCT at the Bone Marrow Transplant Unit at GOSH between 2000 and 2016. Patients who received rituximab for EBV reactivation were identified as shown in the flow diagram in Figure 3.2.



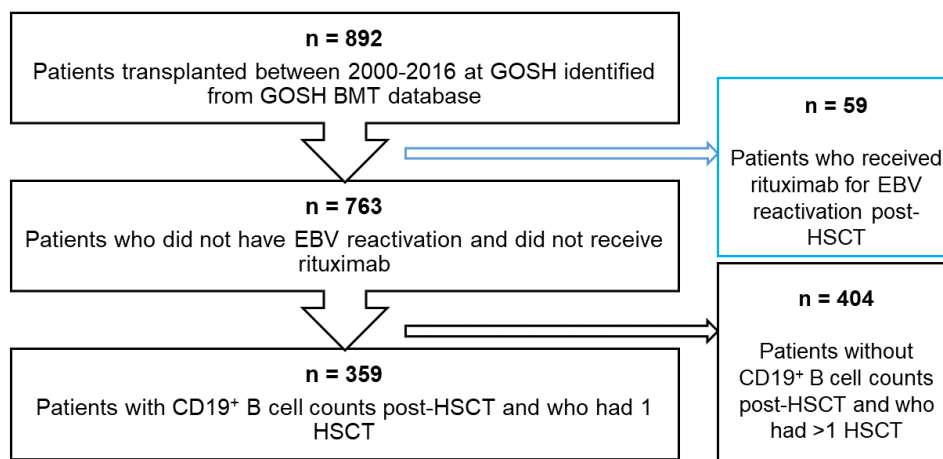


Figure 3.2: Flow diagram of study patients. Box in blue represents patients considered for current study ( $n = 59$ ). GOSH, Great Ormond Street Hospital; BMT, Bone Marrow Transplant; EBV, Epstein-Barr virus; HSCT, Haematopoietic stem cell transplant.

Three inclusion criteria were applied; that patients had:

- Measurements of CD19<sup>+</sup> cell counts post-HSCT
- Undergone their first HSCT
- Not received rituximab for indications other than for EBV reactivation

Data comprised CD19<sup>+</sup> cell counts from immunophenotyping prior to and following rituximab administration, measured in  $10^6$  cells/L of blood from immunophenotyping using flow cytometry, as well as measurements of other immune cell subsets and patient-specific, donor-specific and transplant-specific variables. Regarding sensitivity of the assay to detect lymphocytes, 10,000 events were targeted in the lymphocyte gate.

### 3.2.2 Rituximab Therapy

Rituximab was administered via intravenous infusion at a dose of  $375 \text{ mg/m}^2$  weekly, with patients receiving a single dose on a conservative regimen or four doses on a pre-emptive regimen. Patients administered a single rituximab dose underwent HSCT during the years 2011-2016 whereas patients

who received four rituximab doses were from a historical cohort transplanted in the period 2005-2009 treated using a pre-emptive strategy, originally studied by Worth *et al*<sup>38</sup>.

### 3.2.3 Incorporating Rituximab Effect

As the model-building dataset was constructed using retrospective data from routine clinical practice, serum drug concentrations of rituximab over time were not measured hence rituximab PK data were not collected. Therefore, to model the effect of rituximab on CD19<sup>+</sup> cell reconstitution post-HSCT, a kinetic-pharmacodynamic (K-PD) modelling approach was used, utilising the rituximab dose amount and the number of doses (either one or four), which were known. Rituximab was administered by intravenous infusion, with a single dose constituting 375mg/m<sup>2</sup>. Doses were converted to absolute doses using body weight and the Boyd formula prior to modelling<sup>261</sup>.

The mechanistic NLME model of CD19<sup>+</sup> cell reconstitution post-HSCT in Chapter 2, as given below, was used as the basis of model development,

$$\frac{dA_1}{dt} = \lambda \cdot \left( \frac{T^\gamma}{T^\gamma + T50^\gamma} \right) - \mu(A_1), \quad (3.1)$$

where  $A_1$  represents the central B cell compartment,  $\lambda$  is the CD19<sup>+</sup> cell production rate constant,  $\mu$  is the CD19<sup>+</sup> cell death rate constant,  $\gamma$  is the Hill exponent for steepness of slope of CD19<sup>+</sup> cell recovery and  $T50$  is the time to half-maximal output of CD19<sup>+</sup> cells by the bone marrow. In addition, the B cell maturation function was applied *a priori* to  $\lambda$  and  $\mu$  to scale them for age as follows,

$$\lambda = TV_\lambda \cdot w(t) \cdot z(t), \quad (3.2)$$

$$\mu = TV_\mu \cdot z(t), \quad (3.3)$$

where  $TV_\lambda$  is the typical value of  $\lambda$  for an adult scaled for age by  $w(t)$  and  $z(t)$ ,  $z(t)$  is the fraction of naive B cells expressing Ki67 with age,  $w(t)$  is the naive B cell count per unit volume blood with age and  $TV_\mu$  is the typical value of  $\mu$  for an adult scaled for age by  $z(t)$ .

The  $E_{max}$  model is the most frequently used model for describing drug effect in humans and has its foundation in receptor theory, based on the concentration of a drug-receptor complex leading to the effect of a drug<sup>262</sup>. The mathematical equation for the  $E_{max}$  model is as follows;

$$E = \left( \frac{E_{max} \cdot C}{EC_{50} + C} \right) \quad (3.4)$$

where  $E$  is the drug effect,  $E_{max}$  is the maximal drug effect,  $C$  is the drug concentration and  $EC_{50}$  is the drug concentration at which  $E$  is 50% of the  $E_{max}$ . Under the assumption that rituximab increases the death rate of CD19<sup>+</sup> cells, i.e., has a stimulatory effect on  $\mu$ , the  $E_{max}$  model was applied to  $\mu$  to incorporate the drug effect of rituximab. This assumption was also made in previous rituximab PK models<sup>185,255</sup>.

As rituximab concentration data were not available, the rituximab dose required to produce 50% of  $E_{max}$ ,  $ED_{50}$  was considered instead of  $EC_{50}$ . The expected response when no rituximab is present on  $\mu$  is zero therefore 1 was added to the  $E_{max}$  model to allow  $\mu$  to revert to itself.

The equations for the final structural model of the rituximab K-PD model were as follows, with the addition of a dosing compartment,  $A_2$ , and the model now estimating three additional parameters related to rituximab; apparent elimination rate constant ( $k_e$ ), apparent maximum killing effect of rituximab on CD19<sup>+</sup> cells ( $E_{max}$ ), and the rituximab dose required to produce 50% of the apparent maximum killing effect ( $ED_{50}$ ).

$$\frac{dA_1}{dt} = -k_e \cdot (A_1), \quad (3.5)$$

$$\frac{dA_2}{dt} = \lambda \cdot \left( \frac{T^\gamma}{T^\gamma + T^{50\gamma}} \right) - \mu \cdot \left( 1 + \frac{E_{max} \cdot A_1}{ED_{50} + A_1} \right) \cdot A_2 \quad (3.6)$$

Three assumptions were made regarding rituximab; that none was present in the dosing compartment on the day of HSCT, that its elimination followed first-order kinetics and that it increased  $\mu$ .

## 3.3 Results

### 3.3.1 Patient Characteristics

The model was constructed with 619 measurements of CD19<sup>+</sup> cell counts from 55 children (median age at HSCT, 3.0 years; range, 0.6-14.5 years); the raw data used for model-building is shown in Figure 3.3. The study period was for two years post-HSCT therefore a cut-off of 730 days post-HSCT was used for measurements of CD19<sup>+</sup> cell counts. In general, the patients were representative of a typical paediatric HSCT cohort and their characteristics are summarised in Table 3.2.

Table 3.2: Patient and transplant characteristics for model-building dataset for rituximab model. \* denotes one patient who did not receive serotherapy.

	Total Patients (n = 55)
<b>Age (years), median (range)</b>	3.0 (0.6 - 14.5)
<b>Diagnosis, n (%)</b>	
PID	18 (32.7)
NMH	12 (21.8)
MH	15 (27.3)
Other	10 (18.2)
<b>Donor Type, n (%)</b>	
MSD	5 (9.1)
MFD	4 (7.3)
MUD	28 (50.9)
MMFD	2 (3.6)
MMUD	15 (27.3)
Haplo	1 (1.8)
<b>Stem Cell Source, n (%)</b>	
BM	31 (56.4)
PBSC	24 (43.6)
<b>Conditioning, n (%)</b>	
MAC	30 (54.5)
MIC	3 (5.5)
RIC	22 (40.0)
<b>Serotherapy*, n (%)</b>	
Alemtuzumab	39 (70.9)
ATG	15 (27.3)
<b>Rituximab, n (%)</b>	
One dose	39 (70.9)
Four doses	16 (29.1)
<b>Rituximab dose (mg), median (range)</b>	221.25 (127.5 - 675)

### 3.3.2 Model Fitting

The two compartment turnover model was fitted to untransformed  $CD19^+$  cell counts using the Laplacian conditional estimation with interaction algorithm in NONMEM version 7.4.3, with the ADVAN13 subroutine. The initial condition of the B cell compartment was set to  $5 \times 10^6$  cells/L (half of the LLOQ) on the day of HSCT. To handle the  $CD19^+$  cell counts that were BLQ ( $n = 335$ , 54.1%), both the M5 and M3 methods were tested, with the M3 method resulting in a greater reduction in OFV. A combined additive and proportional model best described the residual error. A schematic of the K-PD model is given in Figure 3.4.

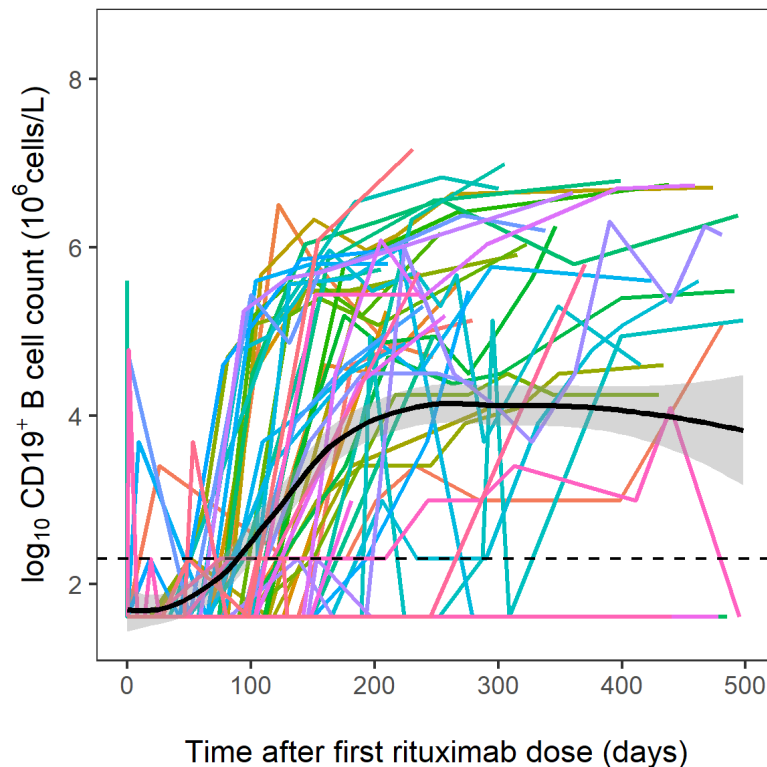


Figure 3.3: Raw data used for model-building ( $n = 55$ ). Each coloured line is an individual patient and the black dotted line represents the LLOQ of the assay used to measure  $CD19^+$  cell counts ( $10 \times 10^6$  cells/L). The thick black line is the local regression curve, and the grey shaded area is the 95% confidence interval

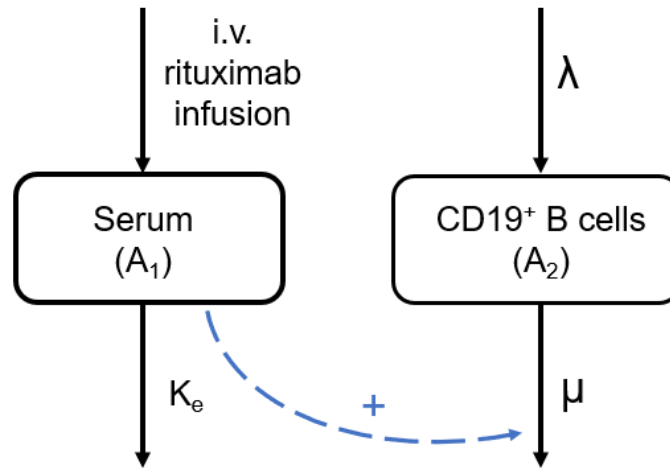


Figure 3.4: Schematic of kinetic-pharmacodynamic model of rituximab. First compartment represents the serum compartment for rituximab dosing by intravenous infusion, where rituximab decays at rate  $k_e$  and is assumed to increase CD19<sup>+</sup> cell death rate,  $\mu$ , denoted by ‘+’ sign. Second compartment represents CD19<sup>+</sup> cells produced by the bone marrow at zero-order rate  $\lambda$  and dying at first-order rate  $\mu$ . A B cell maturation function was applied to  $\lambda$  and  $\mu$  to scale for age-related effects, and a sigmoidal Hill-type function was used to account for the delay in bone marrow output after HSCT.

### 3.3.3 Parameter Estimates

The parameter values estimated from the model-building dataset have been summarised in Table 3. The setpoint parameter was derived by dividing  $\lambda$  by  $\mu$  to provide a measure of the number of CD19<sup>+</sup> cells at steady-state in the absence of rituximab. A delay of 44 days after HSCT was estimated for a child of median age 3.00 years to recover their bone marrow output to 50% of its maximum capacity with the administration of rituximab. Elimination half-lives for CD19<sup>+</sup> cells and rituximab were calculated from  $\mu$  ( $t_{1/2} = \ln 2 / \mu$ ) and  $k_e$  ( $t_{1/2} = \ln 2 / k_e$ ) as 40.8 days and 6.36 days respectively. Regarding rituximab, the model estimated an apparent  $ED_{50}$  value of 0.921 mg, an apparent  $E_{max}$  value of 84.4 and an elimination rate of 0.109 per day.

Table 3.3: Estimated parameter values. Setpoint parameter was derived by dividing  $\lambda$  by  $\mu$ .  $\lambda$ , CD19<sup>+</sup> cell production rate constant;  $\mu$ , CD19<sup>+</sup> cell death rate constant;  $\gamma$ , Steepness of slope of CD19<sup>+</sup> cell recovery;  $T_{50}$ , Time to half-maximal output of CD19<sup>+</sup> cells from bone marrow;  $k_e$ , Rituximab elimination rate constant;  $E_{max}$ , Apparent maximum killing effect of rituximab on CD19<sup>+</sup> cells;  $ED_{50}$ , Rituximab dose producing 50% of apparent maximum killing effect; RSE, relative standard error; BSV, between-subject variability; CI, confidence interval.

Parameter (Units)	Estimate (%RSE)	%BSV (%RSE)	Shrinkage (%)	Bootstrap Median (95% CI)
Setpoint (x 10 <sup>6</sup> cells/L)	79.5 (-)	-		
$\lambda$ (x 10 <sup>6</sup> cells/day)	1.40 (19.70)	126.10 (60.87)	71.7	1.37 (0.852 - 1.98)
$\mu$ (cells/day)	0.018 (22.76)	98.60 (90.84)	30.1	0.018 (0.00910 - 0.0252)
$\gamma$	3.18 (8.83)	-	-	3.40 (2.91 - 4.07)
$T_{50}$ (days)	44.8 (22.35)	96.07 (85.86)	1 x 10 <sup>-10</sup>	49.2 (31.3 - 71.8)
$k_e$ (/day)	0.109 (12.74)	-	-	0.0926 (0.0619 - 0.121)
$E_{max}$	84.4 (26.79)	-	-	78.3 (46.1 - 130.3)
$ED_{50}$ (mg)	0.921 (20.36)	-	-	0.933 (0.622 - 1.40)

### 3.3.4 Covariate Effects

The covariate model from the mechanistic NLME model of CD19<sup>+</sup> cell reconstitution post-HSCT in Chapter 2 was used, with effects of covariates linearly parameterised by multiplication of the parameter by (1 + effect size). Covariate effects are summarised in Table 3.4, and elaborated in turn below.

Table 3.4: Covariate effects identified using SCM.  $T50$ , Time to half-maximal output of  $CD19^+$  cells from bone marrow; PID, primary immunodeficiency; MAC, myeloablative conditioning; RSE, relative standard error; CI, confidence interval.

Parameter	Covariate	Effect Size (% RSE)	Bootstrap Median (95% CI)
$T50$	PID	-0.47 (25.82)	-0.469 (-0.687 to -0.130)
$T50$	MAC	0.954 (28.69)	0.954 (0.393 - 1.48)
$T50$	Matched Donor	-0.47 (197.7)	-0.449 (-0.628 to -0.228)

### *PID*

Of the 55 study patients, 18 (32.7%) had an HSCT indication of PID and were identified as having a significantly different pattern of long-term  $CD19^+$  cell reconstitution following rituximab administration compared to patients with other diagnoses. While the bone marrow of the typical patient required 44.8 days to recover to 50% of its maximum  $CD19^+$  cell production capacity, patients with PID needed 23.7 days, i.e. a decrease of 53%, to recover their bone marrow output to the same extent.

### *MAC*

The time taken to recover 50% of bone marrow output was also affected by the type of conditioning regimen. Patients who received a MAC regimen ( $n = 30$ , 54.5 %) took approximately 87.5 days to recover their bone marrow output to 50% capacity. This was nearly double the the mean estimated  $T50$  value for patients who received either RIC or MIC regimens who took 44.8 days.

### *Matched Donor*

Two-thirds of the study patients received HSCs from a HLA-matched donor ( $n = 37$ , 67.3%). These patients were found to have a statistically significant difference in the time taken to recover their bone marrow output to 50% capacity, a 53% decrease from 44.8 days to 23.7 days.

## 3.3.5 Model Evaluation

The model was evaluated using goodness-of-fit plots (Figure 3.5) and a pcVPC (Figure 3.6). Model evaluation demonstrated a good fit of the observed data to the model-predicted data, with most of the data clustering along the line of unity in the plots of the observed data against both the population predictions and individual predictions. In addition, the residual error was well described by the combined error model as shown in the plot of CWRES against time since HSCT, which



suggested a normal distribution with mean zero, with most of the data between between  $\pm 2$  standard deviations of the mean and no pattern developing with time since HSCT. For the plot of IWRES against individual predictions, there are visible perturbations to an otherwise flat line due to the BLQ data and some individuals with high individual predictions. Lastly, the pcVPC illustrated consistency between the observed data and simulated data, with the observed percentiles falling within the 95% prediction intervals. The prediction intervals are wider at later timepoints post-HSCT due to fewer data. As seen by the lower part of the pcVPC, the M3 method worked well in capturing the proportion of data that were BLQ.

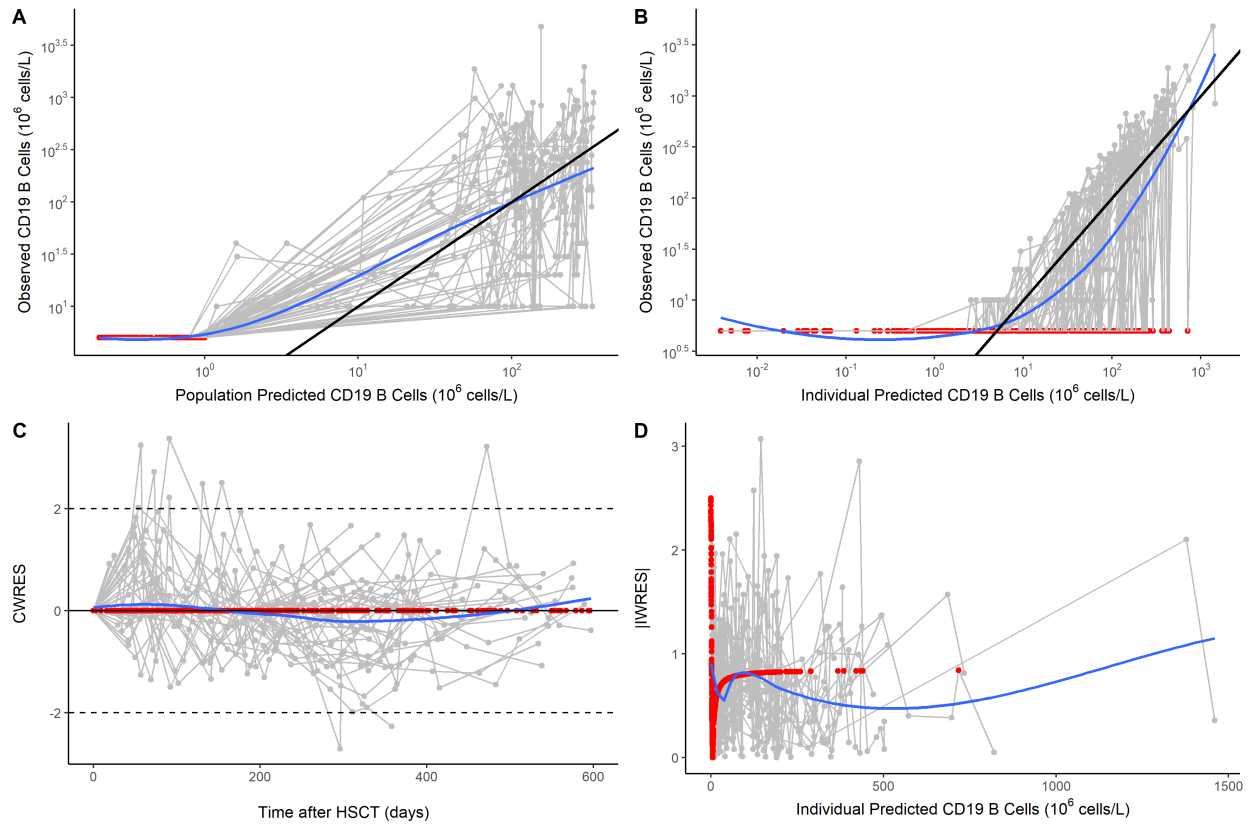


Figure 3.5: Goodness-of-fit plots. A) Observed CD19<sup>+</sup> cell counts vs Population Predicted CD19<sup>+</sup> cell counts. B) Observed CD19<sup>+</sup> cell counts vs Individual Predicted CD19<sup>+</sup> cell counts. C) CWRES vs Time. D) |IWRES| vs Individual Predicted CD19<sup>+</sup> cell counts. Black lines are lines of unity, blue lines are the local regression curves and red datapoints are those that were BLQ.

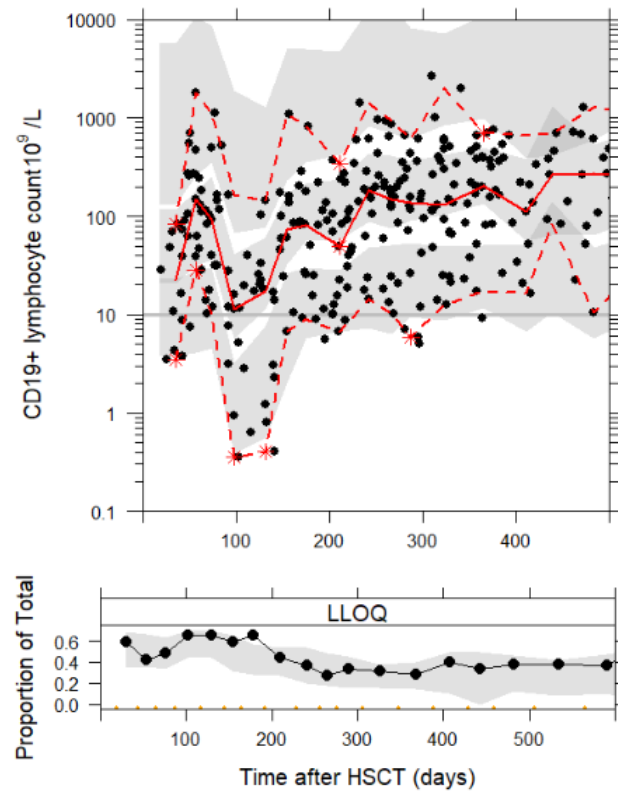


Figure 3.6: Visual predictive check of final rituximab model. Black dots are observed data and the solid red line is the observed median. The dotted red lines are the observed 2.5th, 50th and 97.5th percentiles and the grey shaded area are the 95% prediction intervals. The bottom panel shows the proportion of total data that were BLQ.

### 3.4 Discussion

In this chapter, a novel two-compartment K-PD model was constructed to quantify the pharmacodynamics of rituximab on CD19<sup>+</sup> cells in a paediatric post-HSCT cohort with EBV reactivation. Rituximab effect was incorporated into the mechanistic PD model of CD19<sup>+</sup> cell reconstitution post-HSCT of Chapter 2 therefore the rituximab model exemplifies a clinical scenario in which drug insult further perturbs the recovery of B cells post-HSCT. Regarding its clinical utility, the model has the potential to inform rituximab dosing in this cohort via model-based simulations and to predict individualised patient trajectories of CD19<sup>+</sup> cell reconstitution after rituximab administration.

As a whole, the estimated parameter values of the rituximab K-PD model were biologically valid and the values estimated for the B-cell related parameters  $\lambda$ ,  $\mu$ ,  $\gamma$  and  $T50$  could be compared to the estimated values from the CD19<sup>+</sup> cell model built for non-rituximab patients. For the CD19<sup>+</sup> cell proliferation rate,  $\lambda$ , the K-PD model estimated a value of  $1.4 \times 10^6$  cells/L (95% CI: 0.852 - 1.98), which was 22% lower than estimated in the absence of rituximab ( $1.68 \times 10^6$  cells/L; 95% CI, 1.36 - 2.05). As the drug effect of rituximab was applied to  $\mu$ , this finding was not expected and may suggest that the  $E_{max}$  model may not be fully capturing the rituximab effect. When categorised into age groups for infants, children and adolescents,  $\lambda$  estimates decreased with increasing age as follows;  $4.34 \times 10^6$  cells/L for infants,  $3.58 \times 10^6$  cells/L for children and  $2.47 \times 10^6$  cells/L for adolescents. This was expected and aligned with the established biological mechanism of increased bone marrow output at younger ages accounted for by the B cell maturation function<sup>146</sup>, even after rituximab administration. Of note, this finding contradicts Jamois *et al*, who did not observe any age-related effect in reconstituting CD19<sup>+</sup> cell counts in paediatric patients aged 6-17 years administered rituximab for MPA and GPA<sup>214</sup>. In contrast, our result was corroborated by a study in children following renal transplantation, which noted quicker repopulation of B cells after rituximab administration for children under 10 years<sup>263</sup>. However, this age-related effect did not hold when patients were stratified by the number of rituximab doses administered. The single-dose patients (median age, 3.44 years) and four-dose patients (median age, 2.46 years) had median  $\lambda$  estimates of  $4.06 \times 10^6$  cells/L and  $2.38 \times 10^6$  cells/L respectively, a 41% decrease with four doses which suggested possible dose dependency of CD19<sup>+</sup> cell proliferation on rituximab despite the four-dose patients being a year younger than the single-dose patients. Taken together, this may suggest that in addition to rituximab stimulating  $\mu$ , rituximab may also be inhibiting  $\lambda$  to some extent thereby affecting bone marrow output of new B cells.

Several studies both in adults and children support the hypothesis that a lower rituximab dose may suffice to suppress B cell levels sufficiently. For example, Delapierre *et al* observed that a lower rituximab dose than normal, 100 mg/m<sup>2</sup> compared to the standard 375 mg/m<sup>2</sup> achieved

B cell suppression lasting 6 months and control of EBV viral load in 16 adults as a pre-emptive regimen post-HSCT<sup>264</sup>. Similarly, a single rituximab dose of 375 mg/m<sup>2</sup> cleared EBV viraemia in 19 paediatric patients (median age, 5 years) in a study by Kim *et al*<sup>265</sup> and Wennmann *et al* showed one dose to be sufficient to drop EBV viral load to below the LLOQ in 25 paediatric patients<sup>266</sup>. In addition, simulations performed by Pan *et al* in a paediatric population with autoimmune disease demonstrated that a single infusion of 750 mg/m<sup>2</sup> resulted in comparable CD19<sup>+</sup> cell depletion lasting 6 months to the standard regimen of four doses of 375 mg/m<sup>2</sup><sup>2185</sup>. Furthermore, in a study in healthy volunteers, an extremely low rituximab dose of 1 mg/m<sup>2</sup> resulted in the depletion of 97% of all B cells<sup>267</sup>. To ascertain whether a lower rituximab dose may suffice to suppress B cell levels sufficiently to maintain EBV VL below the LLOQ, simulations of the time course of CD19<sup>+</sup> cells with different rituximab dosing regimens using this K-PD model are now required.

The estimated value of 0.018 cells/day (95% CI: 0.00910 - 0.0252) for  $\mu$  was comparable to the estimate of 0.015 cells/day (95% CI: 0.013 - 0.018) without rituximab, and was also equivalent between one-dose and four-dose patients. This finding is corroborated by literature values; the estimated  $\mu$  of 0.018 cells/day aligns with the CD19<sup>+</sup> cell death rate,  $k_{out}$ , of 0.02/day estimated in paediatric patients administered rituximab for rheumatological disease ( $n = 39$ )<sup>185</sup> and with the B cell turnover rate of 0.012 cells/day derived using the mean B cell disappearance rate of 2.29%/day previously reported for adults with chronic lymphocytic leukaemia ( $n = 7$ ) and the absolute CD19<sup>+</sup> cell count measured by Morbach *et al* for 26-50 year olds<sup>54,179</sup>. Therefore, while  $\lambda$  seems sensitive to rituximab in a dose-dependent manner, there appears to be relative consistency of  $\mu$  across various disease settings, including in the present study of rituximab, as well as across species as detailed in the Discussion of Chapter 2. Taken together, this suggests that the mechanisms of B cell turnover may remain robust despite B-cell disease or administration of B cell-depleting therapy. This may suggest that the  $E_{max}$  model is not appropriately capturing the totality of the rituximab effect on  $\mu$ .

Some previous rituximab models have either estimated the baseline CD19<sup>+</sup> cell count as a parameter<sup>185</sup> or investigated it as a covariate on PK parameters<sup>231,257</sup>, while studies in the context of B cell lymphomas have related rituximab effect to tumour burden and baseline CD19<sup>+</sup> cell count<sup>268,269</sup>. To capture baseline CD19<sup>+</sup> cell count, the model-estimated parameter mean values for  $\lambda$  and  $\mu$  were divided to derive a setpoint parameter representing the number of CD19<sup>+</sup> cells at steady-state in the absence of rituximab, which can be interpreted as the baseline CD19<sup>+</sup> cell count. Rituximab patients had 29% fewer CD19<sup>+</sup> cells at baseline prior to rituximab administration ( $79.5 \times 10^6$  cells/L) as opposed to non-rituximab patients ( $112 \times 10^6$  cells/L), and the setpoint was comparable when stratified by the number of doses. It could be speculated that processes occurring during EBV transformation of B cells may impact the level of CD19<sup>+</sup>/CD20<sup>+</sup> expression on B cells resulting in fewer B cells with detectable CD20<sup>+</sup> and thereby a reduced number of target

CD20<sup>+</sup> antigen in rituximab patients infected with EBV, hence a lower baseline CD19<sup>+</sup> cell count, than in the rituximab-naive post-HSCT patients. There is some clinical evidence to support this such as Starr *et al*, who noted that a decrease in CD20<sup>+</sup> expression has been observed in some B cell lymphomas<sup>270</sup>, Hiraga *et al*, who saw downregulation of CD20<sup>+</sup> expression in 30% of adult patients with B cell lymphoma<sup>271</sup> and several others<sup>272-275</sup>. Although the majority of these cases were in the context of lymphoma, such findings suggest that EBV-related epigenetic modifications may affect expression of B cell markers<sup>276</sup>, which in turn, may impact baseline CD19<sup>+</sup> cell count in patients receiving rituximab for EBV reactivation post-HSCT. In particular, Mrozek-Gorska *et al* demonstrated experimentally that EBV locks human naive B cells in a stage of differentiation resembling plasma cells, which usually do not express CD20<sup>+</sup><sup>277</sup>. Another explanation for the lower baseline CD19<sup>+</sup> cell count observed in rituximab patients could be resistance to rituximab, which has long been documented in the literature<sup>245,278,279</sup> or changes in levels of target CD20<sup>+</sup> expression with time<sup>240</sup>. However, a parallel line of evidence in the literature suggests that EBV reactivation post-HSCT occurs in memory B cells due to disruption of the germinal centre post-HSCT<sup>280</sup>, which is corroborated by Leandro *et al* who observed cells of a memory B cell phenotype that were not depleted by rituximab<sup>249</sup>. Therefore, the exact mechanisms underlying the lower baseline CD19<sup>+</sup> cell count at steady-state in patients prior to rituximab administration remain to be elucidated.

The model-estimated value for the rituximab elimination rate constant,  $k_e$ , of 0.109 per day (95% CI: 0.0619 - 0.121) aligned well with a previous model estimate of 0.143 per day (95% CI: 0.0478 - 0.418) in adults with no disease progression of B cell lymphoma<sup>256</sup>. From  $k_e$ , an elimination half-life of 6.36 days was calculated, which was consistent with the half-life of 4.85 days observed by Rozman *et al* in adult patients with no disease progression<sup>256</sup> and with early studies in adult lymphoma patients that reported 5.3-20 days after subsequent infusions<sup>281</sup>, 3-33 days<sup>282</sup> and mean terminal half-lives of 3.2 days and 8.6 days after the first and fourth rituximab infusions<sup>268</sup>. However, in general, the estimated apparent half-life of 6.36 days was also considerably lower than other estimated half-lives in the literature, which fell within the range of 17-29 days<sup>185,231,240,253,283,284</sup>. The lower half-life could suggest that saturation of the CD20-mediated pathway was not achieved resulting in higher clearance of rituximab and lower exposure in patients with EBV reactivation. As IIV on  $k_e$  has not yet been tested, the relationship between rituximab dose and half-life could not be distinguished. As for other monoclonal antibodies, some variability in rituximab elimination is expected and several PK models have parameterised clearance to reflect this, including a non-specific time-independent clearance term to represent catabolic clearance, and hence linear aspects of rituximab PK, and a specific time-dependent clearance to account for TMDD, i.e., non-linear PK<sup>240,256,258</sup>.

Another consideration in interpreting the rituximab parameters are confounding factors in the anal-

ysis of the exposure-response relationship such as baseline target expression of CD20<sup>+</sup>, biology of EBV reactivation post-HSCT, progression of EBV infection and resistance to rituximab. Differences in PD of rituximab between adults and paediatric patients could be due to differences in the concentration, expression and availability of the target CD20<sup>+</sup> or binding affinity, resulting from differences in disease activity or maturation processes<sup>285</sup>.

In general, the lack of published PD models of rituximab limited our ability to contextualise the estimates of the PD parameters,  $ED_{50}$  and  $E_{max}$ , with the exception of two studies, Pan *et al* and Schoergenhofer *et al*<sup>185,267</sup>. The model estimated apparent  $E_{max}$  value of 84.4 (95% CI: 46.1-130.3) is relatively high in patients with EBV reactivation post-HSCT compared to the estimate of 35.2 in Pan *et al* in paediatric autoimmune patients, which may be related to the difference in disease between the two patient cohorts and the younger median age of the HSCT patients (present model, 3.00 years; Pan *et al*, 13.2 years). In contrast, the model-estimated apparent  $ED_{50}$  value of 0.921 mg was comparable to the 0.81 mg estimated by Pan *et al*. Schoergenhofer *et al* reported a much lower  $ED_{50}$  value of 0.1 mg/m<sup>2</sup> measured in healthy volunteers after a single infusion<sup>267</sup>. The clinical utility of  $E_{max}$  and  $ED_{50}$  would be demonstrated when model-based simulations are performed to inform optimal dosing regimens of rituximab.

The slope of B cell recovery was captured by the Hill-coefficient,  $\gamma$ , which decreased from 4.17 to 3.18 in the presence of rituximab, consistent with the delayed rate of CD19<sup>+</sup> cell reconstitution after rituximab. Similarly, long-term reconstitution of CD19<sup>+</sup> cells, parameterised by  $T50$ , was estimated to be 14 days quicker in rituximab patients (44.8 days; 95% CI: 31.3 - 71.8 days) than in non-rituximab patients (58.9 days; 95% CI: 44.0 - 64.0 days). Ontogenic B cell reconstitution occurs after rituximab administration driven by naive B cells in the bone marrow, the same process that follows HSCT<sup>118,249</sup>, which results in a large proportion of transitional B cells dominating the B cell compartment early after HSCT. This has been observed in several studies including Stocker *et al*, who observed more transitional B cells in post-HSCT paediatric patients who received rituximab than those who did not receive rituximab<sup>223</sup>, a case report by Defilipp *et al*, who documented an increase in transitional B cells in a 19 year-old post-HSCT patient who received rituximab for GVHD<sup>286</sup> and Sarantapoulos *et al*, who observed a greater total number and frequency of naive and transitional B cells in adult post-HSCT patients with chronic GvHD<sup>287</sup>. Collectively, the presence of increased transitional B cells following rituximab in these findings indicate that these cells have differentiated from HSCs in the bone marrow, suggesting the possibility of faster recovery of bone marrow output after rituximab administration post-HSCT. Therefore, the  $T50$  parameter seemed to better reflect the regenerative capacity of the bone marrow than  $\lambda$ .

In general, the effect sizes of the covariates estimated for the rituximab K-PD model were markedly greater than for the model of CD19<sup>+</sup> cell reconstitution post-HSCT in Chapter 2, suggesting the exacerbation of CD19<sup>+</sup> cell reconstitution post-HSCT in the presence of rituximab. In addition, this

demonstrates the ability of the covariate model to capture the impact of drug insult via rituximab, highlighting their clinical relevance. The PID sub-group of patients was estimated to take 23.7 days to recover 50% of their maximum bone marrow output compared to patients with other diagnoses who took 44.8 days. This difference could not be explained by age-related differences in bone marrow output, as the median ages of the PID and non-PID patients were comparable, but may in part be explained by the majority of PID patients ( $n = 15$ , 83%) also having received alemtuzumab as part of pre-HSCT conditioning. Whilst ATG administered as pre-HSCT conditioning is a recognised risk factor for EBV reactivation post-HSCT due to its selective depletion of T cells, the broader lymphodepletive effect of alemtuzumab on both T and B cells could result in the inadvertent killing of EBV-infected B cells, as well as uninfected B cells<sup>98,207,218,288</sup>. Therefore, EBV viral load would decrease as well as the number of B cells available for EBV transformation, which may aid faster recovery of bone marrow output.

In contrast to the negligible increase of 0.5 days in the  $T_{50}$  estimate for non-rituximab patients with a matched donor, the effect of having a matched donor was more pronounced in rituximab patients, decreasing  $T_{50}$  by 53% from 44.8 days to 23.7 days. Several studies corroborate this such as Jain *et al*, who observed a higher percentage of patients with unmatched HSCTs (16%) with EBV reactivation compared to patients with matched HSCTs (9%)<sup>222</sup>. Similarly, Salas *et al* reported increased incidence of EBV reactivation in patients with mismatched or matched unrelated HSCT donors<sup>289</sup>. Therefore, the finding that patients with matched donors had better prognosis is expected, as patients with HLA-mismatched donors have long been known to be at higher risk of EBV reactivation<sup>205–207</sup> and experience delayed immune reconstitution<sup>290,291</sup>.

While a PID diagnosis and having a matched donor decreased  $T_{50}$ , patients who received a MAC regimen ( $n = 30$ , 54.5 %) were estimated to recover half-maximal bone marrow output at 87.5 days post-HSCT, nearly double the 44.8 days taken for patients with RIC or MIC regimens. For non-rituximab patients, an increase in  $T_{50}$  of 10 days from 58 days to 68 days was observed for MAC patients, highlighting the greater covariate effect of MAC in the presence of rituximab. This finding is in line with previous reports of conditioning regimens featuring total body irradiation to be risk factors for EBV reactivation and PTL<sup>292,293</sup>. A possible reason for this observation could be the higher degree of bone marrow toxicity conferred by MAC compared to RIC or MIC, which may delay the restoration of bone marrow output post-HSCT and thereby B cell reconstitution.

Building on work by Pan *et al*, who developed the first paediatric PD model for rituximab<sup>185</sup>, the K-PD model developed in this chapter quantified the effect of rituximab in a post-HSCT paediatric population with EBV reactivation. Despite the relatively small sample size of 55 patients, strengths of the present K-PD model include the incorporation of the previously developed B cell maturation function to account for age-related effects, and its ability to detect covariate effects that aligned with biological mechanisms. Nonetheless, there were also several limitations to this work. Due

to the nature of the retrospective data used, rituximab PK was not fully captured in the model. It could be possible that age effects on rituximab PK may contribute to differences seen in PD between an adult and paediatric population. To address this, published rituximab PK data could be considered from the literature. A useful exercise would be to scale a published adult rituximab PK model using allometry to see if it predicts published paediatric rituximab PK parameters. Efforts of future work will focus on the above. Following refinement of the model, performing simulations of varying dose regimens as tested before in paediatric patients<sup>185</sup> would allow identification of the optimal rituximab dose required to clear EBV viraemia in this post-HSCT cohort with EBV reactivation, the prognostic value of which has been noted in previous studies<sup>222</sup>. Furthermore, the need to individualise rituximab dosing has been suggested for a range of B cell lymphoproliferative disorders<sup>294</sup>, where high PK IIV was observed. Going forward, this model may also have potential to inform dosing of rituximab biosimilars, which are now routinely administered following expiry of rituximab's patents.



## Chapter 4

# Dynamics of EBV Reactivation After HSCT

### 4.1 Introduction

#### 4.1.1 Viral Dynamic Models

Since the 1990's, mathematical modelling has been used to describe lytic viral replication *in vivo* in order to quantify underlying within-host and immune mechanisms as well as the effect of anti-viral treatment<sup>87,103</sup>. The first viral dynamic model was developed to better understand HIV infection in relation to its host cells, CD4<sup>+</sup> cells<sup>295</sup>, centred on three populations; free virus particles, that drive infection of uninfected host cells, which produce infected host cells, which in turn burst to produce more free virus thereby propagating infection. Still regarded today as the original viral dynamic model, there have been since been several iterations of the model over the years to further study HIV<sup>296,297</sup>, and it has also formed the basis of models for other viruses such as human T cell leukaemia virus (HTLV-1)<sup>298</sup>, hepatitis C (HCV)<sup>299,300</sup> and cytomegalovirus (CMV)<sup>301</sup>. More recently, viral dynamic models have been employed to characterise aspects of severe acute respiratory syndrome-coronavirus 2 (SARS-CoV-2) infection in response to the ongoing pandemic<sup>302,303</sup>. In general, viral dynamic models vary in their level of complexity, ranging from the simple target cell-limited model<sup>304</sup> to more intricate mechanistic models<sup>305</sup>. Models that integrate PK and PD with viral kinetics (VK) and viral dynamics (VD), so-called PK-VK models for example, have proven instrumental in studying the effects of anti-viral therapy for infectious diseases<sup>306–308</sup>.

### 4.1.2 EBV Dynamic Models

To the best of the author's knowledge, there are currently no published viral dynamic models for EBV reactivation post-HSCT. Nevertheless, mathematical models have previously been developed to study EBV biology and viral dynamics of EBV infection in other settings therefore these were reviewed for their relevance and potential application to our data.

The earliest mathematical models used agent-based modelling and simulation to investigate within-host dynamics of EBV infection<sup>309,310</sup>. Agent-based models focus on biological entities of interest, agents, and their interactions within a virtual anatomical space according to a rule-based framework<sup>311</sup>. When compared to ODE-based models, the rules governing agent-based models can be likened to the assumptions of an ODE model, while the virtual environment is similar to the compartments that represent an abstract region of tissues or cells in an ODE model.

PathSim, an agent-based model and simulation tool developed by Duca *et al*, comprised a virtual site of EBV infection and persistence, the tonsils and adenoids, where the agents, cells or free virus, could interact<sup>309</sup>. Two key findings from the simulations were the identification of a switch in the course of EBV infection from persistence to clearance upon reactivation of latently infected B cells, and the necessity of the peripheral memory B cell compartment for persistence. In addition, simulation output broadly resembled the dynamics observed in *in vivo* data from patients with glandular fever including distinct acute and persistent phases of infection and exponential decay of infected B cells. However, the model was not itself fitted to *in vivo* data from immunocompromised hosts therefore its ability to describe observed clinical data in the context of EBV reactivation remains unclear. In addition, the model had 33 biological parameters, most of which were fixed to values based on previous literature, suggesting that the model parameters might not be identifiable. Furthermore, the peripheral blood was not represented in the virtual environment, which was the site of blood sampling used to measure EBV VL in the post-HSCT patient cohort. Shapiro *et al* extended the findings of Duca *et al* by performing additional PathSim simulations to investigate key parameters, identifying the reactivation rate of latently infected B cells into lytically infected B cells as the most sensitive parameter<sup>310</sup>. Another observation was the occurrence of viral clearance in the event of a small viral burst size. Two authors from these studies went on to detail the mathematical rationale of a differential equation model, the cyclic pathogen model, constructed in line with the multiple life cycle stages of EBV regulated by the host immune response<sup>312</sup>. This model was later used to illustrate that the cyclic behaviour of EBV as it exploits B cell biology is sufficient to induce persistent infection<sup>313</sup>.

Another class of rule-based models that have been explored for EBV are discrete computer models and simulations known as cellular automata, exemplified by Castiglione *et al*<sup>314</sup>. Similar to PathSim, the authors built a tool, C-ImmSim, to simulate the host immune response to EBV infection,

introducing a blood compartment. Some important results were the similarity of the simulated peak number of B cells with the peak B cell number observed in patients with glandular fever (approximately 35 days post infection), the difference in EBV kinetics between persistent infection (characterised by periodic reactivations, low VL and viral spikes) and acute infection (which featured high VL and a more “clean” profile), and that the latently infected B cells escaped immune surveillance by CTLs by residing in the blood compartment to establish persistence. Again, the model was neither fitted to nor used to predict clinical data.

Some of the drawbacks of these earlier models have since been addressed by ODE models for EBV. Huynh and Adler proposed a 10-ODE model of within-host dynamics of EBV infection of both B cells and epithelial cells, including the host immune response from CTLs<sup>315</sup>. Upon performing simulations using many of the PathSim parameters reported in Shapiro *et al*, they identified similar dynamics for B cells and EBV as seen previously, in addition to a higher number of CTLs specific for latently infected B cells than for lytically infected B cells after infection. The authors extended this model by introducing additional parameters for the host immune response, namely antibodies and cross-reactive CTLs, and suggested the importance of the number and efficiency of CTLs in the clinical outcome of glandular fever<sup>316</sup>.

A study by Huynh and Rong described a 3-ODE model for the dynamics of viral shedding into saliva developed from data from three EBV seropositive adults reported by Hadinoto *et al*<sup>317,318</sup>. Stochastic simulation was performed after introducing random variation to the number of epithelial cells susceptible to EBV originating from B cells or from epithelial cells respectively, as well as the probability of CTLs encountering and killing infected cells. Albeit with few patients, this was the first study to fit a model to clinical EBV data, with resulting parameter values estimated with good precision. A limitation preventing its application to our data are its structure designed more to capture the dynamics of the natural history of EBV infection rather than reactivation in a post-HSCT cohort receiving anti-viral therapy. In addition, VL from EBV shedding measured from saliva samples may differ to VL measured from peripheral blood samples, and the site of infection in the tonsils in relation to epithelial cells is inherently different to reactivation in the peripheral blood with respect to B cells.

Another study of interest was that of Byrne *et al*, who recently developed a mechanistic model of EBV shedding dynamics from saliva samples from 85 Ugandan adults with and without HIV-1 co-infection<sup>319</sup>. Informed by sensitivity analysis, six parameters were fixed and two parameters were fitted, the rate of B cell reactivation resulting in new lytic epithelial infection and the rate of CTL proliferation dependent on number of infected epithelial cells. Regarding covariates, graphical evaluation illustrated a negative correlation of CD4<sup>+</sup> T cell counts with EBV VL and a positive correlation of HIV-1 RNA loads with EBV VL in individuals co-infected with HIV-1, while levels of the B cell activation factor BAFF were not correlated with EBV VL. Whilst this was a com-

prehensive study, it shares the same limitations as described above for Huynh and Rong’s model, precluding its application to our dataset.

To date, the only model available for EBV reactivation post-HSCT is that reported in the doctoral thesis of Akinwumi<sup>320</sup>. A 9-ODE 25 parameter model was developed based on EBV biology, and treatment parameters were integrated to model effects of immunosuppressive drugs commonly administered pre- and post-HSCT including tacrolimus and rabbit ATG, as well as the anti-viral drug valganciclovir. Simulations demonstrated that ATG increased peak infected memory B cells, peak free EBV, setpoint of infected memory B cells as well as the time taken to reach these three points. In contrast, valganciclovir decreased both the peak infected memory B cells and peak free EBV. Despite being a complex model and not having been fitted to clinical data, the model has relevance in that it was developed for the post-HSCT setting and considers the drug effect of agents administered to patients in our study cohort.

In the absence of established *in vivo* animal models of EBV, the models and simulations described above have advanced quantitative understanding of EBV dynamics. However, they do possess limitations affecting their usefulness. These include their overparameterised nature, main focus on glandular fever as the manifestation of EBV and largely not accounting for the effects of anti-viral therapy. In addition, none of the previous studies were conducted in children, necessitating the use of age and size scaling given our paediatric study cohort. Furthermore, most previous models have been developed with immunocompetent hosts in mind whereas the study patients are immunocompromised post-HSCT. Finally, with the exception of Byrne *et al* and Huynh and Rong, the majority of previous EBV models were not fitted to or validated using clinical data to estimate parameters related to EBV kinetics and dynamics<sup>318,319</sup>.

### 4.1.3 Aims

This project aimed to develop a mechanistic NLME model to quantify EBV reactivation dynamics post-HSCT in children.

### 4.1.4 Objectives

- Clean patient electronic data of retrospective EBV VL measurements and other covariates
- Identify factors associated with EBV reactivation
- Review previously published models of EBV dynamics for their suitability to fit EBV VL measurements from study cohort
- If found unsuitable, construct NLME model of EBV reactivation dynamics post-HSCT

- Evaluate model by performing diagnostic checks to compare model-predicted and observed data

## 4.2 Methods

### 4.2.1 Data

Retrospective electronic data from routine clinical practice were collected from children who underwent HSCT at the Bone Marrow Transplant Unit at GOSH between 2005 and 2016, and had EBV reactivation post-HSCT. Patients were identified as shown in the flow diagram below (Figure 4.1).

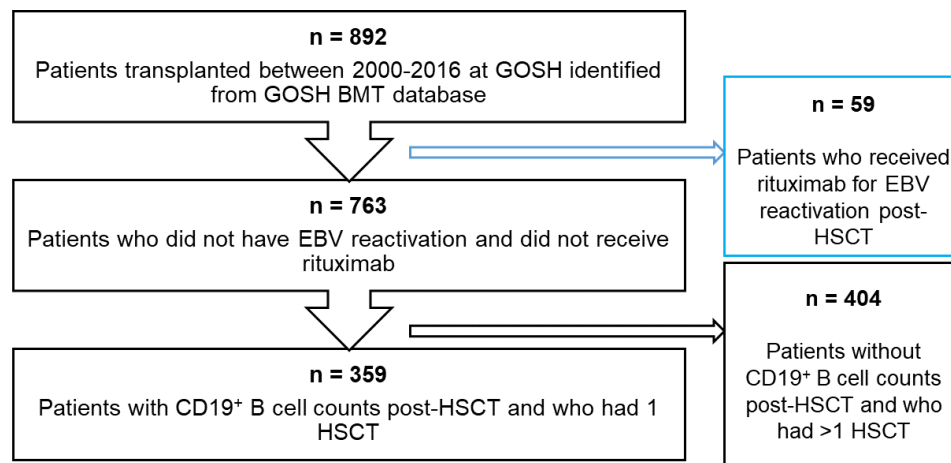


Figure 4.1: Flow diagram of study patients. Box in blue represents patients in current study ( $n = 59$ ). GOSH, Great Ormond Street Hospital; BMT, Bone Marrow Transplant; EBV, Epstein-Barr virus; HSCT, Haematopoietic stem cell transplant.

The final dataset for development of a Cox proportional hazards (Cox-PH) model comprised data from 56 patients, on account of the following inclusion criteria - that patients had:

- Not received rituximab pre-HSCT
- Not received rituximab for indications other than for EBV reactivation
- Undergone their first HSCT

- Measurements of EBV VL collected post-HSCT

Of those 56 patients, the model-building dataset for the viral dynamic model comprised only those patients who had EBV reactivation in the first 100 days post-HSCT.

Data comprised longitudinal measurements of EBV VL (copies/mL whole blood), immune cell subsets including CD19<sup>+</sup> cells and CD4<sup>+</sup> cells, demographic variables, and transplant variables. Regarding sensitivity of the assay to detect lymphocytes, 10,000 events were targeted in the lymphocyte gate. Details of monitoring for EBV viraemia and treatment for EBV reactivation are given below.

### 4.2.2 EBV Viraemia and Rituximab Therapy

In line with GOSH guidelines, EBV VL was monitored weekly by qPCR, using whole blood samples, from the start of conditioning until the CD4<sup>+</sup> T cell count exceeded 300 cells per  $\mu L$  of blood. If EBV DNA was detected via a positive qPCR result in the first three months post-HSCT, qPCR was carried out twice weekly to quantify VL until treatment was given or VL declined. The lower and upper limits of quantification of the assay for EBV VL measurements were 200 and 20,000,000 copies/mL respectively. The EBV VL threshold to treat with rituximab was 40,000 copies/mL in whole blood on two consecutive occasions within the first three months of HSCT, with the following additional criteria; having a donor different from matched sibling donor (MSD) and a CD3<sup>+</sup> T cell count < 300 cells per  $\mu L$  of blood. Rituximab was administered via intravenous infusion at a dose of 375 mg/m<sup>2</sup> weekly, with patients receiving a single dose on a conservative regimen or four doses on a pre-emptive regimen. Patients administered a single rituximab dose underwent HSCT during the years 2011-2016 whereas patients who received four rituximab doses were from a historical cohort transplanted in the period 2005-2009 treated using a pre-emptive strategy, originally studied by Worth *et al*<sup>38</sup>.

### 4.2.3 Cox Proportional Hazards Model

Many covariates contribute to the risk that a patient will experience an EBV reactivation event post-HSCT, related to the patient, donor, transplant, and drug administrations. In order to identify and quantify the impact of these covariates on EBV reactivation in the study cohort, a Cox proportional hazards (Cox-PH) model was developed using R version 4.2.0 (*survminer* (version 0.4.9), *survival* (version 3.3-1) packages) to assess the time to the first EBV reactivation event in the first 100 days post-HSCT<sup>173</sup>.

Previous studies have reported early reconstitution of immune cell subsets to be a predictor of improved outcomes post-HSCT, including less severe viral reactivation, increased overall survival and decreased non-relapse mortality<sup>49,66,321,322</sup>. To determine if such a relationship was present in our data, the threshold of early immune reconstitution defined in these studies,  $\geq 50 \times 10^6$  CD4<sup>+</sup> cells/L in two consecutive measurements within 100 days post-HSCT, was utilised to stratify patients. In addition, this definition was also applied to the measurements of ALC, CD3<sup>+</sup> cells, CD8<sup>+</sup> cells and CD19<sup>+</sup> cells to assess if this threshold could be meaningfully extended to other immune cell subsets. As an alternative method of evaluating the extent of immune reconstitution, the trapezoidal rule was used to calculate the cumulative area under the cell-time curve (AUC) from the day of HSCT (day 0) to the end of the study period (100 days) for ALC, CD3<sup>+</sup> cells, CD8<sup>+</sup> cells and CD19<sup>+</sup> cells for all patients. To illustrate this, an example of the calculation of AUC<sub>0-100</sub> CD19 for a patient can be seen in Figure 4.2.

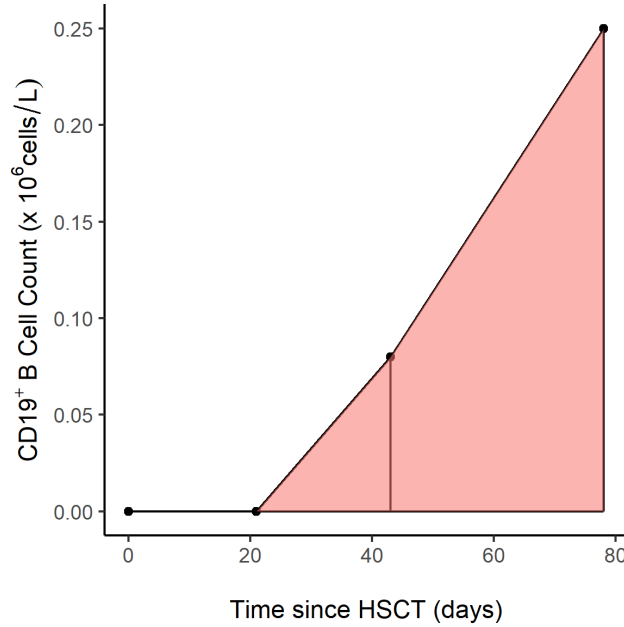


Figure 4.2: AUC<sub>0-100</sub> for CD19<sup>+</sup> cells for one patient. Black dots represent measurements of CD19<sup>+</sup> cells at 21, 43 and 78 days post-HSCT. Zero CD19<sup>+</sup> cells were assumed to be present at day 0 (day of HSCT). Pink shaded region is the AUC calculated using the trapezoidal rule.

Given that multiple ways of accounting for similar variables could result in correlation between covariates, the collinearity between covariates was evaluated prior to building the Cox-PH model. This revealed collinearity for the covariate pairs outlined in Table 4.1.

Table 4.1: Collinearity diagnostics for covariates during Cox-PH model building. ATG, anti-thymocyte globulin; AUC, area under the curve; ALC, absolute lymphocyte count; IR, immune reconstitution, RTX, rituximab. Early IR of all immune cell subsets was calculated using previously defined threshold of early immune reconstitution,  $\geq 50 \times 10^6$  cells/L<sup>66</sup>.

Covariate Pair	Correlation Co-efficient
ATG, Alemtuzumab	0.96
AUC <sub>0-100</sub> CD8, AUC <sub>0-100</sub> CD3	0.90
early CD8 IR, early, CD3 IR	0.72
AUC <sub>0-100</sub> CD4, AUC <sub>0-100</sub> CD3	0.59
AUC <sub>0-100</sub> CD4, AUC <sub>0-100</sub> ALC	0.58
early CD4 IR, early CD3 IR	0.57
AUC <sub>0-100</sub> CD3, AUC <sub>0-100</sub> ALC	0.52
early ALC IR, early CD4 IR	0.49
early ALC IR, early CD3 IR	0.49
early CD8 IR, early CD4 IR	0.48
RTX doses, early CD4 IR	0.45

The highest correlation was observed between ATG and alemtuzumab, while the remainder were mainly between T cell-related covariates. As a result, CD3<sup>+</sup> cell counts were dropped given that T cells were accounted for in the CD4<sup>+</sup> cell and CD8<sup>+</sup> cell variables, ATG and alemtuzumab were collapsed into a dichotomous serotherapy covariate, and the AUC<sub>0-100</sub> for the various immune cell subsets were chosen given that we were not confident in the validity of extending the threshold of early immune reconstitution to immune cell subsets other than CD4<sup>+</sup> cells.

Therefore, the final covariates included in the model were the following; type of donor, HSC source, whether the patient had an HSCT indication of PID, EBV serostatus of both donor and recipient, type of conditioning regimen, administration of alemtuzumab or ATG as serotherapy pre-HSCT, age, number of rituximab doses, and AUC<sub>0-100</sub> for ALC, CD19<sup>+</sup> cells, CD4<sup>+</sup> cells and CD8<sup>+</sup> cells. Variables significant in univariate analysis ( $p < 0.05$ ) were taken forward to a multivariable analysis. All categorical covariates were dichotomous, and the biological rationale for the reference classification and other classification were determined in conjunction with the GOSH BMT clinical team.



### 4.2.4 Sensitivity Analysis

In the Introduction to this chapter in section 4.1, a literature review was performed to assess the suitability of existing EBV models to fit patients' EBV reactivation VL measurements. The mechanistic model of EBV viral kinetics by Akinwumi was considered to be the most relevant starting point of all the previous reported EBV models, as it was developed for the post-HSCT setting<sup>320</sup>. The model describes the key stages of the EBV infection cycle based on the germinal centre theory of EBV biology, and is visualised schematically in Figure 4.3.

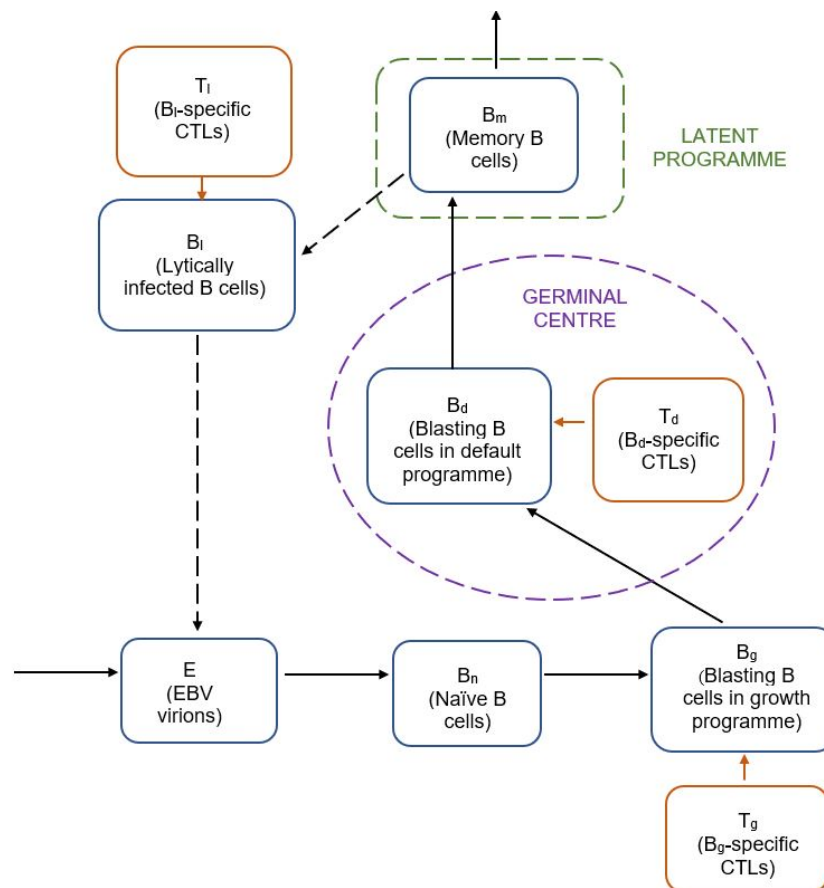


Figure 4.3: Schematic of Akinwumi model of EBV kinetics<sup>320</sup>. Blue boxes are B cell compartments, orange boxes are CTL compartments. CTL, cytotoxic T cell.

It is comprised of nine variables related to the processes of latent and lytic EBV infection, as well as the various types of B cell and CTL involved in the host immune response, totalling 25 parameters to be estimated or fixed. Free EBV virions,  $E$ , infect naïve B cells,  $B_n$ , of which a fraction transforms

into infected B cells,  $B_g$ , expressing the growth programme. The remainder proliferate into infected B cells that undergo the default programme in the germinal centre,  $B_d$ . Some of the default B cells become latently infected memory B cells,  $B_m$ , which can reactivate to become lytically infected B cells,  $B_l$ . CTLs specific to the  $B_g$ ,  $B_d$  and  $B_l$  infected B cell populations are included by way of the  $T_g$ ,  $T_d$  and  $T_l$  populations respectively. The model equations are given below:

$$\frac{dE}{dt} = n\delta_l B_l - \delta_E E, \quad (4.1)$$

$$\frac{dB_n}{dt} = \lambda_n - \mu_e E B_n - \delta_n B_n, \quad (4.2)$$

$$\frac{dB_g}{dt} = (1 - \beta)\mu_e E B_n + (r_g - \omega_g - \delta_g)B_g - \delta_1 T_g B_g, \quad (4.3)$$

$$\frac{dB_d}{dt} = \omega_g B_g + (r_d - \delta_d - \omega_d)B_d - \delta_2 T_d B_d, \quad (4.4)$$

$$\frac{dB_m}{dt} = \omega_d B_d + (r_m - \delta_m - \omega_m)B_m, \quad (4.5)$$

$$\frac{dB_l}{dt} = \omega_d B_d + (r_m - \delta_m - \omega_m)B_m, \quad (4.6)$$

$$\frac{dT_g}{dt} = r_1 T_g B_g - d_1 T_g, \quad (4.7)$$

$$\frac{dT_d}{dt} = r_2 T_d B_d - d_2 T_d, \quad (4.8)$$

$$\frac{dT_l}{dt} = r_3 T_l B_l - d_3 T_l. \quad (4.9)$$

The model was implemented in R version 4.2.0 using the *deSolve* (version 1.28) package<sup>173</sup>, with all 25 parameters fixed to published values to obtain a reference fit of the model (Table 4.2). The latently infected memory B cell compartment,  $B_m$ , was taken as a proxy for EBV VL. The VL sensitivity to each of the 25 parameters was determined by setting each in turn through a range of values (0.00001-1000) to simulate the EBV VL trajectory. The root mean squared distance (RMSD) was calculated for each parameter for the range of parameter values tested to provide a comparison between the reference fit and each of the simulated fits.

Table 4.2: Parameter values used to obtain reference fit of Akinwumi model. <sup>a</sup> Assumption; parameters are measured per week except for  $n$  and  $\beta$  that are dimensionless.

Parameter	Description	Value	Reference
$n$	Viral burst size	$1.00 \times 10^5$	310,315

Parameter	Description	Value	Reference
$\delta_l$	Death rate of lytically infected cell due to viral burst	$2.32 \times 10^{-4}$	310,315
$\delta_e$	Death rate of EBV	2.33	310
$\lambda_n$	Production rate of naive B cells	$5.04 \times 10^5$	310,315
$\beta$	NK cell effect on EBV infection	0.80	<i>a</i>
$\mu_e$	EBV infection rate per B cell virus	$3.30 \times 10^{-8}$	315
$\delta_n$	Death rate of naive B cells	1.68	315
$r_g$	Proliferation rate of infected B cells expressing growth programme	37.8	310,315
$\omega_g$	Transit rate from growth compartment to default compartment	4.90	315
$\delta_g$	Death rate of infected B cells expressing growth programme	0.88	310,315
$\delta_1$	CTL killing rate of infected B cells expressing growth programme	$3.83 \times 10^{-4}$	315
$r_d$	Proliferation rate of infected B cells expressing default programme	38.81	323
$\omega_d$	Transit rate from default compartment to memory compartment	10.08	315,323
$\delta_d$	Death rate of infected germinal B cells expressing the default programme	10.08	315,323
$\delta_2$	CTL killing rate of infected B cells expressing default programme	$3.83 \times 10^{-4}$	315
$r_m$	Proliferation rate of infected memory B cells	0.00	310,315
$\omega_m$	Reactivation rate of infected memory B cells into lytically infected B cells	0.84	310,315
$\delta_m$	Death rate of infected memory B cells	0.00	310,315,323
$\delta_3$	CTL killing rate of lytically infected B cells	$7.66 \times 10^{-4}$	310,315
$r_1$	CTL activation rate against infected B cells expressing the growth programme	$1.40 \times 10^{-3}$	310,315
$r_2$	CTL activation rate against infected B cells expressing the default programme	$2.10 \times 10^{-3}$	310,313,315

Parameter	Description	Value	Reference
$r_3$	CTL activation rate against lytically infected B cells	$4.90 \times 10^{-3}$	310,315
$d_1$	CTL death rate responding to growth compartment	$6.46 \times 10^{-2}$	310,313
$d_2$	CTL death rate responding to default compartment	$6.46 \times 10^{-2}$	310,313
$d_3$	CTL death rate responding to lytic compartment	$6.46 \times 10^{-2}$	310,313

#### 4.2.5 Viral Dynamic Model Building

In the event that a simplified version of the Akinwumi model could not be fitted to the patient EBV VL data, a viral dynamic model of EBV reactivation dynamics post-HSCT was constructed using a NLME approach. The K-PD model developed in Chapter 3 for rituximab PD on CD19<sup>+</sup> cells was leveraged by combining it with a viral dynamic model reported by Wang *et al*<sup>324</sup>. The authors extended the classical viral dynamic model to include a CTL compartment to incorporate drug effects of antiretroviral therapy for HIV infection of CD4<sup>+</sup> cells. The equations for the 4 ODE model of Wang *et al* were as follows;

$$\frac{dT}{dt} = \lambda - dT - kVT, \quad (4.10)$$

$$\frac{dT^*}{dt} = kVT - \delta T^* - qT^*C, \quad (4.11)$$

$$\frac{dV}{dt} = N\delta T^* - cV, \quad (4.12)$$

$$\frac{dC}{dt} = pT^*C - d_c C, \quad (4.13)$$

where  $T$ ,  $T^*$ ,  $V$  and  $C$  represent the uninfected CD4<sup>+</sup> cells, infected CD4<sup>+</sup> cells, HIV virions and CTLs respectively<sup>324</sup>. The thymus produces CD4<sup>+</sup> cells with rate  $\lambda$ , which die with rate  $d$ . Uninfected CD4<sup>+</sup> cells become infected by HIV with rate  $k$  to produce infected CD4<sup>+</sup> cells, which die with rate  $\delta$  or are killed by CTLs with rate  $q$ . Regarding HIV, it is produced by the bursting of infected CD4<sup>+</sup> cells with burst size  $N$ , the total number of HIV virions an infected CD4<sup>+</sup> cell can produce in its lifetime, resulting in their death with rate  $\delta$  while HIV is cleared with rate  $c$ . CTLs proliferate with rate  $p$  upon encountering an infected CD4<sup>+</sup> cell and die with rate  $d_c$ .

Integrating the above model with the K-PD model for rituximab PD on CD19<sup>+</sup> cells, we therefore have the following 5 ODE model incorporating the drug effect of rituximab, now in terms of CD19<sup>+</sup> cells and EBV in place of CD4<sup>+</sup> cells and HIV;

$$\frac{dA_1}{dt} = -k_e \cdot A_1, \quad (4.14)$$

$$\frac{dA_2}{dt} = \lambda \cdot \left( \frac{T^\gamma}{T^\gamma + T50^\gamma} \right) - \mu \cdot \left( 1 + \frac{E_{max} \cdot A_1}{ED_{50} + A_1} \right) A_2 - kA_4A_2, \quad (4.15)$$

$$\frac{dA_3}{dt} = kA_4A_2 - \delta \cdot \left( 1 + \frac{E_{max} \cdot A_1}{ED_{50} + A_1} \right) \cdot A_3 - qA_3A_5, \quad (4.16)$$

$$\frac{dA_4}{dt} = N\delta A_3 - cA_4, \quad (4.17)$$

$$\frac{dA_5}{dt} = rA_3A_5 - dA_5, \quad (4.18)$$

where  $A_1$ ,  $A_2$ ,  $A_3$  and  $A_4$  are now compartments representing the serum into which rituximab is dosed, uninfected CD19<sup>+</sup> cells, infected CD19<sup>+</sup> cells and EBV virions respectively. Rituximab is eliminated with rate  $k_e$  from the serum, and is assumed to increase the death rates of both uninfected and infected CD19<sup>+</sup> cells. Following a delay due to HSCT, the bone marrow produces CD19<sup>+</sup> cells with rate  $\lambda$ , which die with rate  $\mu$ , enhanced by the B-cell killing effect of rituximab. Uninfected CD19<sup>+</sup> cells become infected by EBV with rate  $k$  to produce infected CD19<sup>+</sup> cells, which die with rate  $\delta$ , enhanced by the B-cell killing effect of rituximab, or are killed by CTLs with rate  $q$ . Regarding EBV, it is produced by the bursting of infected CD19<sup>+</sup> cells with a fixed burst size  $N$ , the total number of EBV virions an infected CD19<sup>+</sup> cell can produce in its lifetime, resulting in their death with rate  $\delta$  while EBV is cleared with rate  $c$ . CTLs proliferate with rate  $r$  upon encountering an infected CD19<sup>+</sup> cell and die with rate  $d$ . All parameters in the rituximab K-PD model were fixed to their final parameter estimates, as reported in Chapter 3. The viral burst size,  $N$  was fixed to 1000 in line with published values<sup>310</sup>.

Several assumptions were made when applying the model. Regarding rituximab, it was assumed that; none was present in the dosing compartment at time zero, that its elimination followed first-order kinetics and that it increased  $\mu$ . The initial condition of the uninfected CD19<sup>+</sup> cell compartment,  $A_2$ , was set to  $5 \times 10^6$  cells/L (half of the LLOQ of the assay) at time of HSCT. For the infected CD19<sup>+</sup> cell compartment,  $A_3$ ,  $0.05 \times 10^6$  cells/L at time of HSCT was set as the initial condition, assuming that 1% of uninfected CD19<sup>+</sup> cells become infected by EBV in line with a previous study of patients with glandular fever, in which 0.1-1% of B cells expressed EBV-encoded nuclear antigen<sup>325</sup>. The initial condition of the EBV compartment,  $A_4$ , was set to 100 copies/mL of whole blood (half of the LLOQ of the assay) and for the CTL compartment,  $A_5$ , an initial T cell

concentration of 168 cells/ $\mu\text{L}$  was set as estimated in post-HSCT paediatric patients by Hoare *et al*<sup>106</sup>.

The model was tested with and without the  $-kA_4A_2$  term in compartment  $A_2$ . If the  $-kA_4A_2$  term was omitted, the assumption was made that there was negligible loss of CD19<sup>+</sup> cells from compartment  $A_2$  due to EBV infection given the following biological rationale; that EBV does not destroy CD19<sup>+</sup> cells but transforms them as part of its biological mechanism, and that the total proportion of CD19<sup>+</sup> cells infected by EBV is very small<sup>325</sup>.

## 4.3 Results

### 4.3.1 Patient Characteristics

The model-building datasets for the Cox-PH model and the viral dynamic model comprised 56 children (median age at HSCT, 3.02 years; range, 0.3 - 14.0 years) and 30 children (median age at HSCT, 2.81 years; range, 0.7 - 14.5 years) respectively. Patients characteristics are summarised in Table 4.3. Although patients were followed up for up to three years after HSCT, the study period focussed on the first 100 days post-HSCT as EBV reactivation most commonly occurs in the first three months following HSCT.

Table 4.3: Patient and transplant characteristics for model-building datasets for Cox-PH model and NLME Model.\* denotes one patient who did not receive serotherapy in the dataset for the Cox-PH model. Of the 38 patients who had EBV reactivation in the first 100 days post-HSCT, eight patients were excluded from the viral dynamic model dataset as they did not receive rituximab in the first 100 days post-HSCT.

	Cox-PH Model ( $n = 56$ )	Viral Dynamic Model ( $n = 30$ )
<b>Age (years), median (range)</b>	3.0 (0.3 - 14.0)	2.8 (0.7 - 14.5)
<b>Diagnosis, <math>n</math> (%)</b>		
PID	19 (33.9)	5 (16.7)
NMH	12 (21.4)	6 (20.0)
MH	15 (26.8)	13 (43.3)
Other	10 (17.9)	6 (20.0)
<b>Donor Type, <math>n</math> (%)</b>		

	Cox-PH Model ( $n = 56$ )	Viral Dynamic Model ( $n = 30$ )
MSD	6 (10.7)	3 (10.0)
MFD	4 (7.1)	1 (3.3)
MUD	28 (50.0)	20 (66.7)
MMFD	1 (1.8)	0
MMUD	15 (26.8)	6 (20.0)
Haplo	2 (3.6)	0
<b>Stem Cell Source, <math>n</math> (%)</b>		
BM	32 (57.1)	20 (66.7)
PBSC	24 (42.9)	10 (33.3)
<b>Conditioning, <math>n</math> (%)</b>		
MAC	22 (39.3)	15 (50.0)
MIC	1 (1.8)	0
RIC	32 (57.1)	15 (50.0)
None	1 (1.8)	0
<b>Serotherapy*, <math>n</math> (%)</b>		
Alemtuzumab	40 (72.7)	16 (53.3)
ATG	15 (27.3)	14 (46.7)
<b>Recipient EBV Serostatus, <math>n</math> (%)</b>		
Positive	26 (46.4)	18 (60.0)
Negative	30 (53.6)	12 (40.0)
<b>Donor EBV Serostatus, <math>n</math> (%)</b>		
Positive	52 (92.9)	29 (96.7)
Negative	4 (7.1)	1 (3.3)

### 4.3.2 Clinical Outcomes

Of the 56 patients in the Cox-PH model, 38 (67.9%) had an initial EBV reactivation in the first 100 days since HSCT, with a median time to EBV reactivation of 40 days (range, 14-97 days) and a median peak EBV VL of 255,000 copies/mL (range, 403-32,479,800 copies/mL). Forty-one patients received a single dose of rituximab on a conservative regimen whilst 15 patients received four doses on a pre-emptive regimen. There were no deaths due to EBV reactivation, or any other reasons, in the study period. Although they did not have EBV reactivation in the study period, one patient progressed to PTLT 168 days post-HSCT and started rituximab treatment the following day. This patient was 7.83 years at HSCT, and had the following features predisposing to EBV: diagnosis

of X-linked lymphoproliferative disease; received RIC regimen of alemtuzumab, fludarabine and melphalan; the HSC source was PBSC; had a mismatched unrelated donor. A violin plot of the median peak EBV VL stratified by number of rituximab doses has been plotted in Figure 4.4, and EBV VL against time since EBV reactivation stratified by early CD4<sup>+</sup> T cell reconstitution has been plotted in Figure 4.5.

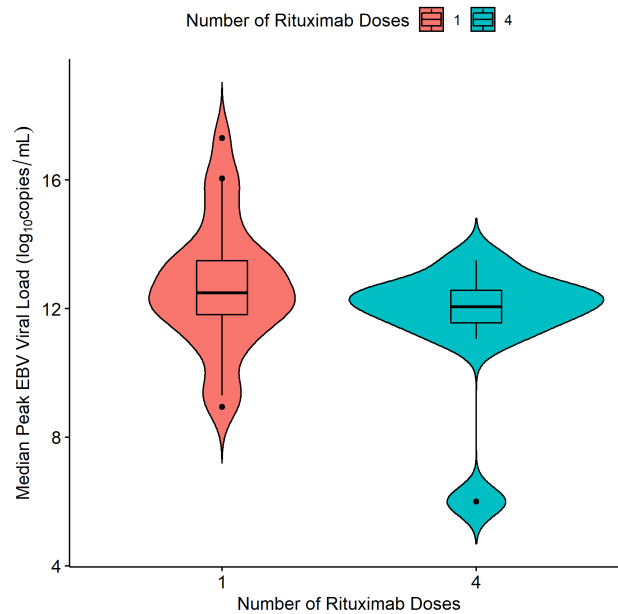


Figure 4.4: Violin plot of median peak EBV VL stratified by number of rituximab doses received. Black horizontal line represents median peak EBV VL for the dose number and box represents interquartile range. Black dots represent median peak EBV VLs lying outside the interquartile range and coloured shape represents the distribution of the data.

### 4.3.3 Cox-PH Model

Univariate and multivariate Cox-PH modelling results are shown in Tables 4.4 and 4.5 respectively. In univariate analysis, a PID diagnosis, AUC<sub>0-100</sub> of CD8<sup>+</sup> T cells, serotherapy with ATG, HSC source of peripheral blood and EBV seropositivity of HSCT recipient were significantly associated with increasing the risk of EBV reactivation. Of these, two covariates were found to significantly increase risk of EBV reactivation in multivariable analysis; EBV seropositivity of the HSCT recipient and pre- HSCT administration of ATG (adjusted hazard ratio (HR) = 2.32,  $p = 0.02$ ; AHR = 2.55,  $p = 0.04$ ). Kaplan-Meier curves of the cumulative fraction of patients with EBV reactivation stratified by these two covariates have been visualised in Figure 4.6.



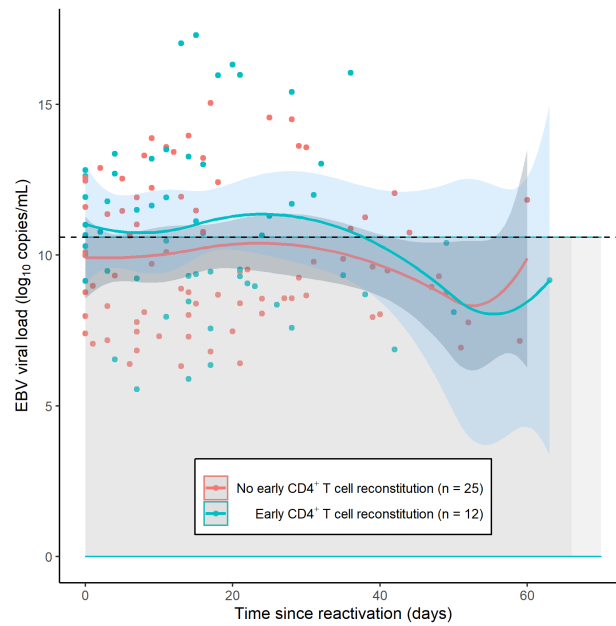


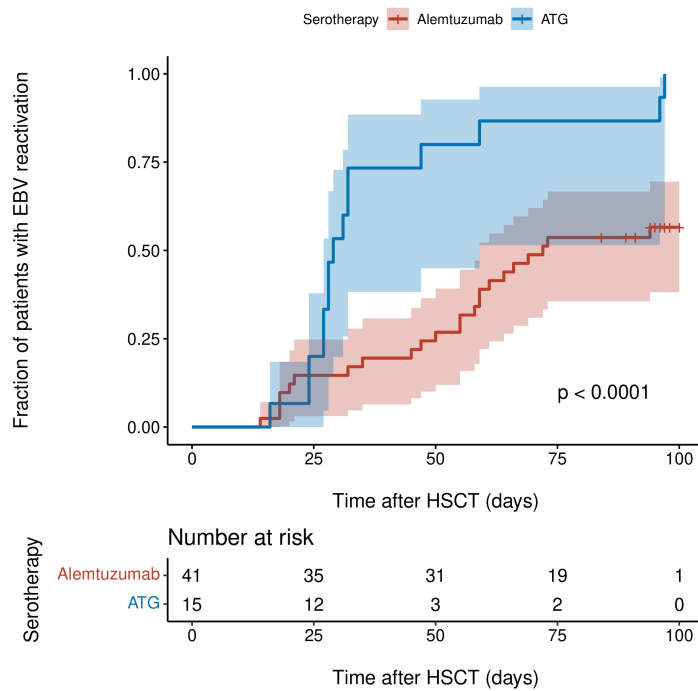
Figure 4.5: EBV VL against time since EBV reactivation, stratified by early CD4 T cell reconstitution, as defined by Admiraal *et al*<sup>49</sup>. Curves are from spline regression (2df) of EBV VL with time, with VL measurements normalised to two weeks before EBV reactivation. Points are an individual patient's measured VL and grey shaded region signifies VL measurements below 40,000 copies/mL, the threshold to treat with rituximab.

Table 4.4: Univariate Cox-PH model for time to first EBV reactivation in first 100 days post-HSCT. PID, primary immunodeficiency; HSC, haematopoietic stem cell; PBSC, peripheral blood stem cell; BM, bone marrow; EBV, Epstein-Barr virus;  $AUC_{0-100}$ , area under the curve from day of HSCT to 100 days post-HSCT; ALC, absolute lymphocyte count; MSD, matched sibling donor; MFD, matched familial donor; MUD, matched unrelated donor; MMFD, mismatched familial donor; MMUD, mismatched unrelated donor; Haplo, haploidentical donor; MAC, myeloablative conditioning; MIC, minimal-intensity conditioning; RIC, reduced-intensity conditioning; ATG, anti- thymocyte globulin. HR, hazard ratio; CI, confidence interval. – denotes a continuous variable.

Covariate	Term (Reference)	<i>P</i> Value	HR	95% CI
PID Diagnosis	Yes (No)	0.01	0.37	0.17 - 0.82
HSC Source	PBSC (BM)	0.02	0.44	0.22 - 0.87
Age	-	0.41	1.03	0.95 - 1.12
Rituximab Doses	-	0.25	0.86	0.67 - 1.11
Donor EBV Serostatus	Seropositive (Seronegative)	0.83	1.17	0.28 - 4.87
Recipient EBV Serostatus	Seropositive (Seronegative)	0.003	2.67	1.39 - 5.12
$AUC_{0-100}$ ALC	-	0.90	0.99	0.83 - 1.18
$AUC_{0-100}$ CD19	-	0.65	0.99	0.95 - 1.03
$AUC_{0-100}$ CD4	-	0.77	0.99	0.96 - 1.03
$AUC_{0-100}$ CD8	-	0.005	1.02	1.01 - 1.04
Donor Type	MMFD/MMUD/Haplo (MFD/MSD)	0.11	0.43	0.16 - 1.21
	MUD (MFD/MSD)	0.27	1.58	0.71 - 3.56
Conditioning Regimen	RIC (MIC/MAC/None)	0.46	0.78	0.41 - 1.50
Serotherapy	ATG (Alemtuzumab)	0.0001	3.74	1.90 - 7.36

Table 4.5: Multivariate Cox-PH model for time to first reactivation in first 100 days post-HSCT. PID, primary immunodeficiency; HSC, haematopoietic stem cell; PBSC, peripheral blood stem cell; BM, bone marrow; EBV, Epstein-Barr virus;  $AUC_{0-100}$ , area under the cell-time curve from 0-100 days post-HSCT; ATG, anti-thymocyte globulin. HR, hazard ratio; CI, confidence interval. – denotes a continuous variable.

Covariate	Term (Reference)	<i>P</i> Value	HR	95% CI
PID Diagnosis	Yes (No)	0.10	0.48	0.20 - 1.14
HSC Source	PBSC (BM)	0.48	0.74	0.32 - 1.70
Recipient EBV	Seropositive	0.02	2.33	1.15 - 4.73
Serostatus	(Seronegative)			
$AUC_{0-100}$ CD8	-	0.20	1.01	0.99 - 1.03
Serotherapy	ATG (Alemtuzumab)	0.04	2.55	1.07 - 6.11



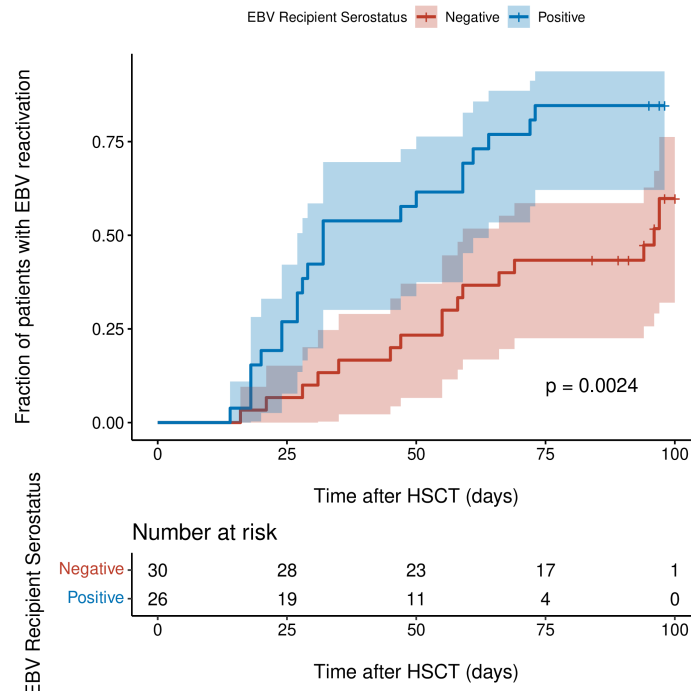


Figure 4.6: Kaplan-Meier curves of cumulative fraction of patients with EBV reactivation in first 100 days post-HSCT stratified by type of serotherapy (ATG or alemtuzumab) and EBV serostatus of recipient (negative or positive). P values were calculated using the log-rank test and denote the difference between the two subgroups. Shaded regions show 95% confidence interval.

### 4.3.4 Sensitivity Analysis

Of the 25 parameters in the model, 13 parameters were found to be sensitive on account of an RMSD value greater than zero. In Figure 4.7, an inverted plot of the log of the RMSD against the parameters in the model of Akinwumi is shown for a single parameter value of 10. In addition, simulated EBV VL trajectories have been visualised against time since reactivation for parameter values in the range  $1 \times 10^{-5}$  -  $1 \times 10^3$ , using the  $B_m$  compartment as a proxy for EBV VL (Figure 4.8). Parameters identified as key determinants of EBV VL were those related to latently infected memory B cells and CTLs, as follows:  $\delta_2$ , CTL killing rate of infected B cells expressing the default programme;  $r_m$ , the proliferation rate of latently infected memory B cells;  $\omega_m$ , the reactivation rate of latently infected memory B cells into lytically infected memory B cells;  $\delta_m$ , the death rate of latently infected memory B cells and  $r_2$ , the rate of CTL activation against infected B cells expressing the default programme.

### 4.3.5 Viral Dynamic Model

#### 4.3.5.1 Model Fitting

The five-compartment model was fitted to 613 log-transformed EBV VL measurements from 30 children, with the Laplacian conditional estimation with interaction algorithm and the ADVAN13 subroutine. An additive model was used to describe the residual error, and the M5 method was implemented to handle the EBV VL measurements that were BLQ ( $n = 323$ , 52.7%). A schematic of the model for EBV dynamics and CD19<sup>+</sup> cell dynamics is shown in Figure 4.9, plots of all raw EBV VLs used for model-building are shown in Figures 4.10 and 4.11, and a subset of individual plots of EBV VLs with rituximab dosing, CD19<sup>+</sup> cells and CD4<sup>+</sup> cells are depicted in Figure 4.12.

Regarding the initial conditions of the compartments, the following assumptions were made; that no rituximab was present in  $A_1$ ,  $5 \times 10^6$  CD19<sup>+</sup> cells/ $\mu$ L (half of the LLOQ) were present on day zero (the day of HSCT) in  $A_2$ ,  $0.05 \times 10^6$  CD19<sup>+</sup> cells/ $\mu$ L, i.e. 1% of the B cells, were infected with EBV in  $A_3$  on day zero, a EBV VL of 100 copies/mL of whole blood (half of the LLOQ) was present in  $A_4$  and the initial CD8<sup>+</sup> cell concentration was 168 cells/ $\mu$ L on day zero (the day of HSCT) in  $A_5$ <sup>106</sup>.

#### 4.3.5.2 Parameter Estimates

The parameter estimates estimated from the viral dynamic model-building dataset have been given in Table 6. Parameters related to infected CD19<sup>+</sup> cells, EBV and CTLs were estimated while

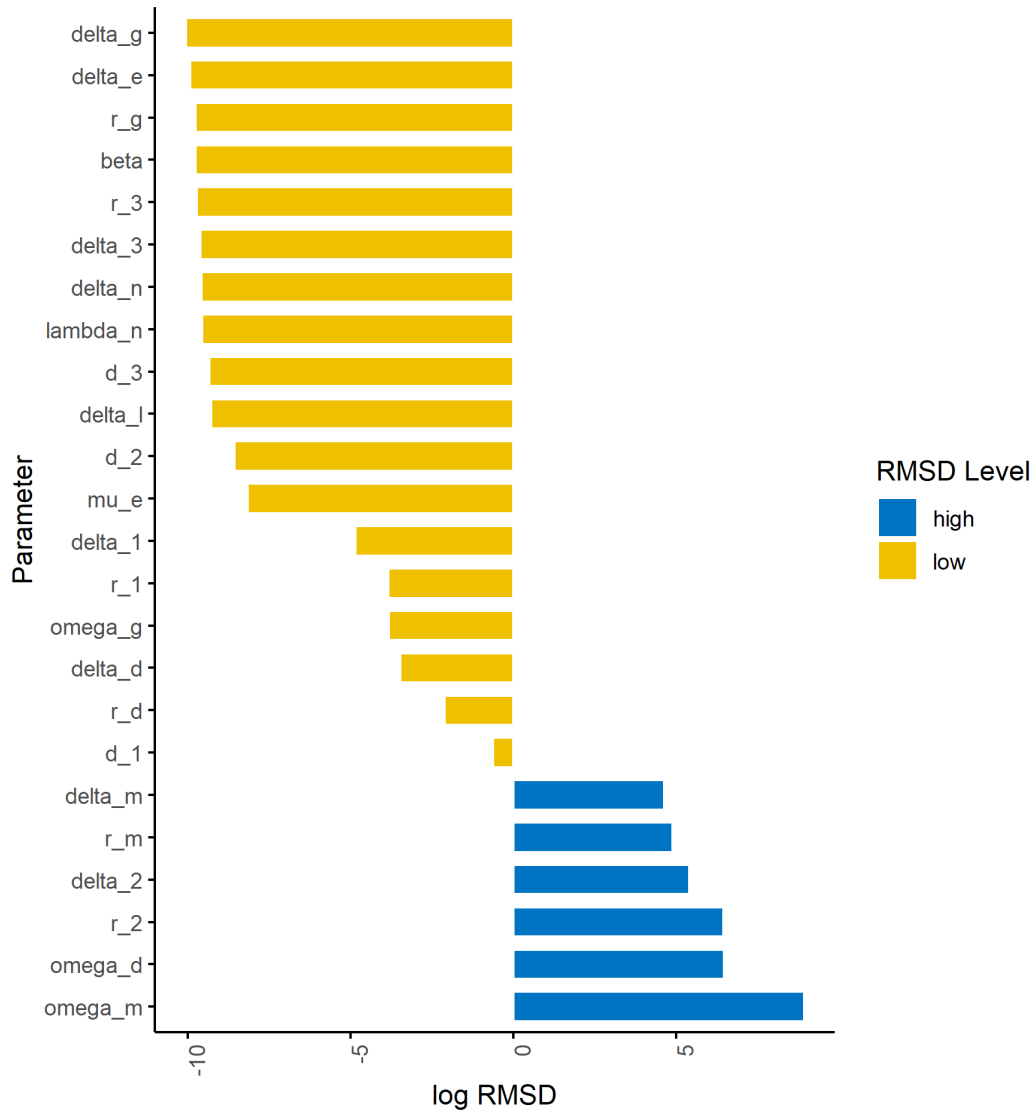


Figure 4.7: Plot to show sensitivity of parameters when parameter value is set to 10, evaluated using RMSD. Log RMSD has been plotted for presentation purposes. RMSD, root mean squared distance.

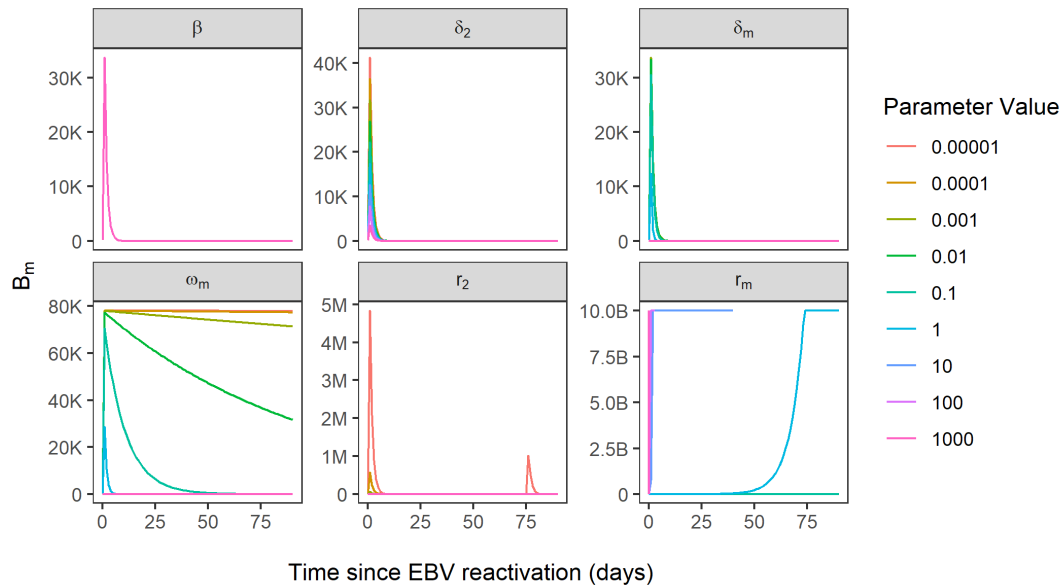


Figure 4.8: Simulated EBV VL trajectories, using  $B_m$  compartment as a proxy for EBV VL. Sensitivity of EBV VL shown for the variation of six parameters over the range of values 0.00001-1000, where  $\beta$  parameter represents reference model fit and all other parameters are sensitive parameters. B, one billion; M, one million; K, 1000.

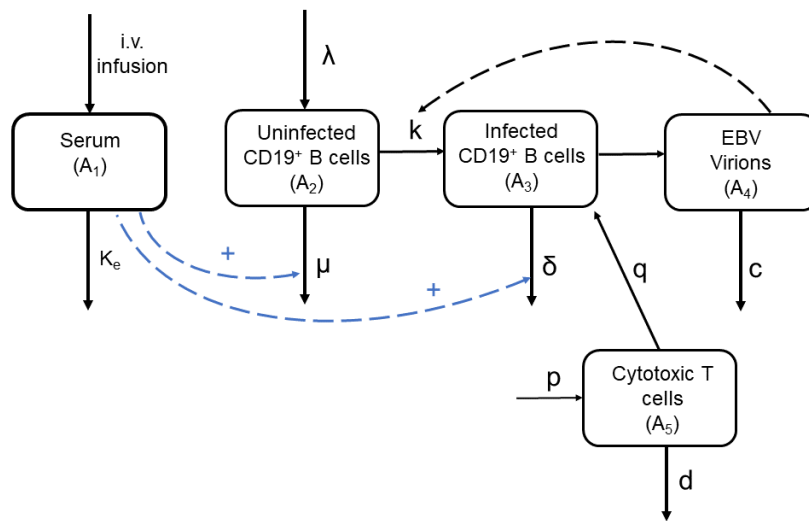


Figure 4.9: Schematic of model of EBV dynamics and CD19<sup>+</sup> cell dynamics post-HSCT.

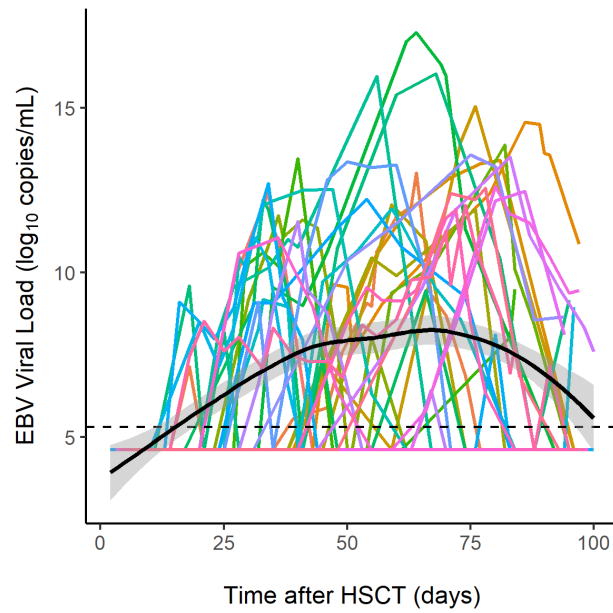


Figure 4.10: Raw EBV VL measurements in viral dynamic model-building dataset ( $n = 30$ ). Each coloured line represents EBV VL trajectory for an individual patient. The black dotted line is the LLOQ of the assay used to measure EBV VL (200 copies/mL). The thick black line is the local regression curve, and the grey shaded area is the 95% confidence interval. X-axis shows time since HSCT (days).



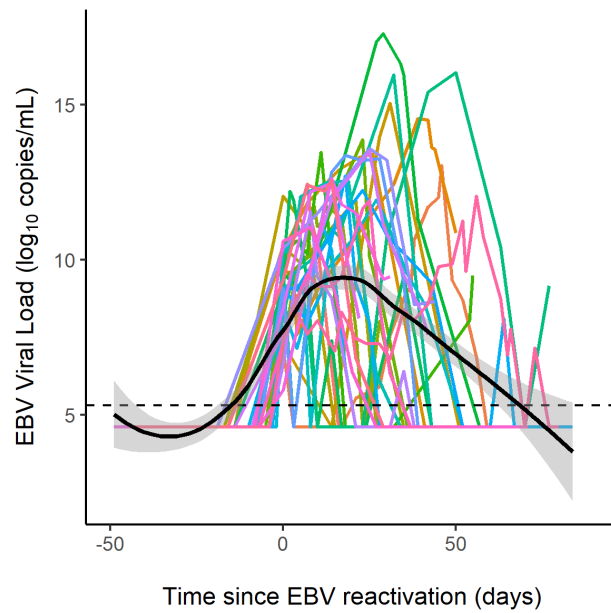


Figure 4.11: Raw data used for building viral dynamic model. Each coloured line is an individual patient and the black dotted line represents LLOQ of the EBV VL assay (200 copies/mL). The thick black line is the local regression curve, and the grey shaded area is the 95% confidence interval. X-axis shows time since EBV reactivation, where each patient's VL measurements were normalised to the start of their reactivation event. time since EBV reactivation, where each patient's VL measurements were normalised to the start of their reactivation event.

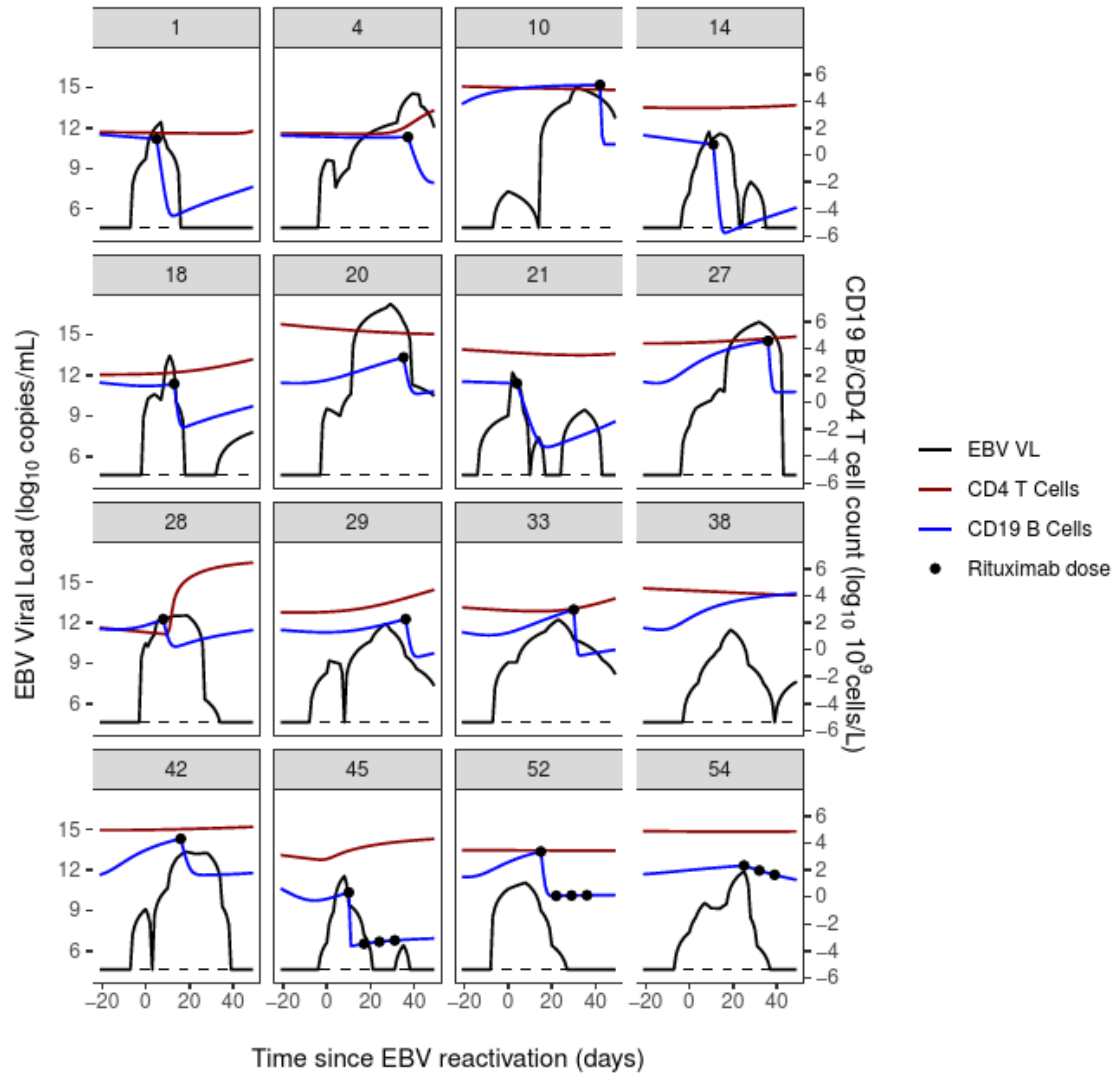


Figure 4.12: Individual trajectories of EBV VL, CD19<sup>+</sup> cell and CD4<sup>+</sup> cell counts and rituximab dosing for 16 patients. Black line is EBV VL, blue line is CD19<sup>+</sup> cell count, brown line is CD4<sup>+</sup> cell count and black dots indicate rituximab administrations. Dotted black line represents the lower limit of detection of the EBV VL assay (200 copies/mL). CD4<sup>+</sup> cell counts were predicted using a published PD model for CD4<sup>+</sup> cell reconstitution post-HSCT in children<sup>106</sup> and CD19<sup>+</sup> cell counts were predicted using the Chapter 3 K-PD model for the effect of rituximab on CD19<sup>+</sup> cell reconstitution post-HSCT in children. For EBV VL, observed measurements spanning from three weeks pre- to seven weeks post-HSCT were plotted, and were linearly interpolated to obtain a continuous range of data points for 0-100 days post-HSCT. In the absence of a published mathematical model for CD8<sup>+</sup> cell reconstitution post-HSCT and a sparsity of observed CD8<sup>+</sup> cell counts disabling linear interpolation, CD8<sup>+</sup> cell counts were not visualised.

uninfected CD19<sup>+</sup> cell and rituximab parameters were fixed to the parameter estimates of the final K-PD model from Chapter 2. In addition, the EBV viral burst size was fixed to a literature value<sup>310</sup>. From the EBV clearance rate,  $c$ , the half-life of an EBV virion was calculated ( $\ln 2 / c$ ) as 10.06 days.

Table 4.6: Estimated parameter values from EBV viral dynamic model.  $\lambda$ , CD19<sup>+</sup> cell production rate constant;  $\mu$ , CD19<sup>+</sup> cell death rate constant;  $\gamma$ , Steepness of slope of CD19<sup>+</sup> cell recovery;  $T50$ , Time to half-maximal output of CD19<sup>+</sup> cells from bone marrow;  $k_e$ , Rituximab elimination rate constant;  $E_{max}$ , Maximum killing effect of rituximab on CD19<sup>+</sup> cells;  $ED_{50}$ , Rituximab dose producing 50% of maximum killing effect;  $k$ , Infected CD19<sup>+</sup> cell production rate constant;  $\delta$ , Infected CD19<sup>+</sup> cell death rate constant;  $q$ , CTL killing rate of infected cells;  $N$ , Viral burst size;  $c$ , Viral clearance rate;  $r$ , CTL proliferation rate constant;  $d$ , CTL death rate constant; RSE, relative standard error; BSV, between-subject variability; CI, confidence interval.

Parameter (units)	Estimate (%RSE)	%BSV (%RSE)	Shrinkage (%)	Bootstrap Median (95% CI)
$\lambda$ ( $\times 10^6$ cells/day)	1.40 (fixed)	92.36 (14.07)	59.7	-
$\mu$ (cells/day)	0.018 (fixed)	117.05 (19.93)	27.7	-
$\gamma$	3.18 (fixed)	-	-	-
$T50$ (days)	44.80 (fixed)	147.65 (46.79)	48.6	-
$k_e$ (/day)	0.109 (fixed)	-	-	-
$E_{max}$	84.40 (fixed)	-	-	-
$ED_{50}$ (mg)	0.921 (fixed)	-	-	-
$k$ ( $\times 10^6$ cells/day)	0.112 (28.75)	12.00 (22.78)	83.7	0.112 (0.0961 - 0.134)
$\delta$ (cells/day)	5.86 $\times$ $10^{-5}$ (23.72)	14.93 (64.13)	87.7	5.86 $\times 10^{-5}$ (5.18 $\times 10^{-5}$ - 9.86 $\times 10^{-5}$ )
$q$ (cells/day)	2.30 $\times 10^{-3}$ (20.65)	0.62 (984.38)	99.1	2.32 $\times 10^{-3}$ (2.10 $\times 10^{-3}$ - 3.14 $\times 10^{-3}$ )
$N$	1000 (fixed)	-	-	-
$c$ (virions/day)	0.0829 (20.27)	1.64 (462.69)	97.0	0.0842 (0.0788 - 0.107 )

Parameter (units)	Estimate (%RSE)	%BSV (%RSE)	Shrinkage (%)	Bootstrap Median (95% CI)
$r$ (cells/day)	$3.26 \times 10^{-6}$ (24.14)	24.54 (135.88)	66.2	$3.26 \times 10^{-6}$ ( $3.12 \times 10^{-6}$ - $3.81 \times 10^{-6}$ )
$d$ (cells/day)	$1.23 \times 10^{-4}$ (983.74)	155 (829.88)	99.0	$1.23 \times 10^{-4}$ ( $1.08 \times 10^{-4}$ - $1.25 \times 10^{-4}$ )

#### 4.3.5.3 Model Evaluation

Goodness-of-fit plots, seen in Figure 4.13, and a pcVPC, seen in Figure 4.14, were produced to evaluate the model. For the pcVPC, 200 datapoints were simulated from the parameter values estimated by the model and the fraction of data that were BLQ were included in the bottom panel. In general, model evaluation suggested adequate comparability between the observed data and model-predicted data. The plots of the observed data against population predictions and individual predictions respectively demonstrated a reasonable fit, with the overall trend of the data clustering along the line of unity. For the residual error model, the plot of the conditional weighted residuals (CWRES) against time since HSCT showed a normal distribution with a mean of zero and most of the data between  $\pm 2$  standard deviations of the mean. However, there appears to be a slight pattern developing with time since HSCT. Regarding the plot of the absolute individually weighted residuals (IWRES) against individual predictions, most of the data are scattered along a flat line with a trough at 100 copies/mL, half of the LLOQ, due to the BLQ data. The pcVPC demonstrates some consistency between the observed data and simulated percentiles. There is variability observed at the lowest and highest EBV VL measurements, with a wide 95% prediction interval for the 97.5th percentile. The proportion of the BLQ data are well-captured by the model using the M5 method with the exception of early post-HSCT timepoints. In general, all CTL-related parameters were estimated with high relative standard error.

## 4.4 Discussion

In this chapter, the dynamics of EBV reactivation post-HSCT have been methodically studied in a paediatric cohort. A multivariate Cox-PH model was first developed, and identified pre-HSCT ATG administration and EBV seropositivity of the HSCT recipient as significant risk factors for an initial EBV reactivation event in the first 100 days post-HSCT. In addition, to the best of the author's knowledge, sensitivity analysis was performed for the first time on a previously reported mechanistic mathematical model of EBV viral kinetics to detect key parameters driving EBV VL<sup>320</sup>.

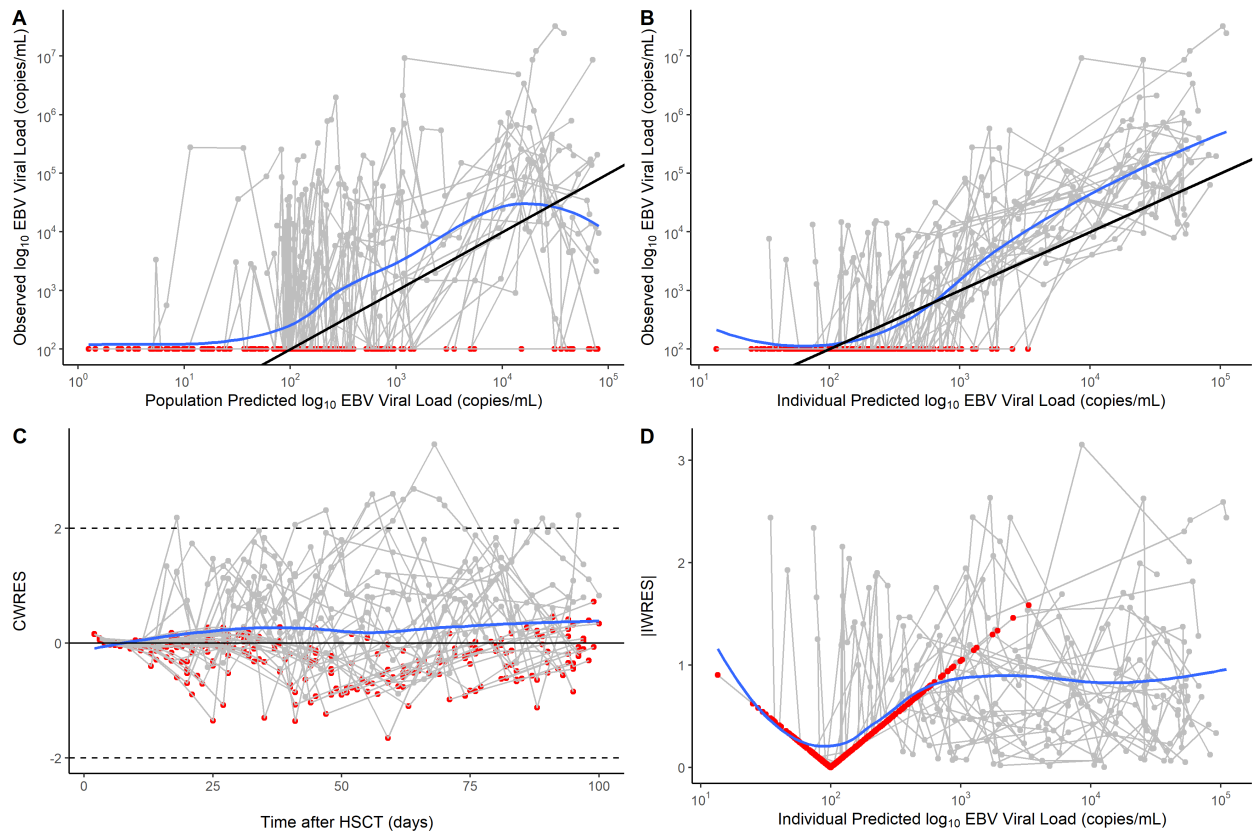


Figure 4.13: Goodness-of-fit plots for EBV viral dynamic model. A) Observed EBV VL vs Population Predicted EBV VL. B) Observed EBV VL vs Individual Predicted EBV VL. C) CWRES vs Time after HSCT. D)  $|IWRES|$  vs Individual Predicted EBV VL. Blue lines are the local regression curves and red data points are EBV VL measurements that were BLQ.

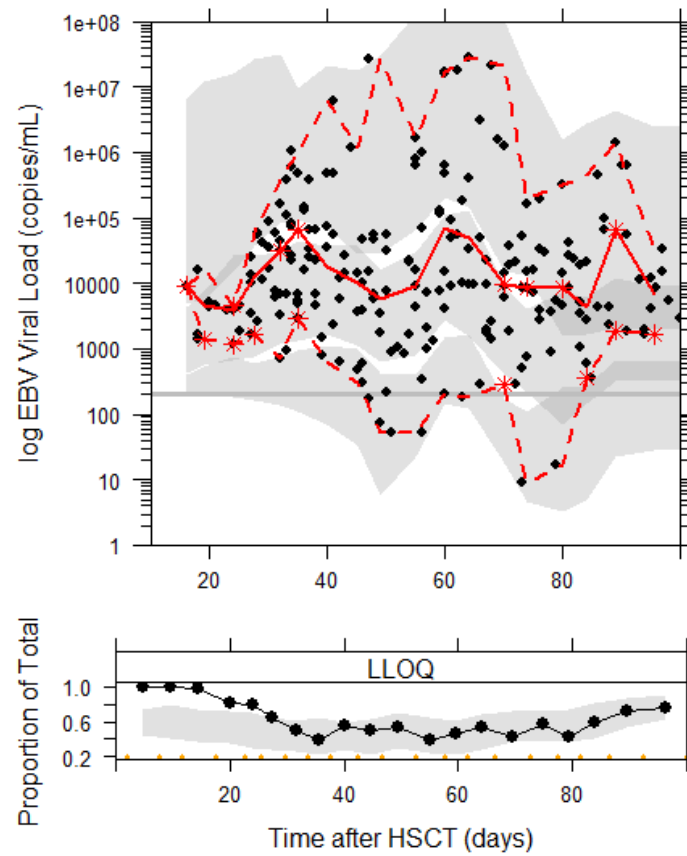


Figure 4.14: Prediction-corrected Visual Predictive check for viral dynamic model. Black dots are observed EBV VLs and the solid red line is the observed median. The dotted red lines are the observed 2.5th, 50th and 97.5th percentiles and the grey shaded area are the 95% prediction intervals. The bottom panel shows the proportion of total data that were BLQ.

Furthermore, the previously developed rituximab K-PD model in Chapter 3 was leveraged by integrating it with a published viral dynamic model<sup>324</sup> to construct a novel mechanistic NLME model of EBV viral dynamics and CD19<sup>+</sup> cell dynamics under the influence of rituximab.

ATG has been widely reported to be associated with a higher incidence of EBV reactivation post-HSCT therefore the result that pre-HSCT ATG significantly increases the risk of EBV reactivation corroborates these previous findings<sup>207,289,326,327</sup>. Even though it is administered as part of the conditioning regimen for GvHD prophylaxis in the weeks pre-HSCT, ATG's T-cell depletive effect lasts well into the early post-HSCT period due to its long half-life of 29.8 days<sup>326</sup>. This exacerbates the reconstituting CD8<sup>+</sup> T cell compartment including the already reduced CTL-mediated immune surveillance of EBV post-HSCT. In the study, 100% (15 of 15) of patients who received ATG had EBV reactivation in the first 100 days post-HSCT while only 57.5% (23 of 40) of patients who received alemtuzumab had EBV reactivation, a finding comparable with previous studies, most probably attributed to alemtuzumab's broader lymphocyte depletion of B cells, including those that are EBV-infected<sup>98,205,207,218</sup>. Although the historical consensus is that EBV serological donor/recipient mismatch increases risk of EBV reactivation, most studies ascribe EBV-associated PTLD to donor-derived EBV<sup>288,328</sup>. This contradicts our finding that EBV seropositivity of the HSCT recipient is a risk factor for EBV reactivation, which has been observed previously in another paediatric post-HSCT study<sup>329</sup>. As the focus of the current study was on the first EBV reactivation event post-HSCT, a study period of the first 100 days post- HSCT was chosen when reactivation is most likely to occur. In contrast, many studies of EBV reactivation have much longer study periods spanning from six months to nearly five years post-HSCT<sup>38,49,330–332</sup>. At these later timepoints post-HSCT, there would be more donor-derived cells due to increased chimerism, which we might not have been able to capture in the study period of 100 days post-HSCT. This is also evident when looking at the EBV serological donor/recipient combinations in the patient cohort; in EBV seropositive donors with EBV seronegative recipients, 55.2% (16 of 29) of patients had an EBV reactivation while 87.0% (20 of 23) of patients who were EBV-seropositive and had EBV-seropositive donors experienced an EBV reactivation event. There were only three patients who were EBV seropositive and had EBV seronegative donors, of which two had EBV reactivation. Having access to chimerism data at post-HSCT timepoints for the study patients might help to shed further light on this result.

The incidence of EBV reactivation of 67.9% was high but similar to that observed in some previous studies<sup>333,334</sup>. The first 100 days post-HSCT is when EBV reactivation, or indeed viral reactivation in general, is most likely to occur<sup>335</sup>, therefore a higher incidence may be expected compared to lower incidences observed across much longer study periods. In addition, it is recognised that the incidence of EBV reactivation post-HSCT varies depending on the transplant type, sensitivity of the EBV quantification assay, definitions of thresholds of EBV viraemia and timing of reactivation<sup>219</sup>. Regarding the onset of the EBV reactivation event, the median time of reactivation in the patient

cohort was 40 days post-HSCT, which aligned well with previously reported times ranging from 34-45 days<sup>222,336,337</sup>.

In general, highly variable EBV VL dynamics were exhibited by the post-HSCT patients in the model-building dataset, typical of acute infection, as documented before<sup>209,338</sup>. Although some patients experienced multiple reactivation events over the course of their recovery post-HSCT, the study period of the first 100 days post-HSCT was chosen to focus on the first EBV reactivation event encountered. The visualised trajectories of EBV VL, CD19<sup>+</sup> cells and CD4<sup>+</sup> cells in response to EBV and rituximab for individual patients in Figure 4.12 illustrated the complexity and variability of EBV dynamics between patients. A decrease in CD19<sup>+</sup> cell count occurred shortly after the first rituximab dose was administered, as per the B-cell depleting mechanism of action of rituximab and was coupled with a contemporaneous decrease in EBV VL in all patients. Conversely, CD4<sup>+</sup> cell counts remained stable in most patients during the reactivation, in line with a previous study which reported no increase in CD4<sup>+</sup> cell counts after viral reactivation<sup>49</sup>. Patterns of EBV dynamics demonstrated slow and rapid growth as well as partial and complete clearance in response to rituximab, as observed for other post-HSCT viral reactivations such as CMV<sup>339</sup>. In addition, it can be inferred from Figure 4.12 that subsequent rituximab doses in patients may not further decrease CD19<sup>+</sup> cell count and consequently EBV VL, as suggested by patients 45, 52 and 54. To produce Figure 4.12, previously developed mathematical models by our group for CD4<sup>+</sup> cell reconstitution post-HSCT in children<sup>106</sup> and the Chapter 3 K-PD model for the effect of rituximab of CD19<sup>+</sup> cell reconstitution post-HSCT in children were utilised to predict CD4<sup>+</sup> cell and CD19<sup>+</sup> cell counts respectively for the first 100 days post-HSCT, as there were limited observed immune cell counts from patients due to lymphopenia in the early post-HSCT period.

Upon conducting a literature review of previously published models of EBV dynamics, the mechanistic viral kinetic model reported by Akinwumi was deemed to be the most applicable to the patient cohort as it was the only model developed for the post-HSCT setting<sup>320</sup>. The major finding from sensitivity analysis of this model was that parameters related to latent memory B cells and CTLs determined changes in EBV VL, which aligned with the well-established role that these two cell types have in the biological mechanism of EBV reactivation. In addition, the relevance of these parameters have been demonstrated by experimental studies. For example, Burns *et al* observed an increase in the number and proportion of CD27<sup>+</sup> memory B cells in peripheral blood samples of post-HSCT patients that were latently infected with EBV and expressed the cell proliferation marker Ki67, highlighting the importance of the  $r_m$  (proliferation rate of infected B cells),  $\omega_m$  (reactivation rate of latently infected B cells into lytically infected B cells) and  $\delta_m$  (death rate of infected B cells) parameters<sup>280</sup>. Regarding  $\delta_2$  (CTL killing rate of infected B cells) and  $r_2$  (rate of CTL activation against infected B cells), such CTL parameters have long featured in viral dynamic models since the earliest characterisation of the host immune response against virus-infected cells<sup>295,296</sup>.



The pivotal role of CTLs in reducing EBV VL continue to be demonstrated in the prevention and treatment of EBV-associated PTLD, both experimentally and clinically<sup>340–343</sup>. Informed by the sensitivity analysis, these five parameters then formed a simplified version of the original model of Akinwumi. However, attempts to fit this simplified model to the patient EBV VL measurements proved unsuccessful, even when most parameters were fixed to published literature values and one parameter was estimated at a time. There are several possible explanations for this. Firstly, the initial parameter estimates were based on literature values that were all derived from agent-based simulation and not from clinical data from patients. In the absence of other estimated literature values, these were used but their biological plausibility remained unconfirmed. Another setback encountered during implementation was failure of the model to converge for a range of estimation algorithms in NONMEM, suggesting model instability or parameters not being identifiable. Similar issues were recently documented by Margetts in his pursuit to construct a viral kinetic model for post-HSCT CMV dynamics<sup>344</sup>.

In light of these challenges, the rituximab K-PD model developed in Chapter 3 was combined with a published viral dynamic model to build a pharmacometric model for EBV reactivation dynamics post-HSCT. There were several rationale for this. Firstly, the patients in the model-building dataset for the rituximab K-PD model were the same patients whose data were used to build the EBV Cox-PH model and viral dynamic model therefore we built on prior knowledge gained of the system. This meant that scaling for age-related effects and HSCT-specific parameters were already present at the structural level of the model, as well as the the drug effect of rituximab, the treatment for EBV reactivation post-HSCT. Lastly, the inclusion of the model by Wang *et al* introduced a virus compartment and CTL compartment. Taken together, these features resulted in the compartments of the final viral dynamic model encompassing the relevant viral, drug, host cell and host immune response aspects of the biological mechanism of EBV reactivation. Also of note, several of the sensitive parameters in the Akinwumi model were present in the EBV viral dynamic model thereby incorporating the knowledge gained from the sensitivity analysis ( $k$  represents  $r_m$ ,  $\delta$  represents  $\delta_m$  and  $q$  represents  $\delta_2$ ).

In general, the viral dynamic model adequately described aspects of the EBV VL patient profiles observed in the post-HSCT cohort, with most parameters estimated with reasonable precision. The estimated value of  $0.112 \times 10^6$  cells/day (95% CI:  $0.0961 \times 10^6$  -  $0.134 \times 10^6$ ) for the proliferation rate of infected CD19<sup>+</sup> cells,  $k$ , was 12.5-fold larger than for uninfected CD19<sup>+</sup> cells,  $1.4 \times 10^6$  cells/day (95% CI,  $0.852 \times 10^6$  -  $1.98 \times 10^6$ ). While there are no published proliferation rates for EBV-infected CD19<sup>+</sup> cells, to the best of the author's knowledge, and given that CD19<sup>+</sup> cells include naive, memory and EBV-induced blasting plasma cells, this increased rate could be attributed to the uncontrolled proliferation of B cells induced by EBV transformation compared to the normal levels of proliferation expected for uninfected B cells in the absence of EBV. This finding also aligns with

a study by Burns *et al*, who observed an increase in the number and proportion of CD27<sup>+</sup> memory B cells in peripheral blood samples of post-HSCT patients that were latently infected by EBV and expressed the cell proliferation marker Ki67<sup>280</sup>. Furthermore, it has been demonstrated that memory B cells are the site of EBV persistence both in healthy immunocompetent individuals and immunocompromised post-HSCT patients in vivo<sup>27,280</sup> and a higher proliferation rate for CD27<sup>+</sup> memory B cells than for CD27<sup>-</sup> naive B cells has previously been reported<sup>178</sup>. The derived half-life for infected CD19<sup>+</sup> cells of 32 years, whilst not biologically plausible in children, is consistent with the range of 31-41 years observed by Hoshino *et al* in healthy adults<sup>345</sup>. Regarding the estimated death rate for infected CD19<sup>+</sup> cells ( $\delta$ ),  $5.86 \times 10^{-5}$  cells/day (95% CI:  $5.18 \times 10^{-5}$  -  $9.86 \times 10^{-5}$ ), this was 4-fold lower than the published value generated from simulation by Shapiro *et al*,  $2.32 \times 10^{-4}$  cells/day, and 1000-fold lower than the death rate of 0.06 cells/day derived from Macallan *et al*'s reported half-life of 11 days for memory B cells<sup>178,310</sup>. With regards to the death rate derived from Macallan *et al*, this death rate could be higher as it applies to all memory B cells, including uninfected memory B cells, whereas only a very small proportion of the total memory B cell compartment become infected by EBV hence the lower death rate estimated by the model. Another possible explanation for this discrepancy could be related to the viral burst size,  $N$ . Despite being fixed to 1000 in line with literature values<sup>317,318</sup>, this value was based on healthy adults, who are inherently different to the immunocompromised post-HSCT paediatric patient cohort under study. In addition, a model assumption made when setting the initial condition of the infected B cell compartment was that 1% of all B cells are infected by EBV, supported by a study conducted in patients with glandular fever<sup>325</sup>.

In contrast, the model estimated value for the EBV clearance rate ( $c$ ), 0.0829 virions/day, and the derived EBV half-life of 8.36 days, were in reasonable agreement with published values for patients, albeit marginally higher. Previously reported EBV half-lives were in the range of 0.9-5.4 days for post-HSCT patients treated with rituximab<sup>209</sup>, a mean of 3.2 days calculated by Funk *et al* from four historic studies in transplant patients<sup>338,340,346,347</sup>, in the range of 0.51-1.97 days for post-HSCT rituximab-treated patients and 2.5-12.6 days for non-rituximab patients<sup>288</sup> and lastly, 1.85-28.29 days for patients with nasopharyngeal carcinoma<sup>348</sup>.

With regards to the CTL killing rate,  $q$ , this was estimated as  $2.3 \times 10^{-3}$ /day (95% CI:  $2.10 \times 10^{-3}$  -  $3.14 \times 10^{-3}$ ), three-fold higher than the simulated value of  $7.66 \times 10^{-4}$  /day for lytically infected B cells<sup>310</sup> and 0.6 times higher than the simulated value of  $3.83 \times 10^{-4}$ /day for latently infected B cells, the only other CTL killing rates reported for EBV. Whilst the CTL killing rate for various viruses are available, many were quantified in mice<sup>349</sup> and those quantified in humans were variable depending on the method of quantification and model, for example, 1.6/day for HTLV-1<sup>350</sup>, 0.1- 9.8/day for HIV<sup>351</sup> and 0.1/day for CMV<sup>301</sup>, which made comparison, and therefore the interpretation of this result, difficult. Similarly, the value of  $3.2 \times 10^{-6}$  cells/day (95% CI:  $3.12 \times$

$10^{-6}$  -  $3.81 \times 10^{-6}$ ) estimated by the model for the CTL proliferation rate,  $r$ , was a derivation of the simulated value of  $3.25 \times 10^{-5}$  cells/day, which served as its initial estimate<sup>310</sup>. For the final CTL parameter, the CTL death rate,  $d$ , the model estimate of  $1.23 \times 10^{-4}$  cells/day (95% CI:  $1.08 \times 10^{-4}$  -  $1.25 \times 10^{-4}$ ), was more than 75-fold lower than a previously reported estimate of  $9.5 \times 10^{-3318,352}$  and significantly lower than the simulated value of  $6.46 \times 10^{-2310}$ . In addition, the derived half-life for EBV-specific CTLs of 15 years is most likely not biologically plausible for a paediatric cohort, given that most patients were less than 15 years old and would be experiencing EBV reactivation event post-HSCT as a primary infection, decreasing the likelihood of such a long-lived EBV-specific CTL pool.

The usefulness and applicability of a mathematical modelling approach to quantify the dynamics of EBV reactivation in this patient cohort has been demonstrated, but there are several limitations to be noted. The small sample sizes of 56 patients for the Cox-PH model and 30 patients for the viral dynamic model were characteristic of the study being retrospective and based at a single centre as well as the outcome of interest, EBV reactivation in children post-HSCT, being uncommon. Nevertheless, other authors have also conducted multivariable analysis on data from a comparable number or fewer patients in the context of EBV reactivation<sup>218,353,354</sup>. In addition, whilst the dataset represented a typical HSCT cohort, there were no patients who underwent HSCT using cord blood. The pattern of EBV reactivation for such patients may differ considerably to patients transplanted using PBSCs or BM, as their T cell reconstitution has been reported to be much faster, attributed to CBT patients receiving ATG-free pre-HSCT conditioning regimens and being of younger age at HSCT<sup>62,97,106</sup>. Regarding the viral dynamic model, the lack of previous NLME models of EBV reactivation post-HSCT greatly limited our ability to contextualise and interpret the results of the estimated parameter values, relying heavily on simulated values. Some estimates appeared more biologically plausible than others, and several parameters were estimated with high standard error and between-subject variability, in particular for the CTL-related parameters. This may be explained in part by the current lack of covariate model. Given the numerous covariates that can potentially contribute to the risk of EBV reactivation post-HSCT, the development of the Cox-PH model served as a preliminary evaluation of covariates<sup>355</sup>. The covariate-model building process for the viral dynamic model should now be informed by the identification of pre-HSCT ATG and EBV seropositivity of the recipient as significant covariates from the Cox-PH model. These covariates should be graphically evaluated to determine their relationship with EBV VL and clinical outcome<sup>339</sup> thereby justifying their incorporation into the base structural model of the NLME model to help explain the variability seen in the EBV VL trajectories of individual patients. Following further refinement of the model as outlined above, model-based simulations can be performed to demonstrate the effect of various rituximab dosing regimens on the trajectories of CD19<sup>+</sup> cells and EBV VL. This would reveal the true prognostic value of this EBV viral dynamic model in terms of its ability to inform rituximab dosing to improve clinical outcomes for post-HSCT patients with

EBV reactivation.

## Chapter 5

# Rituximab Biosimilar Pharmacodynamics in Rheumatology

### 5.1 Introduction

#### 5.1.1 Biosimilars

A biosimilar is defined as a biological product that is highly similar to and has no clinically meaningful differences from an existing approved ‘reference’ product<sup>226</sup>. With the help of PKPD studies, purity, chemical identity and bioactivity are assessed to ensure safety, efficacy and quality. To support biosimilar development, additional studies deemed appropriate such as clinical immunogenicity may also be performed<sup>226</sup>. After the patent for a reference product expires, exclusivity is lost, allowing generic drugs, and biosimilar drugs, to be marketed. While both are cheaper than the brand-name reference drug, generic drugs are chemically identical to the reference whereas biosimilars are highly similar. The first biosimilar drugs to be approved were filgrastim-sndz by the FDA in 2015, a granulocyte colony-stimulating factor agent<sup>356</sup>, and somatropin by the EMA in 2006, growth hormone<sup>357</sup>. Following the approval of biosimilars, the act of switching refers to the prescriber exchanging one medicine for another, e.g. a biosimilar product for the reference product, and vice versa, with the same therapeutic intent<sup>358</sup>. Such switching studies were recently reviewed by Barbier *et al* to assess the impact of switching on efficacy, safety and immunogenicity

outcomes for a range of biosimilars across various therapeutic areas<sup>359</sup>. In addition to biosimilars, there are interchangeable products, which satisfy regulatory requirements for biosimilars as well as additional requirements<sup>360</sup>. Whilst biosimilars bring significant benefits such as improved patient access, increased treatment options and lower healthcare costs, challenges in their adoption into clinical practice include reluctance of patients and healthcare providers, lack of financial incentives for healthcare providers and regulatory policies<sup>225,361</sup>.

### 5.1.2 Rituximab Biosimilars

Following the expiration of rituximab's patent in 2013 and 2016 in Europe and the United States respectively, biosimilars of rituximab have emerged in clinical use<sup>225</sup>. The current licensure for rituximab biosimilars has been summarised in Table 5.1. To date, there are four licensed rituximab biosimilars approved for all indications that the reference is licensed for.

Table 5.1: Current licensure for rituximab biosimilars. EMA, European Medicines Agency; FDA, Food and Drug Administration. NHL, Non-Hodgkin's B cell lymphoma; CLL, Chronic lymphocytic leukaemia; RA, Rheumatoid arthritis; MPA, Microscopic polyangitis; GPA, Granulomatosis with polyangitis; PV, Pemphigus vulgaris.

Name	Manufacturer	FDA Approval	EMA Approval	Population	Indications
Truxima	Celltrion Healthcare	2018	2017	Adult, Paediatric	NHL, CLL, RA, MPA, GPA, PV
Rixathon	Sandoz GmbH	Pending	2017	Adult, Paediatric	NHL, CLL, RA, MPA, GPA, PV
Ruxience	Pfizer Europe	2019	2020	Adult, Paediatric	NHL, CLL, RA, MPA, GPA, PV
Riabni	Amgen Inc	2020	Pending	Adult, Paediatric	NHL, CLL, RA, MPA, GPA

At GOSH, the rituximab biosimilar Truxima was introduced in October 2017. Regarding the rollout

of rituximab biosimilars, Cheesman gave an insight into the strategies taken to achieve complete adoption at a haematology department of a major tertiary hospital<sup>362</sup>. As the uptake of rituximab biosimilars increases, clinical studies have been increasingly conducted on their use in recent years, including randomised controlled trials, switching studies, real-world evidence studies and PKPD studies.

For the indication of rheumatoid arthritis, several switching studies have been performed in adult patients comparing safety and efficacy of biosimilars Truxima and Rixathon to reference rituximab<sup>363–365</sup>. In terms of their design, these studies consisted of a maintenance group, who received either reference or biosimilar from the start of treatment, and a switch group, who were switched from reference to biosimilar. No clinically meaningful differences were reported with regards to safety, efficacy, PD and immunogenicity, with a range of endpoints investigated including percentage of anti-drug antibodies, European League Against Rheumatism (EULAR) response<sup>363</sup>, Disease Activity Score using 28 joints (DAS28)<sup>364</sup> and hypersensitivity reactions<sup>365</sup>. In CLL and NHL patients, Urru *et al* studied two switch groups, from one biosimilar to another biosimilar (either Truxima or Rixathon) or to either reference or biosimilar different to that received before the study, and a no-switch group, with comparable endpoints observed in terms of adverse events<sup>366</sup>. In addition, Cohen *et al* investigated patients who received Ruxience with or without switch from reference<sup>367</sup> whilst the biosimilar Riabni was shown to be PKPD equivalent to reference in patients with moderate to severe arthritis in work by Burmester *et al*<sup>368</sup>.

Another major contribution to the biosimilars literature is that from real-world evidence studies<sup>361</sup>. Leveraging electronic patient health record data, Otremba *et al* described growing administration of rituximab biosimilars Rixathon and Truxima for extrapolated oncology indications NHL and CLL in Germany<sup>369</sup>. In the context of rheumatoid arthritis, Melville *et al* conducted a single-centre observational study to assess the effects of a treatment switch from reference to Truxima<sup>370</sup>. The authors additionally explored predictive factors for biosimilar discontinuation post-switch, which was mainly attributed to loss of effectiveness, adverse events, contraindication and patient choice. Alongside rituximab biosimilars approved by the EMA and FDA, other national health authorities have also granted licences. For example, HLX01, the first rituximab biosimilar approved in China by the National Medical Products Administration, was evaluated against reference in a study by Deng *et al* for B-cell lymphoma<sup>371</sup>. In addition, Riva *et al* investigated the biosimilar Novex licensed by the Argentinean Health Authority against reference rituximab in paediatric patients with complex diseases<sup>372</sup>. This observational single-centre study was one of the few paediatric studies of rituximab biosimilars. Furthermore, approved in India in 2007, the activity of the biosimilar Reditux against reference was investigated by Roy *et al* in a retrospective study in B-cell lymphoma patients, with no significant differences reported in terms of toxicity and clinical outcomes<sup>373</sup>.

Some of the more recent randomised controlled trials of rituximab biosimilars have compared their

safety, efficacy and PK with reference rituximab for follicular lymphoma. Rixathon and Truxima combined with a cyclophosphamide, doxorubicin, vincristine and prednisolone (CHOP) regimen was compared to reference combined with a CHOP regimen in Jurczak *et al* and Kim *et al* respectively<sup>374,375</sup>. Both studies reported equivalence of overall response and PK as well as comparable clinical outcomes. In Ogura *et al*, patients were randomly assigned to monotherapy with Truxima or reference, with therapeutic equivalence achieved between both treatment arms<sup>376</sup>. The PK of a candidate rituximab biosimilar, IBI301, was compared against reference in treatment for CD20<sup>+</sup> B cell lymphoma patients in Jiang *et al*, and was shown to be bioequivalent, with comparable PD, safety, immunogenicity profiles<sup>377</sup>. The same biosimilar was later administered in combination with a CHOP regimen for a similar patient cohort, compared against reference plus a CHOP regimen, and demonstrated non-inferior safety and efficacy<sup>378</sup>. Similarly, Reditux, was tested in combination with a CHOP regimen by Menon *et al*, who performed non-compartmental analysis to calculate PK parameters<sup>379</sup>.

To the best of the author's knowledge, two population PK models of rituximab biosimilars to date have been published in adult patients with B cell lymphoma<sup>380,381</sup> and none for paediatric patients.

### 5.1.3 Aim

This project aimed to develop a mechanistic NLME model to quantify the pharmacodynamics of a rituximab biosimilar on CD19<sup>+</sup> cell reconstitution in children with rheumatological conditions.

### 5.1.4 Objectives

- Clean patient electronic data of retrospective CD19<sup>+</sup> cell counts and rituximab biosimilar dosing
- Modify Chapter 3 rituximab K-PD model for clinical setting of rheumatology indications
- Evaluate model by performing diagnostic checks to compare model-predicted and observed data

## 5.2 Methods

### 5.2.1 Data

Using the Epic Electronic Health Record system, retrospective electronic data from routine clinical practice were collected from paediatric patients who had CD19<sup>+</sup> cell counts and drug administrations



at GOSH in the period 19/04/2019 to 14/01/2021. A series of inclusion criteria were implemented to identify study patients, as shown in the flow diagram in Figure 5.1, namely that patients had:

- Drug administrations of rituximab or rituximab biosimilars for rheumatology diagnoses
- A minimum of 2 CD19<sup>+</sup> cell counts each
- Not received fludarabine post-HSCT after receiving rituximab or rituximab biosimilars
- Had their baseline CD19<sup>+</sup> cell count  $\leq 7$  days before the first dose of rituximab or rituximab biosimilars

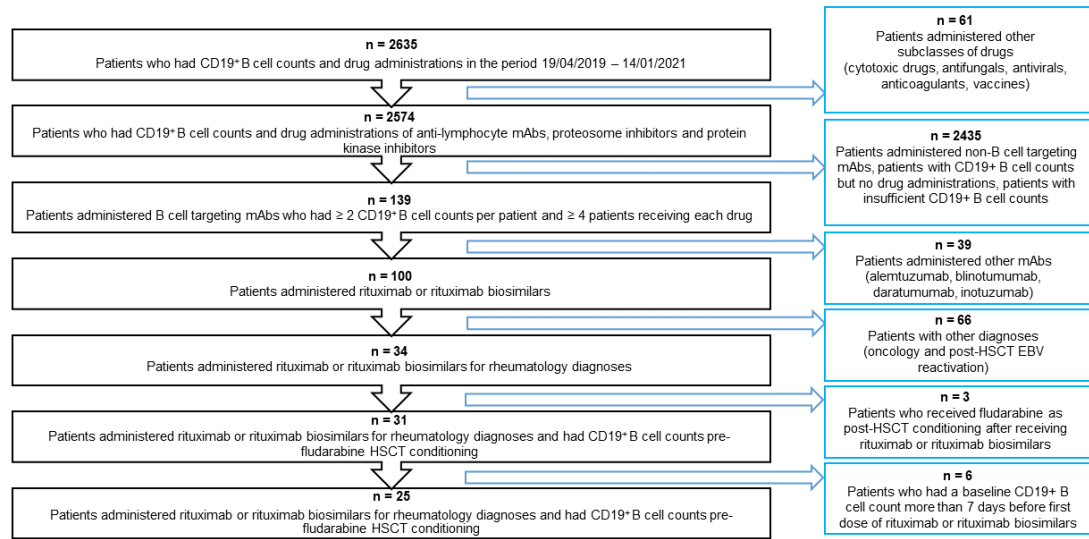


Figure 5.1: Flow diagram of study patients. EBV, Epstein-Barr virus; HSCT, Haematopoietic stem cell transplant; mAb, Monoclonal antibody.

The model-building dataset comprised CD19<sup>+</sup> cell counts, measured in  $10^6$  cells/L of blood, from 25 children. Data collected included demographic variables as well as measurements of immune cell subsets obtained by immunophenotyping using flow cytometry. Regarding sensitivity of the assay to detect lymphocytes, 10,000 events were targeted in the lymphocyte gate.

## 5.2.2 Rituximab and Biosimilar Administration

Patients were administered rituximab and the rituximab biosimilar, Truxima according to institutional protocols. The following formulations were used: MabThera 100mg/10mL concentrate for solution for infusion, MabThera 500mg/50mL concentrate for solution for infusion, Truxima 100mg/10mL concentrate for solution for infusion and Truxima 500mg/50mL concentrate for solution for infusion. Administration was via intravenous infusion, with a single dose constituting 375mg/m<sup>2</sup>. The dosing regimen varied depending on the rheumatological indication being treated, with up to four doses administered, and dosing frequencies included once only, every 48 hours, every 7 days and every 14 days.

## 5.2.3 Model

The mechanistic K-PD model developed in Chapter 3 to quantify rituximab PD in post-HSCT patients was used as the starting point. To ensure that the model would be able to describe CD19<sup>+</sup> cell reconstitution in non-HSCT rheumatology patients, the HSCT-specific parameters,  $\gamma$  and  $T50$  were removed. In addition, the covariate model was omitted as it was constructed using HSCT-specific covariates such as donor, conditioning regimen and HSC source, which were not applicable for the rheumatology patient cohort. Therefore, the equations for the structural model of the rituximab and rituximab biosimilars K-PD model was as follows.

$$\frac{dA_1}{dt} = -k_e \cdot (A_1), \quad (5.1)$$

$$\frac{dA_2}{dt} = \lambda - \mu \cdot \left( 1 + \frac{E_{max} \cdot A_1}{ED_{50} + A_1} \right) \cdot A_2 \quad (5.2)$$

The model-building assumptions made for rituximab were also made for the rituximab biosimilar; that none was present in the dosing compartment on day zero, that its elimination followed first-order kinetics and that it increased  $\mu$ .

## 5.3 Results

### 5.3.1 Patient Characteristics

The model was constructed using 139 measurements of CD19<sup>+</sup> cell counts from 25 children (median age, 12.8 years; range, 1.7 - 17.8 years). All patients received the rituximab biosimilar Truxima,

and four patients also received reference in addition to Truxima. Over a third of patients had a diagnosis of systemic lupus erythematosus. The raw data used for model-building is shown in Figure 5.2, and patient characteristics are summarised in Table 5.2.

Table 5.2: Patient characteristics for model-building dataset for rituximab biosimilars model. All patients received rituximab biosimilar. \* denotes 4 patients who received reference rituximab as well as rituximab biosimilar.

	Total Patients ( $n = 25$ )
<b>Age (years), median (range)</b>	12.8 (1.7 - 17.8)
<b>Diagnosis, <math>n</math> (%)</b>	
Juvenile arthritis	3 (12)
Arteritis	3 (12)
Localised scleroderma	1 (4)
Osteoporosis	1 (4)
Raynaud's syndrome	1 (4)
Spondyloepiphyseal dysplasia	1 (4)
Systemic lupus erythematosus	9 (36)
Granulomatosis with polyangitis	2 (8)
Renal osteodystrophy	1 (4)
Osteochondrodysplasia	1 (4)
Juvenile dermatomyositis	2 (8)
<b>CD19<sup>+</sup> cell count (<math>10^6</math>/L)</b>	10 (10 - 1150)
<b>Baseline CD19<sup>+</sup> cell count (<math>10^6</math>/L)</b>	330 (10 - 1150)
<b>Rituximab Formulation, <math>n</math> (%)</b>	
Reference MabThera	4* (16)
Biosimilar Truxima	25 (100)
<b>Rituximab dose (mg), median (range)</b>	1000 (165 - 1000)

### 5.3.2 Model Fitting

The two compartment turnover model was fitted to untransformed CD19<sup>+</sup> cell counts using the Laplacian conditional estimation with interaction algorithm in NONMEM version 7.4.3, with the ADVAN13 subroutine. The initial condition of the B cell compartment was set to  $5 \times 10^6$  cells/L (half of the LLOQ) on day zero. A proportion of the dataset were BLQ ( $n = 98$ , 70.5%) and these

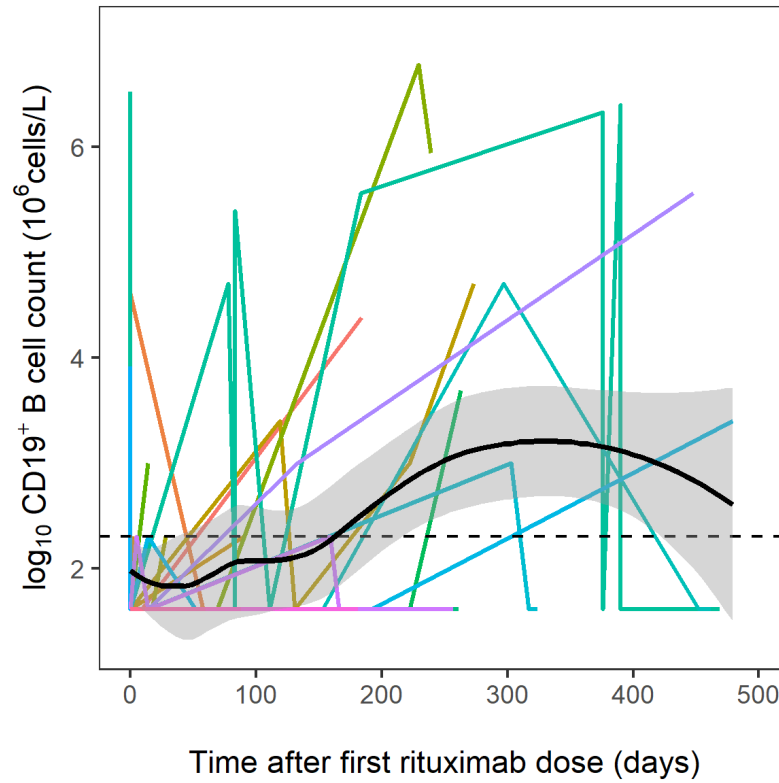


Figure 5.2: Raw data used for model-building ( $n = 25$ ). Each coloured line is an individual patient and the black dotted line represents the LLOQ of the assay used to measure  $\text{CD19}^+$  cell counts ( $10 \times 10^6$  cells/L). The thick black line is the local regression curve, and the grey shaded area is the 95% confidence interval.

observations were handled using the M3 method. A combined additive and proportional model best described the residual error.

### 5.3.3 Parameter Estimates

The parameter values estimated from the model-building dataset have been summarised in Table 5.3. The setpoint parameter was derived by dividing  $\lambda$  by  $\mu$  to provide a measure of the number of CD19<sup>+</sup> cells at steady-state in the absence of rituximab or rituximab biosimilar. Elimination half-lives for CD19<sup>+</sup> cells and rituximab biosimilar were calculated from  $\mu$  ( $t_{1/2} = \ln 2/\mu$ ) and  $k_e$  ( $t_{1/2} = \ln 2/k_e$ ) as 47.8 days and 6.08 days respectively. Regarding the rituximab biosimilar, the model estimated an apparent  $ED_{50}$  value of 1.04 mg, an apparent  $E_{max}$  value of 79.6 and an elimination rate of 0.114 per day.

Table 5.3: Estimated parameter values. Setpoint, number of CD19<sup>+</sup> cells at steady state in absence of rituximab biosimilar derived by  $\lambda$  divided by  $\mu$ ;  $\lambda$ , CD19<sup>+</sup> cell production rate constant;  $\mu$ , CD19<sup>+</sup> cell death rate constant;  $k_e$ , elimination rate constant of rituximab biosimilar;  $E_{max}$ , maximum killing effect of rituximab biosimilar on CD19<sup>+</sup> cells;  $ED_{50}$ , rituximab biosimilar dose producing 50% of maximum killing effect.

Parameter (units)	Estimate (%RSE)	%BSV (%RSE)	Shrinkage (%)	Bootstrap Median (95% CI)
Setpoint (x 10 <sup>6</sup> cells/L)	206.21	-	-	-
$\lambda$ (x 10 <sup>6</sup> cells/L)	2.99 (1.92)	88.83 (1.39)	55.0	2.58 (0.69 - 5.14)
$\mu$ (cells/day)	0.0145 (0.68)	111.36 (5.02)	49.9	0.0141 (0.00488 - 0.0414)
$k_e$ (/day)	0.114 (2.84)	248.80 (26.33)	55.0	0.0919 (0.0275 - 0.159)
$E_{max}$	79.6 (0.89)	-	-	72.2 (33.7 - 182.49)
$ED_{50}$ (mg)	1.04 (4.13)	-	-	0.907 (0.288 - 2.24)

### 5.3.4 Model Evaluation

The model was evaluated using goodness-of-fit plots (Figure 5.3) and a pcVPC (Figure 5.4). Model evaluation demonstrated a good fit of the observed data to the model-predicted data, with data clustering along the line of unity in the plots of the observed data against both the population predictions and individual predictions. In addition, the residual error was well described by the combined error model as shown in the plot of CWRES against time after dose/observation, which suggested a normal distribution with mean zero, with most of the data between  $\pm 2$  standard deviations of the mean and no pattern developing with time after dose/observation. For the plot of IWRES against individual predictions, there is a visible perturbation to an otherwise flat line at early timepoints due to the BLQ data. Lastly, the pcVPC illustrated consistency between the observed data and simulated data, with the observed percentiles falling within the 95% prediction intervals. In general, the prediction intervals were wide due to sparse data. As seen by the lower part of the pcVPC, the M3 method worked well in capturing the proportion of data that were BLQ.

## 5.4 Discussion

In this chapter, a two-compartment model was used to quantify the pharmacodynamics of the rituximab biosimilar Truxima in a paediatric population with rheumatological indications. Taking the rituximab model developed in Chapter 3 as a starting point, the HSCT-related parameters were removed to accommodate the clinical setting of rheumatology. As the administration of rituximab biosimilars is now commonplace, the clinical utility of such a model includes informing dose establishment and dose bioequivalence of rituximab biosimilars with the reference rituximab using the PD endpoint, CD19<sup>+</sup> cells, or using PK, if serum concentrations of rituximab biosimilars over time were available.

In general, the model estimated mean parameter values that were biologically plausible and with good precision. Of note, the estimate for  $\lambda$ ,  $2.99 \times 10^6$  cells/L (95%CI:  $0.69 \times 10^6$  -  $5.14 \times 10^6$ ), was 78% higher and 113% higher than estimated for the post-HSCT patients studied in Chapter 2 ( $1.68 \times 10^6$  cells/L; 95% CI,  $1.36 \times 10^6$  -  $2.05 \times 10^6$ ) and the post-HSCT patients who received rituximab studied in Chapter 3 ( $1.4 \times 10^6$  cells/L; 95% CI,  $0.852 \times 10^6$  -  $1.98 \times 10^6$ ) respectively. This resulted in a higher derived setpoint parameter value of  $206 \times 10^6$  cells/L in rheumatology patients, i.e. a higher baseline count of peripheral CD19<sup>+</sup> cells than in post-HSCT patients. For comparison, a reference value for the absolute CD19<sup>+</sup> cell count in healthy adolescents aged 11-18 years is 304 cells/ $\mu$ L (range, 226 - 370 cells/ $\mu$ L) therefore the derived setpoint value of  $206 \times 10^6$  cells/L in rheumatology patients was marginally lower than the lower end of the healthy range<sup>54</sup>. This aligned with the mechanism that HSCT confers an insult to the bone marrow thus decreasing

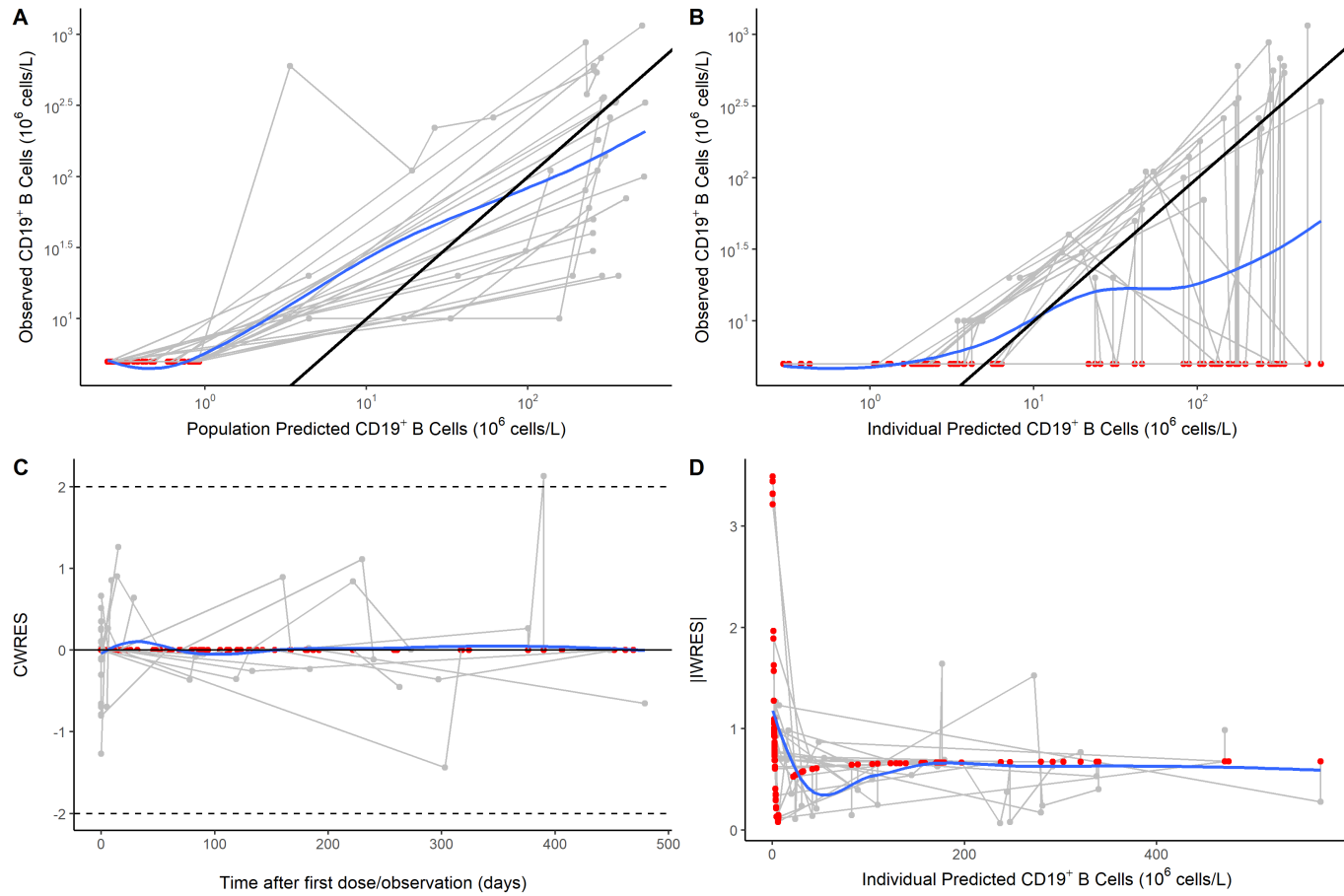


Figure 5.3: Goodness-of-fit plots. A) Observed CD19<sup>+</sup> cell counts vs Population Predicted CD19<sup>+</sup> cell counts. B) Observed CD19<sup>+</sup> cell counts vs Individual Predicted CD19<sup>+</sup> cell counts. C) CWRES vs Time after first dose/observation. D) |IWRES| vs Individual Predicted CD19<sup>+</sup> cell counts. Black lines are lines of unity, blue lines are the local regression curves and red datapoints are those that were BLQ.

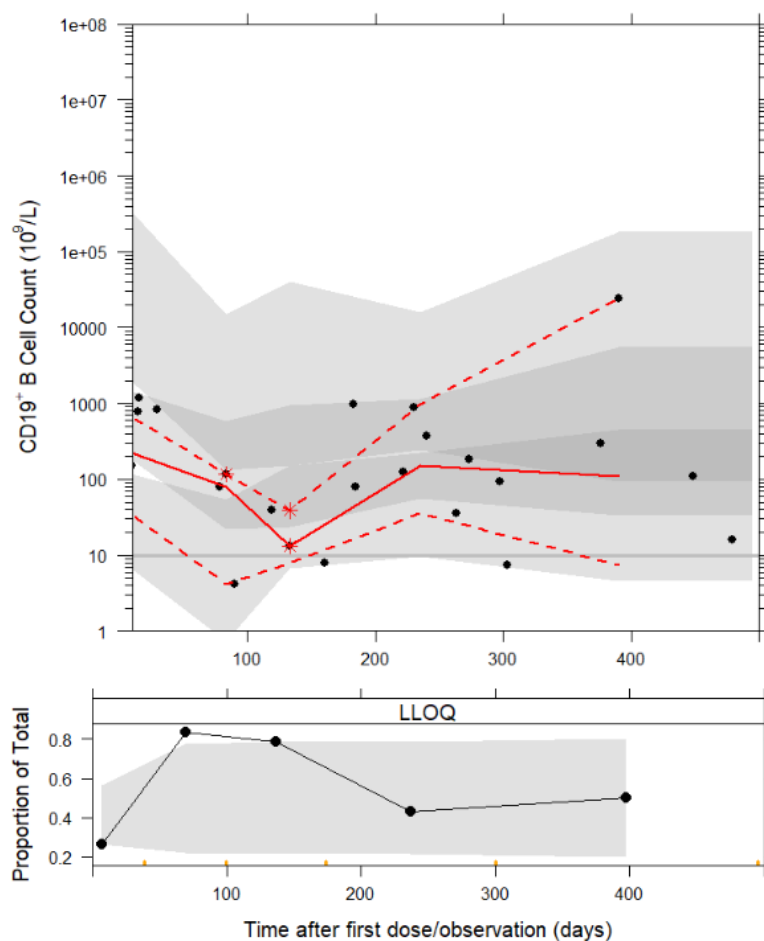


Figure 5.4: Prediction-corrected Visual predictive check of rituximab biosimilars model. Black dots are observed data and the solid red line is the observed median. The dotted red lines are the observed 2.5th, 50th and 97.5th percentiles and the grey shaded area are the 95% prediction intervals. The bottom panel shows the proportion of total data that were BLQ.



the capacity for CD19<sup>+</sup> cell proliferation in post-HSCT patients, resulting in a lower setpoint CD19<sup>+</sup> cell count compared to rheumatology patients. This suggests that the difference in derived setpoint values between the two patient groups could be due to biological or physiological differences.

The estimate for  $\mu$  was 0.0145 cells/day (95% CI: 0.00488 - 0.0414), comparable to 0.015 cells/day (95% CI: 0.013 - 0.018) estimated in the non-rituximab post-HSCT patients and 0.018 cells/day (95% CI: 0.00910 - 0.0252) estimated in rituximab post-HSCT patients. The continued similarity of  $\mu$ , despite a difference in patient cohort between post-HSCT and rheumatology patients and a difference in age range between mainly children in the post-HSCT cohorts and older adolescent patients in the rheumatology cohort, strongly supports the notion that mechanisms of B cell turnover remain robust following administration of B cell-depletive therapies such as rituximab and rituximab biosimilars, as well as after the insult of HSCT.

For  $k_e$ , the model estimated value of 0.114 per day was in line with the estimate of 0.109 per day by the Chapter 3 rituximab K-PD model but almost three-fold higher than estimated by Pan *et al* for rheumatology patients with a comparable median age of 13.2 years<sup>185</sup>. This difference could be linked to the marked difference in baseline CD19<sup>+</sup> cell count between the two study cohorts. Whereas the present study cohort had a median baseline CD19<sup>+</sup> cell count of  $330 \times 10^6$  cells/L, the study by Pan *et al* had a median baseline count of  $170 \times 10^6$  cells/L, nearly 50% lower. It could be hypothesised that the higher baseline count in patients in the present study may lead to saturation of the CD20<sup>+</sup> target-specific binding pathway, which could result in increased clearance via the much slower non-specific binding, causing a higher  $k_e$  estimate. Interestingly, the apparent half-life of 6.08 days is in the region of the  $10.9 \pm 8.6$  days reported in B cell lymphoma patients who received Reditux biosimilar<sup>379</sup>.

Regarding apparent  $E_{max}$ , this was estimated to be 79.6 (95% CI: 33.7 - 182.49), in line with that estimated by the rituximab K-PD model, 84.4, but more than two-fold higher than estimated by Pan *et al*, 35.2<sup>185</sup>. A possible explanation for this discrepancy could be the incorporation of the B cell maturation function in the biosimilars model, which scaled the  $\lambda$  and  $\mu$  parameters with respect to age before they were multiplied by the  $E_{max}$  model. In contrast, the effect of age was not accounted for in the model of Pan *et al*, which may elucidate the disagreement between the estimated and derived values for  $k_{in}$  and  $k_{out}$  in Pan *et al* of  $5.32 \times 10^6$  cells/L and 0.02 per day respectively and the estimated values for  $\lambda$  and  $\mu$  in the biosimilars model of  $2.99 \times 10^6$  cells/L and 0.0145 per day respectively.

The apparent  $ED_{50}$  parameter estimate of 1.04 mg (95% CI: 0.288 - 2.24) was in good agreement with the estimates of 0.81 mg by Pan *et al*<sup>185</sup> and 0.921 mg estimated by the rituximab K-PD model in Chapter 3. The corroboration of a low  $ED_{50}$  value from three models indeed suggests that a lower dose of rituximab and rituximab biosimilars can be as efficacious with regards to sufficient B cell suppression to control disease. It is important to note that both the rituximab K-PD model

and rituximab biosimilars K-PD model were fitted to B cell counts from peripheral blood only, therefore a higher rituximab dose may be required to achieve B cell depletion in solid tissue<sup>185</sup>.

While promising that the current biosimilar model could fit the data reasonably well, there are several improvements to be made to the model before it can be clinically useful. Firstly, a covariate model is yet to be developed to accompany the structural model. Clinically relevant covariates to be tested should include diagnosis, gender, and comedications such as methotrexate, hydrocortisone and mycophenolate mofetil, in line with previous work by Pan *et al*<sup>185</sup>. Secondly, to quantify the effect of formulation and to be able to inform bioequivalence, the model-building dataset for the biosimilar model can be merged with the historic dataset from the study by Pan *et al* to create a joint dataset representative of patients who received both the rituximab biosimilar and reference rituximab. Finally, simulations should be performed to test various dose regimens of the rituximab biosimilar to assess the resulting impact on patients' CD19<sup>+</sup> cell trajectories.

## Chapter 6

# Conclusions

Whilst they offer substantial therapeutic benefits, medical interventions such as HSCT and the administration of drugs affecting the immune response are also associated with high mortality and morbidity, largely due to adverse effects on the immune system. Therefore, it is necessary to better understand the recovery of the immune system after such insults in order to better inform the clinical management of patients. In particular, the paediatric population displays heterogeneity and variability in their recovery from these insults, highlighting the importance of considering development and maturation in delineating the patterns of recovery. In addition, the off-label administration of drugs affecting the immune response in paediatrics necessitates studies to optimise dosing regimens of these agents to improve treatment efficacy.

The first of the models constructed, detailed in Chapter 2, was a one-compartment mechanistic PD model to quantify  $CD19^+$  cell reconstitution following paediatric HSCT. With reference to previous modelling work done for  $CD4^+$  cell reconstitution following paediatric HSCT<sup>106</sup> and by considering relevant prior knowledge of immunobiology<sup>54,146</sup>, a B cell maturation function was developed to scale for age-related effects and a delay function was incorporated to account for the time delay between HSCT and bone marrow output. A PID diagnosis, receiving MAC and having a matched donor were identified as significant covariates impacting the time taken to recover half-maximal bone marrow output post-HSCT.

Building on this  $CD19^+$  cell model, an  $E_{max}$  model was then incorporated to create a two-compartment K-PD model in Chapter 3, to identify the pharmacodynamics of rituximab on B cells for the off-label indication of EBV reactivation post-HSCT. In general, greater effect sizes were estimated for the covariates in the rituximab K-PD model than for the  $CD19^+$  cell model in Chapter 2, highlighting the exacerbation of  $CD19^+$  cell reconstitution post-HSCT in the pres-

ence of rituximab. In Chapter 5, a simplified version of this rituximab K-PD model was used to quantify the pharmacodynamics of the Truxima rituximab biosimilar in children with rheumatological indications, demonstrating the application of the core model structure to a non-HSCT clinical setting.

In Chapter 4, the viral dynamics of EBV reactivation post-HSCT was investigated using several modelling approaches. Firstly, a multivariate Cox proportional hazards model identified pre-HSCT ATG administration and EBV seropositivity of the HSCT recipient as significant risk factors for an initial EBV reactivation event in the first 100 days post-HSCT<sup>1</sup>. In addition, sensitivity analysis of a previously reported mechanistic mathematical model of EBV viral kinetics found parameters related to latently infected memory B cells and CTLs to be key drivers of EBV VL<sup>320</sup>. This complex model proved challenging to fit to the clinical patient data therefore the rituximab K-PD model developed in Chapter 3 was integrated with a modified version of a published viral dynamic model for HIV<sup>324</sup> to construct a novel mechanistic five-compartment model of EBV viral dynamics and CD19<sup>+</sup> cell dynamics under the influence of rituximab.

## 6.1 Future Work

Efforts of future work should focus on further refinement of the models developed, performing model-based simulations and performing internal and/or external validation to assess predictive performance of the models on unseen patient data. This could be done using internal data from patients who underwent HSCT at GOSH after 2016 or using external data from patients transplanted at other HSCT centres.

Regarding the Chapter 2 CD19<sup>+</sup> cell model, a future direction is to leverage it as a Bayesian tool to predict individual patients' long-term CD19<sup>+</sup> cell reconstitution trajectories post-HSCT using CD19<sup>+</sup> cell counts from the early post-HSCT period as well as relevant covariate data. As post-HSCT patients undergo routine clinical monitoring, such a tool could be automatically updated as patients' CD19<sup>+</sup> cell counts are collected.

For the rituximab K-PD model, model-based simulations of various rituximab dosing regimens should be performed, e.g. ranging from a quarter of the usual dose, 94 mg/m<sup>2</sup> to double the dose, 750 mg/m<sup>2</sup>, to provide simulated profiles of CD19<sup>+</sup> cell suppression over time. Another direction of future work could be to convert the K-PD model into a full PK-PD model by integrating rituximab PK data from the literature. In terms of the EBV viral dynamic model, conducting model-based simulations would help identify the optimal rituximab dose at which the extent of CD19<sup>+</sup> cell depletion would be sufficient to suppress EBV VL to a sub-clinical level.

As for the rituximab biosimilar model, a covariate model should first be developed. Covariates tested

should include diagnosis, gender, and comedications in line with previous work by Pan *et al*<sup>185</sup>. Secondly, to quantify the effect of formulation and to be able to inform bioequivalence, the model-building dataset for the biosimilar model can be merged with the historic dataset from the study by Pan *et al* to create a joint dataset representative of patients who received both the rituximab biosimilar and reference rituximab. Finally, model-based simulations should be performed to test various dose regimens of the rituximab biosimilar to assess the resulting impact on patients' CD19<sup>+</sup> cell trajectories.

Collectively, the research presented in this thesis aimed to use mathematical modelling to investigate the reconstitution of B cells in children following various insults to the immune system. Four novel mechanistic NLME models of CD19<sup>+</sup> cell reconstitution encompassing immunology, viral infection and pharmacology were developed using retrospective real-world electronic health record data from children transplanted and treated at GOSH. New insights have been gained into the biological mechanisms governing B cell reconstitution and factors affecting it have been identified. This is the first time that B cell reconstitution has been quantified in children using NLME models, and there is great potential to continue this work to further expand our understanding of B cell reconstitution, and of immune reconstitution as a whole.

# References

1. Kania, S. P. *et al.* Epstein-Barr Virus Reactivation After Paediatric Haematopoietic Stem Cell Transplantation : Risk Factors and Sensitivity Analysis of Mathematical Model. *Frontiers in Immunology* **13**, 1–9 (2022).
2. Jagannathan-Bogdan, M. & Zon, L. I. Hematopoiesis. *Development (Cambridge)* **140**, 2463–2467 (2013).
3. Suo, C. *et al.* Mapping the developing human immune system across organs. *Science* **376**, (2022).
4. Schofield, R. The relationship between the spleen colony-forming cell and the haemopoietic stem cell. *Blood cells* **4**, 7–25 (1978).
5. Yahata, T. *et al.* Quiescent Human Hematopoietic Stem Cells in the Bone Marrow Niches Organize the Hierarchical Structure of Hematopoiesis. *Stem Cells* **26**, 3228–3236 (2008).
6. Yamamoto, V. *et al.* Hematopoietic Stem Cell Niche During Homeostasis, Malignancy, and Bone Marrow Transplantation. (2021).doi:10.3389/fcell.2021.621214
7. Kondo, M. *et al.* Biology of Hematopoietic Stem Cells and Progenitors: Implications for Clinical Application. *Annu. Rev. Immunol* **21**, 759–806 (2003).
8. Murphy, K. *Janeway’s Immunobiology: 9th Edition*. 1–277 (2017).
9. Chaplin, D. Overview of the Immune Response. *J Allergy Clin Immunol* **125**, 1–41 (2010).
10. Parkin, J. & Cohen, B. An Overview of the immune system. *Handbook of Clinical Neurology* **357**, 1777–1789 (2001).
11. Bertaina, A. & Andreani, M. Major histocompatibility complex and hematopoietic stem cell transplantation: Beyond the classical HLA polymorphism. *International Journal of Molecular Sciences* **19**, 1–14 (2018).

12. Alt, F. W. *et al.* Ordered rearrangement of immunoglobulin heavy chain variable region segments. *The EMBO Journal* **3**, 1209–1219 (1984).
13. Cooper, P., M. D. Delineation of the Thymic and Bursal Lymphoid Systems in the Chicken. *Nature* 143–146 (1965).
14. Wilkinson, M. G. L. & Rosser, E. C. B Cells as a Therapeutic Target in Paediatric Rheumatic Disease. *Frontiers in immunology* **10**, 214 (2019).
15. Nemazee, D. Mechanisms of central tolerance for B cells. *Nature Reviews Immunology* **17**, 281–294 (2017).
16. Klein, U. & Dalla-Favera, R. Germinal centres: Role in B-cell physiology and malignancy. *Nature Reviews Immunology* **8**, 22–33 (2008).
17. Crotty, S. T follicular helper cell differentiation, function, and roles in disease. **41**, 529–542 (2015).
18. Lebien, T. W. & Tedder, T. F. B lymphocytes: how they develop and function. *Blood* **112**, 1570–1580 (2008).
19. Stashenko, P., Nadler, L. E. E. M., Hardy, R. & Schlossman, S. F. Characterization of a human B lymphocyte-specific antigen. *The Journal of Immunology* **125**, 1678–1685 (1980).
20. Tedder, T. F. CD19: A promising B cell target for rheumatoid arthritis. *Nature Reviews Rheumatology* **5**, 572–577 (2009).
21. Wang, K., Wei, G. & Liu, D. CD19: a biomarker for B cell development, lymphoma diagnosis and therapy. *Experimental Hematology & Oncology* **1**, 1–7 (2012).
22. Avivi, I., Stroopinsky, D. & Katz, T. Anti-CD20 monoclonal antibodies: Beyond B-cells. *Blood Reviews* 217–223 (2013).doi:10.1016/j.blre.2013.07.002
23. Leandro, M. J. B-cell subpopulations in humans and their differential susceptibility to depletion with anti-CD20 monoclonal antibodies. *Arthritis Research & Therapy* **15**, 1–8 (2013).
24. National Institute for Health and Care Excellence Treatment summaries: Immune response. (2022).at <<https://bnf.nice.org.uk/treatment-summaries/immune-response/>>
25. National Institute for Health and Care Excellence. Treatment summaries: Rheumatic disease, suppressing drugs. (2022).at <<https://bnf.nice.org.uk/treatment-summaries/rheumatic-disease-suppressing-drugs/>>
26. Perelson, A. S., Kirschner, D. E. & De Boer, R. Dynamics of HIV infection of CD4+ T cells. *Mathematical Biosciences* **114**, 81–125 (1993).
27. Babcock, G. J., Decker, L. L., Volk, M. & Thorley-Lawson, D. A. EBV persistence in memory B cells in vivo. *Immunity* **9**, 395–404 (1998).

28. Dohms, J. E. & Saif, Y. M. Criteria for evaluating immunosuppression. *Avian diseases* **28**, 305–310 (1984).
29. Duarte, R. F. *et al.* Indications for haematopoietic stem cell transplantation for haematological diseases, solid tumours and immune disorders: current practice in Europe, 2019. *Bone Marrow Transplantation* **54**, 1525–1552 (2019).
30. Hatzimichael, E. & Tuthill, M. Hematopoietic stem cell transplantation. *Stem Cells and Cloning: Advances and Applications* **3**, 105–117 (2010).
31. Passweg, J. R. *et al.* Hematopoietic cell transplantation and cellular therapy survey of the EBMT: monitoring of activities and trends over 30 years. *Bone Marrow Transplantation* **56**, 1651–1664 (2021).
32. British Society of Blood and Marrow Transplantation and Cellular Therapy 2020 UK & ROI Transplant Activity. (2020).at <<https://bsbmtct.org/activity/2020/>>
33. Lapidot, T., Dar, A. & Kollet, O. How do stem cells find their way home? *Blood* **106**, 1901–1910 (2005).
34. Storek, J. *et al.* Reconstitution of the immune system after hematopoietic stem cell transplantation in humans. *Seminars in Immunopathology* **30**, 425–437 (2008).
35. Gyurkocza, B. & Sandmaier, B. M. Conditioning regimens for hematopoietic cell transplantation: One size does not fit all. *Blood* **124**, 344–353 (2014).
36. Pai, S. Y. Treatment of primary immunodeficiency with allogeneic transplant and gene therapy. *Hematology (United States)* **2019**, 457–465 (2019).
37. Hamilton, B. K. Current approaches to prevent and treat GVHD after allogeneic stem cell transplantation. *Hematology (United States)* **2018**, 228–235 (2018).
38. Worth, A. *et al.* Pre-emptive rituximab based on viraemia and T cell reconstitution: A highly effective strategy for the prevention of Epstein-Barr virus-associated lymphoproliferative disease following stem cell transplantation. *British Journal of Haematology* **155**, 377–385 (2011).
39. Ding, Y. *et al.* Epstein-Barr virus and cytomegalovirus reactivation after allogeneic hematopoietic cell transplantation in patients with non-Hodgkin lymphoma: the prevalence and impacts on outcomes: EBV and CMV reactivation post allo-HCT in NHL. *Annals of Hematology* **100**, 2773–2785 (2021).
40. Great Ormond Street Hospital for Children NHS Foundation Trust Bone Marrow Transplant clinical outcomes. (2021).at <<https://www.gosh.nhs.uk/conditions-and-treatments/clinical-outcomes/bone-marrow-transplant-clinical-outcomes/>>



41. Noel, D. *et al.* Does graft-versus-host disease influence the tempo of immunologic recovery after allogeneic human marrow transplantation? An observation on 56 long-term survivors. *Blood* **51**, 1087–1105 (1978).
42. Ratanatharathorn, B. V. *et al.* Prophylaxis After HLA-Identical Sibling Bone Marrow Transplantation. *Blood* **92**, 2303–2314 (1998).
43. MacMillan, M. L. *et al.* A refined risk score for acute graft-versus-host disease that predicts response to initial therapy, survival, and transplant-related mortality. *Biology of Blood and Marrow Transplantation* **21**, 761–767 (2015).
44. Merindol, N., Charrier, E., Duval, M. & Soudeyns, H. Complementary and contrasting roles of NK cells and T cells in pediatric umbilical cord blood transplantation. *Journal of Leukocyte Biology* **90**, 49–60 (2011).
45. Mehta, R. S. & Rezvani, K. Immune reconstitution post allogeneic transplant and the impact of immune recovery on the risk of infection. *Virulence* **7**, 901–916 (2016).
46. Fukuda, T. *et al.* Risks and outcomes of invasive fungal infections in recipients of allogeneic hematopoietic stem cell transplants after nonmyeloablative conditioning. (2003).doi:10.1182/blood-2003-02-0456
47. Rolling, T. *et al.* Haematopoietic cell transplantation outcomes are linked to intestinal mycobiota dynamics and an expansion of *Candida parapsilosis* complex species. *Nature Microbiology* **6**, 1505–1515 (2021).
48. Mikulska, M. *et al.* Blood Stream Infections in Allogeneic Hematopoietic Stem Cell Transplant Recipients: Reemergence of Gram-Negative Rods and Increasing Antibiotic Resistance. *Biology of Blood and Marrow Transplantation* **15**, 47–53 (2009).
49. Admiraal, R. *et al.* Viral reactivations and associated outcomes in the context of immune reconstitution after pediatric hematopoietic cell transplantation. *Journal of Allergy and Clinical Immunology* **140**, 1643–1650.e9 (2017).
50. Vaitkute, G. *et al.* Linking gastrointestinal microbiota and metabolome dynamics to clinical outcomes in paediatric haematopoietic stem cell transplantation. *Microbiome* **10**, (2022).
51. Leung, T. F. *et al.* Incidence, risk factors and outcome of varicella-zoster virus infection in children after haematopoietic stem cell transplantation. *Bone Marrow Transplantation* **25**, 167–172 (2000).
52. Blennow, O. *et al.* Varicella-Zoster Reactivation after Allogeneic Stem Cell Transplantation without Routine Prophylaxis-The Incidence Remains High. *Biology of Blood and Marrow Transplantation* **20**, 1646–1649 (2014).

53. Barnett, D., Walker, B., Landay, A. & Denny, T. N. CD4 immunophenotyping in HIV infection. **6**, (2008).
54. Morbach, H., Eichhorn, E. M., Liese, J. G. & Girschick, H. J. Reference values for B cell subpopulations from infancy to adulthood. *Clinical and Experimental Immunology* **162**, 271–279 (2010).
55. Duchamp, M. *et al.* B-cell subpopulations in children: National reference values. *Immunity Inflammation and Disease* **2**, 131–140 (2014).
56. Van Den Brink, M. R. M., Velardi, E. & Perales, M. A. Immune reconstitution following stem cell transplantation. *Hematology* **2015**, 215–219 (2015).
57. Naik, S. *et al.* Toward Functional Immune Monitoring in Allogeneic Stem Cell Transplant Recipients. *Biology of Blood and Marrow Transplantation* **26**, 911–919 (2020).
58. Comans-Bitter, W. M. *et al.* Immunophenotyping of blood lymphocytes in childhood: Reference values for lymphocyte subpopulations. *Journal of Pediatrics* **130**, 388–393 (1997).
59. Shearer, W. T. *et al.* Lymphocyte subsets in healthy children from birth through 18 years of age. *Journal of Allergy and Clinical Immunology* **112**, 973–980 (2003).
60. Huenecke, S. *et al.* Age-matched lymphocyte subpopulation reference values in childhood and adolescence: Application of exponential regression analysis. *European Journal of Haematology* **80**, 532–539 (2008).
61. K., K. *et al.* Immune reconstitution after haematopoietic cell transplantation in children: Immunophenotype analysis with regard to factors affecting the speed of recovery. *British Journal of Haematology* **118**, 74–89 (2002).
62. Rénard, C. *et al.* Lymphocyte subset reconstitution after unrelated cord blood or bone marrow transplantation in children. *British Journal of Haematology* **152**, 322–330 (2011).
63. Barker, C. I. S. *et al.* Pharmacokinetic/pharmacodynamic modelling approaches in paediatric infectious diseases and immunology. *Advanced Drug Delivery Reviews* **73**, 127–139 (2014).
64. Colburn, W. A. & Lee, J. W. *Biomarkers, Validation and Pharmacokinetic-Pharmacodynamic Modelling*. *Clin Pharmacokinet* **42**, 997–1022 (2003).
65. Wagner, J. A. Biomarkers: Principles, policies, and practice. *Clinical Pharmacology and Therapeutics* **86**, 3–7 (2009).
66. Heleen Bartelink, I. *et al.* Immune Reconstitution Kinetics as an Early Predictor for Mortality using Various Hematopoietic Stem Cell Sources in Children. *Biology of Blood and Marrow Transplantation* **19**, 305–313 (2013).

67. Kwon, M. *et al.* Early peripheral blood and T-cell chimerism dynamics after umbilical cord blood transplantation supported with haploidentical cells. *Bone Marrow Transplantation* **49**, 212–218 (2013).
68. Park, B. G. *et al.* Reconstitution of lymphocyte subpopulations after hematopoietic stem cell transplantation: Comparison of hematologic malignancies and donor types in event-free patients. *Leukemia Research* **39**, 1334–1341 (2015).
69. Chabannon, C. *et al.* Hematopoietic stem cell transplantation in its 60s: A platform for cellular therapies. *Science Translational Medicine* **10**, 1–11 (2018).
70. Khan, F., Agarwal, A. & Agrawal, S. Significance of chimerism in hematopoietic stem cell transplantation: New variations on an old theme. *Bone Marrow Transplantation* **34**, 1–12 (2004).
71. Faraci, M. *et al.* Evaluation of Chimerism Dynamics after Allogeneic Hematopoietic Stem Cell Transplantation in Children with Nonmalignant Diseases. *Biology of Blood and Marrow Transplantation* **24**, 1088–1093 (2018).
72. Kricke, S., Rao, K. & Adams, J. S. The significance of mixed chimaerism and cell lineage chimaerism monitoring in paediatric patients post haematopoietic stem cell transplant. (2022).doi:10.1111/bjh.18190
73. *Modelling and Applications in Mathematics Education*. (Springer, 2007).
74. Bonate, P. L. *Pharmacokinetic-Pharmacodynamic Modelling and Simulation*. 259–268 (2019).doi:10.1201/9780203743652-14
75. Mould, D. & Upton, R. Basic Concepts in Population Modeling, Simulation, and Model-Based Drug Development. (2012).doi:10.1038/psp.2012.4
76. Box, G. E. P. Science and Statistics. *Journal of the American Statistical Association* **71**, 791–799 (2021).
77. Box, G. E. P. *Robustness in the Strategy of Scientific Model Building*. 201–236 (Academic Press, Inc., 1979).doi:10.1016/b978-0-12-438150-6.50018-2
78. Leonelli, M. Simulation and Modelling to Understand Change. at <[https://bookdown.org/manuele%7B/\\_%7Dleonelli/SimBook/](https://bookdown.org/manuele%7B/_%7Dleonelli/SimBook/)>
79. Barrett, J. S., Fossler, M. J., Cadieu, K. D. & Gastonguay, M. R. Pharmacometrics: A multidisciplinary field to facilitate critical thinking in drug development and translational research settings. *Journal of Clinical Pharmacology* **48**, 632–649 (2008).

80. Kelly, L. E., Sinha, Y., Barker, C. I. S., Standing, J. F. & Offringa, M. Useful pharmacodynamic endpoints in children: Selection, measurement, and next steps. *Pediatric Research* **83**, 1095–1103 (2018).
81. IUPHAR, the I. U. of B. & Pharmacology, C. Clinical Pharmacology in Research, Teaching and Health Care Considerations by IUPHAR, the International Union of Basic and Clinical Pharmacology. *Basic and Clinical Pharmacology and Toxicology* **107**, 531–559 (2010).
82. Mager, D. E., Woo, S. & Jusko, W. J. *Scaling Pharmacodynamics from In Vitro and Pre-clinical Animal Studies to Humans. Drug Metab Pharmacokinet* 16–24 (2009).
83. Standing, J. F. Understanding and applying pharmacometric modelling and simulation in clinical practice and research. *British journal of clinical pharmacology* **83**, 247–254 (2017).
84. González-Sales, M., Nekka, F., Tanguay, M., Tremblay, P. O. & Li, J. Modelling the dose–response relationship: the fair share of pharmacokinetic and pharmacodynamic information. *British Journal of Clinical Pharmacology* **83**, 1240–1251 (2017).
85. Jacqmin, P. *et al.* Modelling response time profiles in the absence of drug concentrations: Definition and performance evaluation of the K-PD model. *Journal of Pharmacokinetics and Pharmacodynamics* **34**, 57–85 (2007).
86. Tod M Evaluation of drugs in pediatrics using K-PD model: perspectives. *Fundamental & Clinical Pharmacology* **22**, 589–594 (2008).
87. Perelson, A. Modelling Viral and Immune System Dynamics. *Nature Immunology* **2**, 28=36 (2002).
88. Mager, D. E., Jusko, W. J., Pharmacol, C. & Author, T. Development of Translational Pharmacokinetic-Pharmacodynamic Models. *Clin Pharmacol Ther* **83**, 909–912 (2008).
89. Upton, R. & Mould, D. Basic Concepts in Population Modeling, Simulation, and Model-Based Drug Development: Part 3—Introduction to Pharmacodynamic Modeling Methods. *CPT Pharmacometrics Syst. Pharmacol* 1–16 (2014).doi:10.1038/psp.2013.71
90. Chan, P. L. S. & Holford, N. H. G. Drug Treatment Effects on Disease Progression. *Annu. Rev. Pharmacol. Toxicol* **41**, 625–659 (2001).
91. Mould, D. Model-Based Meta-Analysis; An Important Tool for Making Quantitative Decisions During Drug Development. *Clinical Pharmacology & Therapeutics* **92**, 283–286 (2012).
92. Holford, N. Clinical pharmacology = disease progression + drug action. *British Journal of Clinical Pharmacology* **79**, 18–27 (2015).
93. Meibohm, B. & Derendorf, H. Pharmacokinetic/pharmacodynamic studies in drug product development. *Journal of Pharmaceutical Sciences* **91**, 18–31 (2002).

94. Sheiner, L. Learning versus confirming in clinical drug development. *Clinical Pharmacology & Therapeutics* **61**, 275–291 (1997).
95. Bradburn, M. J., Clark, T. G., Love, S. B. & Altman, D. G. Survival Analysis Part II: Multivariate data analysis- An introduction to concepts and methods. *British Journal of Cancer* **89**, 431–436 (2003).
96. Kaplan, E.L; Meier, P. Nonparametric Estimation from Incomplete Observations. *Journal of the American Statistical Association* **53**, 457–481 (1958).
97. Chiesa, R. & Veys, P. Reduced-intensity conditioning for allogeneic stem cell transplant in primary immune deficiencies. *Expert Review of Clinical Immunology* **8**, 255–267 (2012).
98. Willemsen, L. *et al.* Impact of Serotherapy on Immune Reconstitution and Survival Outcomes After Stem Cell Transplantations in Children: Thymoglobulin Versus Alemtuzumab. *Biology of Blood and Marrow Transplantation* **21**, 473–482 (2015).
99. Niehues, T. *et al.* Factors affecting lymphocyte subset reconstitution after either related or unrelated cord blood transplantation in children - a Eurocord analysis. *British Journal of Haematology* **114**, 42–48 (2001).
100. Kobulnicky, D. J. *et al.* Leukemia & Lymphoma The influence of lymphoid reconstitution kinetics on clinical outcomes in allogeneic stem cell transplantation The influence of lymphoid reconstitution kinetics on clinical outcomes in allogeneic stem cell transplantation. *Leukaemia and Lymphoma* (2018).doi:10.1080/10428194.2018.1452216
101. Davies, G. R., Hope, W. & Khoo, S. Opinion: The pharmacometrics of infectious disease. *CPT: Pharmacometrics and Systems Pharmacology* **2**, 1–3 (2013).
102. Garrido, M., Berraondo, P. & Trocóniz, I. F. Commentary on Pharmacometrics for Immunotherapy. *CPT: Pharmacometrics and Systems Pharmacology* **6**, 8–10 (2017).
103. Canini, L. & Perelson, A. S. Viral kinetic modeling: State of the art. *Journal of Pharmacokinetics and Pharmacodynamics* **41**, 431–443 (2014).
104. McCune, J., Jacobson, P., Wiseman, A. & Militano, O. Optimizing drug therapy in pediatric stem cell transplantation: Focus on pharmacokinetics. *Bone Marrow Transplant* **50**, 165–172 (2015).
105. McCune, J. S. & Bemer, M. J. Pharmacokinetics, Pharmacodynamics and Pharmacogenomics of Immunosuppressants in Allogeneic Haematopoietic Cell Transplantation: Part I. *Clinical Pharmacokinetics* **55**, 525–550 (2016).
106. Hoare, R. L., Veys, P., Klein, N., Callard, R. & Standing, J. F. Predicting CD4 T-Cell Reconstitution Following Pediatric Hematopoietic Stem Cell Transplantation. *Clinical Pharmacology and Therapeutics* **102**, 349–357 (2017).

107. Chiesa, R. *et al.* Proposed therapeutic range of treosulfan in reduced toxicity pediatric allogeneic hematopoietic stem cell transplant conditioning: results from a prospective trial. *Clinical Pharmacology & Therapeutics* **0**, 1–10 (2019).
108. Sandgaard, K. S., Lewis, J., Adams, S., Klein, N. & Callard, R. Antiretroviral therapy increases thymic output in children with HIV. *Aids* **28**, 209–214 (2014).
109. Majekodunmi, A. O. *et al.* Modelling CD4 T cell recovery in hepatitis C and HIV Co-infected children receiving antiretroviral therapy. *Pediatric Infectious Disease Journal* **36**, e123–e129 (2016).
110. Lewis, J. *et al.* Thymic output and CD4 T-cell reconstitution in HIV-infected children on early and interrupted antiretroviral treatment: Evidence from the children with HIV early antiretroviral therapy trial. *Frontiers in Immunology* **8**, (2017).
111. Smith, A. M. Validated models of immune response to virus infection. *Current Opinion in Systems Biology* **12**, 46–52 (2018).
112. Bosch, M., Khan, F. M. & Storek, J. Immune reconstitution after hematopoietic cell transplantation. *Current Opinion in Hematology* **19**, 324–355 (2012).
113. Wiegering, V., Eyrich, M., Winkler, B. & Schlegel, P. G. Comparison of Immune Reconstitution after Allogeneic Versus Autologous Stem Cell Transplantation in 182 Pediatric Recipients. *Journal of Pediatric Hematology/Oncology* **41**, e302–e307 (2019).
114. Storek, J., Witherspoon, R. P., Webb, D. & Storb, R. Lack of B cell precursors in marrow transplant recipients with chronic graft-versus-host disease. *American Journal of Hematology* **52**, 82–89 (1996).
115. De Vries, E. *et al.* Reconstitution of lymphocyte subpopulations after paediatric bone marrow transplantation. *Bone Marrow Transplantation* **25**, 267–275 (2000).
116. Williams, K. M. & Gress, R. E. Immune reconstitution and implications for immunotherapy following haematopoietic stem cell transplantation. *Best Practice and Research: Clinical Haematology* **21**, 579–596 (2008).
117. Sims, G. P. *et al.* Identification and characterization of circulating human transitional B cells. *Blood* **105**, 4390–4398 (2005).
118. Marie-Cardine, A. *et al.* Transitional B cells in humans: Characterization and insight from B lymphocyte reconstitution after hematopoietic stem cell transplantation. *Clinical Immunology* **127**, 14–25 (2008).
119. Luning Prak, E. T., Ross, J., Sutter, J. & Sullivan, K. E. Age-related trends in pediatric B-cell subsets. *Pediatric and Developmental Pathology* **14**, 45–52 (2011).

120. Cuss, A. K. *et al.* Expansion of Functionally Immature Transitional B Cells Is Associated with Human-Immunodeficient States Characterized by Impaired Humoral Immunity. *The Journal of Immunology* **176**, 1506–1516 (2006).
121. D’Orsogna, L. J. *et al.* Allogeneic Hematopoietic Stem Cell Transplantation Recipients Have Defects of Both Switched and IgM Memory B Cells. *Biology of Blood and Marrow Transplantation* **15**, 795–803 (2009).
122. Abdel-Azim, H., Elshoury, A., Mahadeo, K. M., Parkman, R. & Kapoor, N. Humoral Immune Reconstitution Kinetics after Allogeneic Hematopoietic Stem Cell Transplantation in Children: A Maturation Block of IgM Memory B Cells May Lead to Impaired Antibody Immune Reconstitution. *Biology of Blood and Marrow Transplantation* **23**, 1437–1446 (2017).
123. Matsue, K., Lum, L. G., Witherspoon, R. P. & Storb, R. Proliferative and differentiative responses of B cells from human marrow graft recipients to T cell-derived factors. *Blood* **69**, 308–315 (1987).
124. Savage, W. J. *et al.* Lymphocyte reconstitution following non-myeloablative hematopoietic stem cell transplantation follows two patterns depending on age and donor/recipient chimerism. *Bone Marrow Transplantation* **28**, 463–471 (2001).
125. Maas, N. G. van der, Berghuis, D., Burg, M. van der & Lankester, A. C. B Cell Reconstitution and Influencing Factors After Hematopoietic Stem Cell Transplantation in Children. *Frontiers in immunology* **10**, 782 (2019).
126. Omazic, B. *et al.* Reconstitution of the Ig heavy chain CDR3 repertoire after allogeneic haematopoietic stem cell transplantation with myeloablative or reduced-intensity conditioning regimens. *Scandinavian Journal of Immunology* **61**, 72–81 (2005).
127. Scarselli, A. *et al.* Longitudinal Evaluation of Immune Reconstitution and B-cell Function After Hematopoietic Cell Transplantation for Primary Immunodeficiency. *Journal of Clinical Immunology* **35**, 373–383 (2015).
128. Bae, K. W., Kim, B. E., Koh, K. N., Im, H. J. & Seo, J. J. Factors influencing lymphocyte reconstitution after allogeneic hematopoietic stem cell transplantation in children. *Korean Journal of Hematology* **47**, 44–52 (2012).
129. Abrahamsen, I. W. *et al.* Immune reconstitution after allogeneic stem cell transplantation: The impact of stem cell source and graft-versus-host disease. *Haematologica* **90**, 86–93 (2005).
130. Charrier, E. *et al.* Reconstitution of maturing and regulatory lymphocyte subsets after cord blood and BMT in children. *Bone Marrow Transplantation* **48**, 376–382 (2013).

131. Sottini, A. *et al.* Simultaneous quantification of recent thymic T-cell and bone marrow B-cell emigrants in patients with primary immunodeficiency undergone to stem cell transplantation. *Clinical Immunology* **136**, 217–227 (2010).
132. Dongen, J. J. M. van *et al.* Design and standardization of PCR primers and protocols for detection of clonal immunoglobulin and T-cell receptor gene recombinations in suspect lymphoproliferations: Report of the BIOMED-2 concerted action BMH4-CT98-3936. *Leukemia* **17**, 2257–2317 (2003).
133. Van Zelm, M. C., Szczepański, T., Van Der Burg, M. & Van Dongen, J. J. M. Replication history of B lymphocytes reveals homeostatic proliferation and extensive antigen-induced B cell expansion. *Journal of Experimental Medicine* **204**, 645–655 (2007).
134. Driessen, G. J. *et al.* B-cell replication history and somatic hypermutation status identify distinct pathophysiologic backgrounds in common variable immunodeficiency. *Blood* **118**, 6814–6823 (2011).
135. Hazenberg, M. D. *et al.* T-cell receptor excision circle and T-cell dynamics after allogeneic stem cell transplantation are related to clinical events. *Blood* **99**, 3449–3453 (2002).
136. Bains, I., Thiebaut, R., Yates, A. J. & Callard, R. Quantifying Thymic Export: Combining Models of Naive T Cell Proliferation and TCR Excision Circle Dynamics Gives an Explicit Measure of Thymic Output. *The Journal of Immunology* **183**, 4329–4336 (2009).
137. Mensen, A. *et al.* Utilization of TREC and KREC quantification for the monitoring of early T- and B-cell neogenesis in adult patients after allogeneic hematopoietic stem cell transplantation. *Journal of Translational Medicine* **11**, 6–9 (2013).
138. Serana, F. *et al.* The Different Extent of B and T Cell Immune Reconstitution after Hematopoietic Stem Cell Transplantation and Enzyme Replacement Therapies in SCID Patients with Adenosine Deaminase Deficiency. *The Journal of Immunology* **185**, 7713–7722 (2010).
139. Lev, A. *et al.* The kinetics of early T and B cell immune recovery after bone marrow transplantation in RAG-2-deficient SCID patients. *PLoS ONE* **7**, (2012).
140. Verstegen, R. H. J. *et al.* Quantification of T-cell and B-cell replication history in aging, immunodeficiency, and newborn screening. *Frontiers in Immunology* **10**, (2019).
141. Jarduli-Maciel, L. R. *et al.* Allogeneic haematopoietic stem cell transplantation resets T- and B-cell compartments in sickle cell disease patients. *Clinical and Translational Immunology* **11**, (2022).
142. Savchenko, A. A. *et al.* TREC/KREC Levels and T and B Lymphocyte Subpopulations in COVID-19 Patients at Different Stages of the Disease. *Viruses* **14**, (2022).



143. Gerdes, J. *et al.* Cell cycle analysis of a cell proliferation-associated human nuclear antigen defined by the monoclonal antibody Ki-67. *Journal of Immunology* **133**, 1710–5 (1984).
144. Douek, D. C. *et al.* Evidence for Increased T Cell Turnover and Decreased Thymic Output in HIV Infection. *The Journal of Immunology* **167**, 6663–6668 (2001).
145. Hazenberg, M. D. *et al.* Establishment of the CD4+ T-cell pool in healthy children and untreated children infected with HIV-1. *Blood* **104**, 3513–3519 (2004).
146. Gilmour, K. *et al.* Naive B Cell Output in HIV-Infected and HIV-Uninfected Children. *AIDS Research and Human Retroviruses* **35**, 33–39 (2018).
147. Barker, C. I. S. *et al.* Pharmacokinetic studies in children: recommendations for practice and research. *Arch Dis Child* **103**, 695–702 (2018).
148. Research, F. C. for D. E. and *Guidance for Industry General Considerations for Pediatric Pharmacokinetic Studies for Drugs and Biological Products.* (2014).at <http://www.fda.gov/Drugs/GuidanceComplianceRegulatoryInformation/Guidances/default.htm> <http://scholar.google.com/scholar?hl=en{\&}btnG=Search{\&}q=intitle:Guidance+for+Industry+General+Co>
149. Samant, T. S., Mangal, N., Lukacova, V. & Schmidt, S. Quantitative clinical pharmacology for size and age scaling in pediatric drug development: A systematic review. *Journal of Clinical Pharmacology* **55**, 1207–1217 (2015).
150. Johnson, T. N. The problems in scaling adult drug doses to children. *Archives of Disease in Childhood* **93**, 207–211 (2008).
151. Leeder, J. S., Kearns, G. L., Spielberg, S. P. & Van Den Anker, J. Understanding the relative roles of pharmacogenetics and ontogeny in pediatric drug development and regulatory science. *Journal of Clinical Pharmacology* **50**, 1377–1387 (2010).
152. Al-Metwali, B. & Mulla, H. Personalised dosing of medicines for children. **69**, 514–524 (2017).
153. Neely, M., Bayard, D., Desai, A., Kovanda, L. & Edginton, A. Pharmacometric Modeling and Simulation Is Essential to Pediatric Clinical Pharmacology. *Journal of Clinical Pharmacology* **58**, S73–S85 (2018).
154. Mahmood, I. Dosing in children: A critical review of the pharmacokinetic allometric scaling and modelling approaches in paediatric drug development and clinical settings. *Clinical Pharmacokinetics* **53**, 327–346 (2014).
155. Anderson, B. J. & Holford, N. H. G. Mechanism-based concepts of size and maturity in pharmacokinetics. **48**, 303–332 (2008).
156. Mulla, H. *Understanding Developmental Pharmacodynamics Importance for Drug Development and Clinical Practice.*

157. Germovsek, E., Barker, C. I. S., Sharland, M. & Standing, J. F. Pharmacokinetic–Pharmacodynamic Modeling in Pediatric Drug Development, and the Importance of Standardized Scaling of Clearance. *Clinical Pharmacokinetics* **58**, 39–52 (2019).
158. Germovsek, E., Cheng, M. & Giragossian, C. Allometric scaling of therapeutic monoclonal antibodies in preclinical and clinical settings. *mAbs* **13**, 1–22 (2021).
159. Wiegel, F. W. & Perelson, A. S. Some scaling principles for the immune system. *Immunology and Cell Biology* **82**, 127–131 (2004).
160. Bains, I., Antia, R., Callard, R. & Yates, A. J. Quantifying the development of the peripheral naive CD4 T-cell pool in humans. (2009).doi:10.1182/blood-2008-10
161. Ette, E. I. & Williams, P. J. Population pharmacokinetics I: Background, concepts, and models. *Annals of Pharmacotherapy* **38**, 1702–1706 (2004).
162. Beal, S.L., Sheiner, L.B., Boeckmann, A.J. & Bauer, R. J. NONMEM 7.4 users guides. (1989).at <<https://nonmem.iconplc.com/%7B/#%7D/nonmem743/guides>>
163. Bauer, R. J. NONMEM Tutorial Part I: Description of Commands and Options, With Simple Examples of Population Analysis. *CPT: Pharmacometrics & Systems Pharmacology* **8**, 525–537 (2019).
164. Bauer, R. J. NONMEM Tutorial Part II : Estimation Methods and Advanced Examples . *CPT: Pharmacometrics & Systems Pharmacology* 538–556 (2019).doi:10.1002/psp4.12422
165. Lindbom, L., Pihlgren, P. & Jonsson, N. PsN-Toolkit - A collection of computer intensive statistical methods for non-linear mixed effect modeling using NONMEM. *Computer Methods and Programs in Biomedicine* **79**, 241–257 (2005).
166. Beal, S. L. Ways to fit a PK model with some data below the quantification limit. *Journal of Pharmacokinetics and Pharmacodynamics* **28**, 481–504 (2001).
167. MO Karlsson, R. S. Diagnosing Model Diagnostics. *Clinical Pharmacology & Therapeutics* **82**, 17–20 (2007).
168. Nguyen, T. H. T. *et al.* Model evaluation of continuous data pharmacometric models: Metrics and graphics. *CPT: Pharmacometrics and Systems Pharmacology* **6**, 87–109 (2017).
169. Holford, N. H. G. The Visual Predictive Check Superiority to Standard Diagnostic (Rorschach) Plots. In *PAGE. Abstracts of the annual meeting of the population approach group in europe. ISSN 1871-6032* PAGE 14 (2005) Abstr738 (2005).at <<http://www.page-meeting.org/?abstract=738>>
170. Bergstrand, M., Hooker, A. C., Wallin, J. E. & Karlsson, M. O. Prediction-corrected visual predictive checks for diagnosing nonlinear mixed-effects models. *AAPS Journal* **13**, 143–151 (2011).

171. Blanco, E. *et al.* Age-associated distribution of normal B-cell and plasma cell subsets in peripheral blood. *Journal of Allergy and Clinical Immunology* **141**, 2208–2219.e16 (2018).
172. Trepel, F. Number and Distribution of Lymphocytes in Man. A Critical Analysis. *Klinische Wochenschrift* **52**, 511–515 (1974).
173. R Core Team *R: A language and environment for statistical computing.* (R Foundation for Statistical Computing, Vienna, Austria, 2022).at <<https://www.R-project.org/>>
174. Wickham, H. *et al.* Welcome to the tidyverse. *J. Open Source Softw.* **4**, 1686 (2019).
175. Jonsson, E. N. & Karlsson, M. O. Xpose - An S-PLUS based population pharmacokinetic/pharmacodynamic model building aid for NONMEM. *Computer Methods and Programs in Biomedicine* **58**, 51–64 (1998).
176. Keizer, R. J., Karlsson, M. O. & Hooker, A. Modeling and simulation workbench for NONMEM: Tutorial on Pirana, PsN, and Xpose. *CPT: Pharmacometrics and Systems Pharmacology* **2**, 1–9 (2013).
177. Lindbom, L., Ribbing, J. & Jonsson, E. N. Perl-speaks-NONMEM ( PsN )—— a Perl module for NONMEM related programming. (2004).doi:10.1016/j.cmpb.2003.11.003
178. Macallan, D. C. *et al.* B-cell kinetics in humans: rapid turnover of peripheral blood memory cells. (2005).doi:10.1182/blood-2004-09
179. Defoiche, J. *et al.* Reduction of B cell turnover in chronic lymphocytic leukaemia. *British Journal of Haematology* **143**, 240–247 (2008).
180. Kaur, A. *et al.* Dynamics of T- and B-Lymphocyte Turnover in a Natural Host of Simian Immunodeficiency Virus. *Journal of Virology* **82**, 1084–1093 (2008).
181. De Boer, R. J., Mohri, H., Ho, D. D. & Perelson, A. S. Turnover Rates of B Cells, T Cells, and NK Cells in Simian Immunodeficiency Virus-Infected and Uninfected Rhesus Macaques. *The Journal of Immunology* **170**, 2479–2487 (2003).
182. Shahaf, G., Zisman-Rozen, S., Benhamou, D., Melamed, D. & Mehr, R. B cell development in the bone marrow is regulated by homeostatic feedback exerted by mature B cells. *Frontiers in Immunology* **7**, 1–13 (2016).
183. Asquith, B. *et al.* Quantifying lymphocyte kinetics in vivo using carboxyfluorescein diacetate succinimidyl ester (CFSE). *Proceedings of the Royal Society B: Biological Sciences* **273**, 1165–1171 (2006).
184. Fulcher, D. A. & Basten, A. B cell life span: A review. *Immunology and Cell Biology* **75**, 446–455 (1997).

185. Pan, S. *et al.* Pharmacodynamics of rituximab on B lymphocytes in paediatric patients with autoimmune diseases. *British Journal of Clinical Pharmacology* (2019).doi:10.1111/bcp.13970
186. Van Der Maas, N. G. *et al.* Modeling Influencing Factors in B-Cell Reconstitution After Hematopoietic Stem Cell Transplantation in Children. *Frontiers in Immunology* **12**, 1–8 (2021).
187. Nakatani, K. *et al.* Cord blood transplantation is associated with rapid B-cell neogenesis compared with BM transplantation. *Bone Marrow Transplantation* **49**, 1155–1161 (2014).
188. Booth, C. & Veys, P. T cell depletion in paediatric stem cell transplantation. *Clinical and Experimental Immunology* **172**, 139–147 (2013).
189. Li, Z., Richards, S., Surks, H. K., Jacobs, A. & Panzara, M. A. Clinical pharmacology of alemtuzumab, an anti-CD52 immunomodulator, in multiple sclerosis. *Clinical and Experimental Immunology* **194**, 295–314 (2018).
190. Ribbing, J. & Niclas Jonsson, E. Power, selection bias and predictive performance of the population pharmacokinetic covariate model. *Journal of Pharmacokinetics and Pharmacodynamics* **31**, 109–134 (2004).
191. Payne, H. *et al.* Comparison of Lymphocyte Subset Populations in Children From South Africa, US and Europe. *Frontiers in Pediatrics* **8**, 1–12 (2020).
192. Hill, D. L. *et al.* Immune system development varies according to age, location, and anemia in African children. *Science Translational Medicine* **12**, (2020).
193. Epstein, M. A., Achong, B. G. & Barr, Y. M. Virus Particles in Cultured Lymphoblasts from Burkitt's Lymphoma. *The Lancet* **283**, 702–703 (1964).
194. Henle, G, Henle, W, Diehl, V. Relation of burkitt's tumor-associated herpes-type virus to infectious mononucleosist. *Proceedings of the National Academy of Sciences* **59**, 94–101 (1968).
195. Hausen, H. zur *et al.* EBV DNA in Biopsies of Burkitt Tumours and Anaplastic Carcinomas of the Nasopharynx. *Nature* **228**, 1056–1058 (1970).
196. Ho, M. *et al.* The frequency of Epstein-Barr virus infection and associated lymphoproliferative syndrome after transplantation and its manifestations in children. *Transplantation* **45**, 719–727 (1988).
197. Green, M. & Michaels, M. G. Epstein-barr virus infection and posttransplant lymphoproliferative disorder. *American Journal of Transplantation* **13**, 41–54 (2013).
198. Cohen, J. Epstein-Barr Virus Infection. *The New England Journal of Medicine* **343**, 481–492 (2000).

199. Smatti, M. K. *et al.* Epstein-Barr Virus Epidemiology, Serology, and Genetic Variability of LMP-1 Oncogene Among Healthy Population: An Update. **8**, 1–16 (2018).
200. Baer, R. *et al.* DNA sequence and expression of the B95-8 Epstein-Barr virus genome. *Nature* **310**, 207–211 (1984).
201. Luftig, M. A. & Stanfield, B. A. Recent advances in understanding Epstein-Barr virus. *F1000Research* **6**, 1–10 (2017).
202. Odumade, O. A., Hogquist, K. A. & Balfour, H. H. Progress and problems in understanding and managing primary epstein-barr virus infections. *Clinical Microbiology Reviews* **24**, 193–209 (2011).
203. Dugan, J. P., Coleman, C. B. & Haverkos, B. Opportunities to target the life cycle of Epstein-Barr Virus (EBV) in EBV-associated lymphoproliferative disorders. *Frontiers in Oncology* **9**, 1–10 (2019).
204. Hislop, A. D., Taylor, G. S., Sauce, D. & Rickinson, A. B. Cellular responses to viral infection in humans: Lessons from Epstein-Barr virus. *Annual Review of Immunology* **25**, 587–617 (2007).
205. Cohen, J. *et al.* Increased incidence of EBV-related disease following paediatric stem cell transplantation with reduced-intensity conditioning. *British Journal of Haematology* **129**, 229–239 (2005).
206. Brunstein, C. G. *et al.* Marked increased risk of Epstein-Barr virus-related complications with the addition of antithymocyte globulin to a nonmyeloablative conditioning prior to unrelated umbilical cord blood transplantation. *Blood* **108**, 2874–2880 (2006).
207. Landgren, O. *et al.* Risk factors for lymphoproliferative disorders after allogeneic hematopoietic cell transplantation. *Blood* **113**, 4992–5001 (2009).
208. Heslop, H. E. How I treat EBV lymphoproliferation. *Blood* **114**, 4002–4008 (2009).
209. Solano, C. *et al.* Epstein-Barr virus DNA load kinetics analysis in allogeneic hematopoietic stem cell transplant recipients: Is it of any clinical usefulness? *Journal of Clinical Virology* **97**, 26–32 (2017).
210. Kimura, H. & Kwong, Y. L. EBV viral loads in diagnosis, monitoring, and response assessment. *Frontiers in Oncology* **9**, 4–9 (2019).
211. Fryer, J. F., Heath, A. B., Wilkinson, D. E. & Minor, P. D. A collaborative study to establish the 1st WHO International Standard for Epstein-Barr virus for nucleic acid amplification techniques. *Biologicals* **44**, 423–433 (2016).
212. Eisenberg, R. Update on rituximab. *Annals of the Rheumatic Diseases* **64**, 55–57 (2005).

- 213. Grillo-Lopez, A. *et al.* Rituximab The First Monoclonal Antibody Approved for the Treatment of Lymphoma. *Current Pharmaceutical Biotechnology* **1**, 1–9 (2000).
- 214. Jamois, C. *et al.* Rituximab pediatric drug development: Pharmacokinetic and pharmacodynamic modeling to inform regulatory approval for rituximab treatment in patients with granulomatosis with polyangiitis or microscopic polyangiitis. *Clinical and Translational Science* 2172–2183 (2022).doi:10.1111/cts.13351
- 215. Delate, T., Hansen, M. L., Gutierrez, A. C. & Le, K. N. Indications for rituximab use in an integrated health care delivery system. *Journal of Managed Care and Specialty Pharmacy* **26**, 832–838 (2020).
- 216. Sarsour, K. *et al.* Rituximab utilization for approved and off-label nononcology indications and patients’ experiences with the Patient Alert Card. *Pharmacology Research and Perspectives* **8**, 1–7 (2020).
- 217. Coppoletta, S. *et al.* Rituximab Treatment for Epstein-Barr Virus DNAemia after Alternative-Donor Hematopoietic Stem Cell Transplantation. *Biology of Blood and Marrow Transplantation* **17**, 901–907 (2011).
- 218. Fox, C. P. *et al.* EBV-associated post-transplant lymphoproliferative disorder following in vivo T-cell-depleted allogeneic transplantation: Clinical features, viral load correlates and prognostic factors in the rituximab era. *Bone Marrow Transplantation* **49**, 280–286 (2014).
- 219. Styczynski, J. *et al.* Management of Epstein-Barr Virus infections and post-transplant lymphoproliferative disorders in patients after allogeneic hematopoietic stem cell transplantation: Sixth European Conference on Infections in Leukemia (ECIL-6) guidelines. *European Hematology Association Haematologica* **101**, 803–811 (2016).
- 220. Kobayashi, S. *et al.* Pre-emptive rituximab for Epstein–Barr virus reactivation after haplo-hematopoietic stem cell transplantation. *Pediatrics International* **59**, 973–978 (2017).
- 221. Kalra, A. *et al.* Epstein-barr virus DNAemia monitoring for the management of post-transplant lymphoproliferative disorder. *Cytotherapy* **20**, 706–714 (2018).
- 222. Jain, T. *et al.* Single dose versus multiple doses of rituximab for preemptive therapy of Epstein–Barr virus reactivation after hematopoietic cell transplantation. *Leukemia and Lymphoma* **60**, 110–117 (2019).
- 223. Stocker, N. *et al.* Pre-emptive rituximab treatment for Epstein – Barr virus reactivation after allogeneic hematopoietic stem cell transplantation is a worthwhile strategy in high-risk recipients : a comparative study for immune recovery and clinical outcomes. *Bone Marrow Transplantation* doi:10.1038/s41409-019-0699-6

- 224. García-Cadenas, I. *et al.* Frequency, characteristics, and outcome of PTLT after allo-SCT: A multicenter study from the Spanish group of blood and marrow transplantation (GETH). *European Journal of Haematology* **102**, 465–471 (2019).
- 225. Greenwald, M., Tesser, J. & Sewell, K. L. Biosimilars Have Arrived: Rituximab. *Arthritis* **2018**, 1–6 (2018).
- 226. Food and Drug Administration Biosimilars and Interchangeable Products. (2017).at <<https://www.fda.gov/drugs/biosimilars/biosimilar-and-interchangeable-products%7B/#%7Dbiosimilar>>
- 227. Miranda-Hernandez, M. P. *et al.* Assessment of physicochemical properties of rituximab related to its immunomodulatory activity. *Journal of Immunology Research* **2015**, (2015).
- 228. Wang, W., Wang, E. Q. & Balthasar, J. P. Monoclonal antibody pharmacokinetics and pharmacodynamics. *Clinical Pharmacology and Therapeutics* **84**, 548–558 (2008).
- 229. Lobo, E. D., Hansen, R. J. & Balthasar, J. P. Antibody pharmacokinetics and pharmacodynamics. *Journal of Pharmaceutical Sciences* **93**, 2645–2668 (2004).
- 230. Ryman, J. T. & Meibohm, B. Pharmacokinetics of monoclonal antibodies. *CPT: Pharmacometrics and Systems Pharmacology* **6**, 576–588 (2017).
- 231. Ng, C. M., Bruno, R., Combs, D. & Davies, B. Population pharmacokinetics of rituximab (anti-CD20 monoclonal antibody) in rheumatoid arthritis patients during a phase II clinical trial. *Journal of Clinical Pharmacology* **45**, 792–801 (2005).
- 232. Müller, C. *et al.* The role of sex and weight on rituximab clearance and serum elimination half-life in elderly patients with DLBCL. *Blood* **119**, 3276–3284 (2012).
- 233. Ovacik, M. & Lin, K. Tutorial on Monoclonal Antibody Pharmacokinetics and Its Considerations in Early Development. *Clinical and Translational Science* **11**, 540–552 (2018).
- 234. Ternant, D. *et al.* Nonlinear pharmacokinetics of rituximab in non-Hodgkin lymphomas: A pilot study. *British Journal of Clinical Pharmacology* **85**, 2002–2010 (2019).
- 235. Bensalem, A. *et al.* Non-Linear Rituximab Pharmacokinetics and Complex Relationship between Rituximab Concentrations and Anti-Neutrophil Cytoplasmic Antibodies (ANCA) in ANCA-Associated Vasculitis: The RAVE Trial Revisited. *Clinical Pharmacokinetics* **59**, 519–530 (2020).
- 236. Ternant, D., Azzopardi, N., Raoul, W., Theodora, B.-A. & Paintaud, G. Influence of Antigen Mass on the Pharmacokinetics of Therapeutic Antibodies in Humans. *Clinical Pharmacokinetics* **2**, 169–187 (2019).

- 237. Dostalek, M., Gardner, I., Gurbaxani, B. M., Rose, R. H. & Chetty, M. *Pharmacokinetics, pharmacodynamics and physiologically-based pharmacokinetic modelling of monoclonal antibodies*. **52**, 83–124 (2013).
- 238. Keizer, R. J., Huitema, A. D. R., Schellens, J. H. M. & Beijnen, J. H. Clinical pharmacokinetics of therapeutic monoclonal antibodies. *Clinical Pharmacokinetics* **49**, 493–507 (2010).
- 239. Golay, J. *et al.* Lessons for the clinic from rituximab PK and PD. *mAbs* 826–837 (2013).doi:10.4161/mabs.26008
- 240. Gibiansky, E., Gibiansky, L., Chavanne, C., Frey, N. & Jamois, C. Population pharmacokinetic and exposure–response analyses of intravenous and subcutaneous rituximab in patients with chronic lymphocytic leukemia. *CPT: Pharmacometrics and Systems Pharmacology* **10**, 914–927 (2021).
- 241. Junghans, R. P. & Anderson, C. L. The protection receptor for IgG catabolism is the  $\beta$ 2-microglobulin-containing neonatal intestinal transport receptor. *Proceedings of the National Academy of Sciences of the United States of America* **93**, 5512–5516 (1996).
- 242. Bennett, J. L. *et al.* B lymphocytes in neuromyelitis optica. *Neurology: Neuroimmunology and NeuroInflammation* **2**, e104 (2015).
- 243. Maloney, D. G., Smith, B. & Rose, A. Rituximab: Mechanism of action and resistance. *Seminars in Oncology* **29**, 2–9 (2002).
- 244. Quartier, P. *et al.* Treatment of refractory autoimmune haemolytic anaemia with anti-CD20 (rituximab). *Infusionstherapie und Transfusionsmedizin* **28**, 31–32 (2001).
- 245. Shah, K., Cragg, M., Leandro, M. & Reddy, V. Anti-CD20 monoclonal antibodies in Systemic Lupus Erythematosus. *Biologicals* **69**, 1–14 (2021).
- 246. Castagnola, E. *et al.* Long-lasting Hypogammaglobulinemia Following Rituximab Administration for Epstein-Barr Virus-Related Post-Transplant Lymphoproliferative Disease Pre-emptive Therapy. *J Hematother Stem Cell Res* **104**, 2204–2206 (2003).
- 247. Makatsori, M. *et al.* Hypogammaglobulinaemia after rituximab treatment-incidence and outcomes. *Qjm* **107**, 821–828 (2014).
- 248. Small, T. *et al.* B-cell differentiation following autologous, conventional, or T-cell depleted bone marrow transplantation: a recapitulation of normal B-cell ontogeny. *Blood* **76**, 1647–1656 (1990).
- 249. Leandro, M. J., Cambridge, G., Ehrenstein, M. R. & Edwards, J. C. W. Reconstitution of peripheral blood B cells after depletion with rituximab in patients with rheumatoid arthritis. *Arthritis and Rheumatism* **54**, 613–620 (2006).



250. Das, G. *et al.* Rituximab before and during pregnancy. *Neurology - Neuroimmunology Neuroinflammation* **5**, e453 (2018).
251. Dai, H. I., Vugmeyster, Y. & Mangal, N. Characterizing Exposure–Response Relationship for Therapeutic Monoclonal Antibodies in Immuno-Oncology and Beyond: Challenges, Perspectives, and Prospects. *Clinical Pharmacology and Therapeutics* **108**, 1156–1170 (2020).
252. Kawakatsu, S. *et al.* Confounding factors in exposure–response analyses and mitigation strategies for monoclonal antibodies in oncology. *British Journal of Clinical Pharmacology* **87**, 2493–2501 (2021).
253. Barth, M. *et al.* Rituximab pharmacokinetics in children and adolescents with de novo intermediate and advanced mature B-cell lymphoma/ leukaemia: A Children’s Oncology Group (COG) report. *Br J Haematol* **162**, 678–683 (2013).
254. Chen, Y. *et al.* Population Pharmacokinetics of Rituximab in Pediatric Patients With Frequent-Relapsing or Steroid-Dependent Nephrotic Syndrome. *Frontiers in Pharmacology* **12**, 1–9 (2021).
255. Blasco, H., Chatelut, E., De Bretagne, I. B., Congy-Jolivet, N. & Le Guellec, C. Pharmacokinetics of rituximab associated with CHOP chemotherapy in B-cell non-Hodgkin lymphoma. *Fundamental and Clinical Pharmacology* **23**, 601–608 (2009).
256. Rozman, S., Grabnar, I., Novaković, S., Mrhar, A. & Jezeršek Novaković, B. Population pharmacokinetics of rituximab in patients with diffuse large B-cell lymphoma and association with clinical outcome. *British Journal of Clinical Pharmacology* **83**, 1782–1790 (2017).
257. Tout, M. *et al.* Rituximab exposure is influenced by baseline metabolic tumor volume and predicts outcome of DLBCL patients: A Lymphoma Study Association report. *Blood* **129**, 2616–2623 (2017).
258. Li, J. *et al.* Population pharmacokinetics of rituximab in patients with chronic lymphocytic leukemia. *Journal of Clinical Pharmacology* **52**, 1918–1926 (2012).
259. Li, L., Gardner, I., Dostalek, M. & Jamei, M. Simulation of monoclonal antibody pharmacokinetics in humans using a minimal physiologically based model. *AAPS Journal* **16**, 1097–1109 (2014).
260. Glassman, P. M. & Balthasar, J. P. Physiologically-based modeling to predict the clinical behavior of monoclonal antibodies directed against lymphocyte antigens. *mAbs* **9**, 297–306 (2017).
261. Sharkey, I. *et al.* Body surface area estimation in children using weight alone: application in paediatric oncology. *British Journal of Cancer* **85**, 23–28 (2001).

- 262. Holford, N. Pharmacodynamic principles and the time course of delayed and cumulative drug effects. *Translational and Clinical Pharmacology* **25**, 157–161 (2017).
- 263. Zarkhin, V. *et al.* A randomized, prospective trial of rituximab for acute rejection in pediatric renal transplantation. *American Journal of Transplantation* **8**, 2607–2617 (2008).
- 264. Delapierre, B. *et al.* Low dose Rituximab for pre-emptive treatment of Epstein Barr virus reactivation after allogeneic hematopoietic stem cell transplantation. *Current Research in Translational Medicine* (2019).doi:10.1016/j.retram.2019.03.001
- 265. Kim, B. K. *et al.* Successful Preemptive Therapy with single dose Rituximab for Epstein-Barr Virus Infection to Prevent Post-Transplant-Lymphoproliferative Disease after Pediatric Hematopoietic Stem Cell Transplantation. *Transplant Infectious Disease* 1–7 (2019).doi:10.1111/tid.13182
- 266. Wennmann, M. *et al.* A Retrospective Analysis of Rituximab Treatment for B Cell Depletion in Different Pediatric Indications. *Frontiers in Pediatrics* **9**, 1–8 (2021).
- 267. Schoergenhofer, C. *et al.* Single, very low rituximab doses in healthy volunteers - A pilot and a randomized trial: Implications for dosing and biosimilarity testing. *Scientific Reports* **8**, 1–8 (2018).
- 268. Berinstein, N. L. *et al.* Association of serum Rituximab (IDEC-C2B8) concentration and anti-tumor response in the treatment of recurrent low-grade or follicular non-Hodgkin's lymphoma. *Annals of Oncology* **9**, 995–1001 (1998).
- 269. Liu, S. *et al.* Rituximab Concentration Varies in Patients With Different Lymphoma Subtypes and Correlates With Clinical Outcome. *Frontiers in Pharmacology* **13**, (2022).
- 270. Starr, A., Kwon, D. H. & Kallakury, B. Epstein-Barr Virus-Positive CD20- and CD45-Negative Diffuse Large B-Cell Lymphoma: A Diagnostic Challenge. *International Journal of Surgical Pathology* **27**, 98–101 (2019).
- 271. Hiraga, J. *et al.* Down-regulation of CD20 expression in B-cell lymphoma cells after treatment with rituximab-containing combination chemotherapies: Its prevalence and clinical significance. *Blood* **113**, 4885–4893 (2009).
- 272. Schmitz, K., Brugger, W., Weiss, B., Kaiserling, E. & Kanz, L. Clonal Selection of CD20-Negative Non-Hodgkin's Lymphoma Cells After Treatment with Anti-CD20 Antibody Rituximab. *British Journal of Haematology* **106**, 571–572 (1999).
- 273. Kennedy, G. A. *et al.* Incidence and nature of CD20-negative relapses following rituximab therapy in aggressive B-cell non-Hodgkin's lymphoma: a retrospective review. *British Journal of Haematology* **119**, 412–416 (2002).

- 274. Jilani, I. *et al.* Transient down-modulation of CD20 by rituximab in patients with chronic lymphocytic leukemia. *Blood* **102**, 3514–3520 (2003).
- 275. Maeshima, A. M. *et al.* Histological and immunophenotypic changes in 59 cases of B-cell non-Hodgkin s lymphoma after rituximab therapy. *Cancer Sciences* **100**, 54–61 (2009).
- 276. Styles, C. T. *et al.* EBV epigenetically suppresses the B cell-to-plasma cell differentiation pathway while establishing long-term latency. *PLoS Biology* **15**, 1–30 (2017).
- 277. Mrozek-Gorska, P. *et al.* Epstein–Barr virus reprograms human B lymphocytes immediately in the prelatent phase of infection. *Proceedings of the National Academy of Sciences of the United States of America* **116**, 16046–16055 (2019).
- 278. Treon, S. P. *et al.* Tumor Cell Expression of CD59 Is Associated With Resistance to CD20 Serotherapy in Patients With B-Cell Malignancies. *Journal of Immunotherapy* **24**, 263–271 (2001).
- 279. Pavlasova, G. & Mraz, M. The regulation and function of CD20: An ‘enigma’ of B-cell biology and targeted therapy. *Haematologica* **105**, 1494–1506 (2020).
- 280. Burns, D. M. *et al.* Memory B-cell reconstitution following allogeneic hematopoietic stem cell transplantation is an EBV-associated transformation event. *Blood* **126**, 2665–2675 (2015).
- 281. Maloney, D. G. *et al.* IDEC-C2B8 (Rituximab) Anti-CD20 Monoclonal Antibody Therapy in Patients With Relapsed Low-Grade Non-Hodgkin’s Lymphoma. *Blood* **90**, 2188–2195 (1997).
- 282. Tobinai, K. *et al.* Feasibility and pharmacokinetic study of a chimeric anti-CD20 monoclonal antibody (IDEC-C2B8, rituximab) in relapsed B-cell lymphoma. *Annals of Oncology* **9**, 527–534 (1998).
- 283. Breedveld, F. *et al.* Rituximab pharmacokinetics in patients with rheumatoid arthritis: B-cell levels do not correlate with clinical response. *Journal of Clinical Pharmacology* **47**, 1119–1128 (2007).
- 284. Bensalem, A. *et al.* CD4+ count-dependent concentration–effect relationship of rituximab in rheumatoid arthritis. *British Journal of Clinical Pharmacology* **85**, 2747–2758 (2019).
- 285. Edlund, H., Melin, J., Parra-Guillen, Z. P. & Kloft, C. Pharmacokinetics and Pharmacokinetic–Pharmacodynamic Relationships of Monoclonal Antibodies in Children. *Clinical Pharmacokinetics* **54**, 35–80 (2015).
- 286. Defilipp, Z. *et al.* Monitoring the kinetics of B-cell recovery following rituximab may guide the management of steroid-refractory chronic GvHD. *Bone Marrow Transplantation* **51**, 607–609 (2016).

- 287. Sarantopoulos, S. *et al.* Recovery of B-cell homeostasis after rituximab in chronic graft-versus-host disease. *Blood* **117**, 2275–2283 (2011).
- 288. Carpenter, B. *et al.* Incidence and dynamics of epstein-barr virus reactivation after alemtuzumab-based conditioning for allogeneic hematopoietic stem-cell transplantation. *Transplantation* **90**, 564–570 (2010).
- 289. Salas, M. Q. *et al.* High incidence but low mortality of EBV-reactivation and PTLN after alloHCT using ATG and PTCy for GVHD prophylaxis. *Leukemia and Lymphoma* **61**, 3198–3208 (2020).
- 290. Servais, S. *et al.* Long-term immune reconstitution and infection burden after mismatched hematopoietic stem cell transplantation. *Biology of Blood and Marrow Transplantation* **20**, 507–517 (2014).
- 291. Bejanyan, N. *et al.* Delayed immune reconstitution after allogeneic transplantation increases the risks of mortality and chronic GVHD. *Blood Advances* **2**, 909–922 (2018).
- 292. Curtis, R. E. *et al.* Risk of lymphoproliferative disorders after bone marrow transplantation: A multi-institutional study. *Blood* **94**, 2208–2216 (1999).
- 293. Kinzel, M. *et al.* Risk Factors for the Incidence of and the Mortality due to Post-Transplant Lymphoproliferative Disorder after Hematopoietic Cell Transplantation. *Transplantation and Cellular Therapy* **28**, 53.e1–53.e10 (2022).
- 294. Gordan, L. N. *et al.* Phase II trial of individualized rituximab dosing for patients with CD20-positive lymphoproliferative disorders. *Journal of Clinical Oncology* **23**, 1096–1102 (2005).
- 295. Ho, D. D. *et al.* Rapid turnover of plasma virions and CD4 lymphocytes in HIV-1 infection. *Nature* **373**, 123–126 (1995).
- 296. Nowak, M. A. & Bangham, C. R. M. Population dynamics of immune responses to persistent viruses. *Science* **272**, 74–79 (1996).
- 297. Perelson, A. S., Neumann, A. U., Markowitz, M., Leonard, J. M. & Ho, D. D. HIV-1 dynamics in vivo: Virion clearance rate, infected cell life-span, and viral generation time. *Science* **271**, 1582–1586 (1996).
- 298. Asquith, B. & Bangham, C. R. M. Quantifying HTLV-I dynamics. *Immunology and Cell Biology* **85**, 280–286 (2007).
- 299. Neumann, A. U. *et al.* Hepatitis C viral dynamics in vivo and the antiviral efficacy of interferon- $\alpha$  therapy. *Science* **282**, 103–107 (1998).

- 300. Guedj, J., Dahari, H., Pohl, R. T., Ferenci, P. & Perelson, A. S. Understanding silibinin's modes of action against HCV using viral kinetic modeling. *Journal of Hepatology* **56**, 1019–1024 (2012).
- 301. Kepler, G. M., Banks, H. T., Davidian, M. & Rosenberg, E. S. A model for HCMV infection in immunosuppressed patients. *Mathematical and Computer Modelling* **49**, 1653–1663 (2009).
- 302. Gastine, S. *et al.* Systematic Review and Patient-Level Meta-Analysis of SARS-CoV-2 Viral Dynamics to Model Response to Antiviral Therapies. *Clinical Pharmacology and Therapeutics* **110**, 321–333 (2021).
- 303. Gonçalves, A. *et al.* Timing of Antiviral Treatment Initiation is Critical to Reduce SARS-CoV-2 Viral Load. *CPT: Pharmacometrics & Systems Pharmacology* **9**, 509–514 (2020).
- 304. De Boer, R. J. & Perelson, A. S. Target cell limited and immune control models of HIV infection: A comparison. *Journal of Theoretical Biology* **190**, 201–214 (1998).
- 305. Parra-Guillen, Z. P. *et al.* Mechanistic Modeling of a Novel Oncolytic Virus, V937, to Describe Viral Kinetic and Dynamic Processes Following Intratumoral and Intravenous Administration. *Frontiers in Pharmacology* **12**, 1–13 (2021).
- 306. Powers, K. A. *et al.* Modeling viral and drug kinetics: Hepatitis C virus treatment with pegylated interferon alfa-2b. *Seminars in Liver Disease* **23**, 13–18 (2003).
- 307. Talal, A. H. *et al.* Pharmacodynamics of PEG-IFN Alpha Differentiate HIV/HCV Coinfected Sustained Virological Responders from Nonresponders. *Hepatology* **43**, 943–953 (2006).
- 308. Nguyen, T. H. T., Mentré, F., Levi, M., Yu, J. & Guedj, J. Pharmacokinetic-viral kinetic model describes the effect of alisporivir as monotherapy or in combination with peg-IFN on Hepatitis C virologic response. *Clinical Pharmacology and Therapeutics* **96**, 599–608 (2014).
- 309. Duca, K. A. *et al.* A virtual look at Epstein-Barr virus infection: Biological interpretations. *PLoS Pathogens* **3**, 1388–1400 (2007).
- 310. Shapiro, M. *et al.* A virtual look at Epstein-Barr virus infection: Simulation mechanism. *Journal of Theoretical Biology* **252**, 633–648 (2008).
- 311. Yu, J. S. & Bagheri, N. Multi-class and multi-scale models of complex biological phenomena. *Current Opinion in Biotechnology* **39**, 167–173 (2016).
- 312. Delgado-Eckert, E. & Shapiro, M. A model of host response to a multi-stage pathogen. *Journal of Mathematical Biology* **63**, 201–227 (2011).
- 313. Hawkins, J. B., Delgado-Eckert, E., Thorley-Lawson, D. A. & Shapiro, M. The Cycle of EBV Infection Explains Persistence, the Sizes of the Infected Cell Populations and Which Come under CTL Regulation. *PLoS Pathogens* **9**, (2013).

314. Castiglione, F. *et al.* Simulating Epstein-Barr virus infection with C-ImmSim. *Bioinformatics* **23**, 1371–1377 (2007).
315. Huynh, G. T., Adler, F. R., Huynh, G. T. & Adler, F. R. Alternating Host Cell Tropism Shapes the Persistence, Evolution and Coexistence of Epstein-Barr Virus Infections in Human. *Bull Math Biol* **73**, 1754–1773 (2011).
316. Huynh, G. T. & Adler, F. R. Mathematical modelling the age dependence of Epstein-Barr virus associated infectious mononucleosis. *Mathematical Medicine and Biology* **29**, 245–261 (2012).
317. Hadinoto, V., Shapiro, M., Sun, C. C. & Thorley-Lawson, D. A. The dynamics of EBV shedding implicate a central role for epithelial cells in amplifying viral output. *PLoS Pathogens* **5**, (2009).
318. Huynh, G. T. & Rong, L. Modeling the dynamics of virus shedding into the saliva of Epstein-Barr virus positive individuals. *Journal of Theoretical Biology* **310**, 105–114 (2012).
319. Byrne, C. M. *et al.* Examining the dynamics of Epstein-Barr virus shedding in the tonsils and the impact of HIV-1 coinfection on daily saliva viral loads. *PLoS Computational Biology* **17**, 1–25 (2021).
320. Akinwumi, S. M. Modeling the Kinetics of EBV in Primary Carriers and Transplant Recipients by Segun M . Akinwumi A thesis submitted in partial fulfillment of the requirements for the degree of Doctor of Philosophy in Applied Mathematics Department of Mathematical and Sta. (2017).
321. Admiraal, R. *et al.* Early CD4+ Immune Reconstitution Predicts Probability of Relapse in Pediatric AML after Unrelated Cord Blood Transplantation: Importance of Preventing in Vivo T-Cell Depletion Using Thymoglobulin®. *Biology of Blood and Marrow Transplantation* **21**, 271 (2015).
322. Koning, C. de *et al.* CD4+ T-cell reconstitution predicts survival outcomes after acute graft-versus-host-disease: a dual-center validation. *Blood* **137**, 848–855 (2021).
323. Roughan, J. E., Torgbor, C. & Thorley-Lawson, D. A. Germinal Center B Cells Latently Infected with Epstein-Barr Virus Proliferate Extensively but Do Not Increase in Number. *Journal of Virology* **84**, 1158–1168 (2010).
324. Wang, Y. *et al.* Viral dynamics model with CTL immune response incorporating antiretroviral therapy. *J. Math. Biol* **67**, 901–934 (2013).
325. Hochberg, D. *et al.* Acute Infection with Epstein-Barr Virus Targets and Overwhelms the Peripheral Memory B-Cell Compartment with Resting, Latently Infected Cells. *Journal of Virology* **78**, 5194–5204 (2004).

- 326. Ballen, K. K. ATG for cord blood transplant: Yes or no? *Blood* **123**, 7–8 (2014).
- 327. Lindsay, J. *et al.* Dynamics of Epstein–Barr virus on post-transplant lymphoproliferative disorders after antithymocyte globulin-conditioned allogeneic hematopoietic cell transplant. *Transplant Infectious Disease* **23**, 1–10 (2021).
- 328. Uhlin, M. *et al.* Risk factors for Epstein-Barr virus-related post-transplant lymphoproliferative disease after allogeneic hematopoietic stem cell transplantation. *Haematologica* **99**, 346–352 (2014).
- 329. Bonong, P. R. E. *et al.* Risk factors for post-transplant Epstein-Barr virus events in pediatric recipients of hematopoietic stem cell transplants. *Pediatric Transplantation* **25**, 1–14 (2021).
- 330. Van Esser, J. W. J. *et al.* Prevention of Epstein-Barr virus-lymphoproliferative disease by molecular monitoring and preemptive rituximab in high-risk patients after allogeneic stem cell transplantation. *Blood* **99**, 4364–4369 (2002).
- 331. Burns, D. M. *et al.* Greatly reduced risk of EBV reactivation in rituximab-experienced recipients of alemtuzumab-conditioned allogeneic HSCT. *Bone Marrow Transplantation* **51**, 825–832 (2016).
- 332. Preemptive Therapy of EBV-Related Lymphoproliferative Disease after Pediatric Haploidentical Stem Cell Transplantation. *American Journal of Transplantation* **7**, 1648–1655 (2007).
- 333. Wei, N., Wang, Y., Wang, J., Wu, L. & Wang, Z. Characteristics of Epstein–Barr virus reactivation after allogeneic haematopoietic stem cell transplantation in patients with chronic active Epstein–Barr virus disease: favorable responses to rituximab. *Bone Marrow Transplantation* **56**, 1449–1451 (2021).
- 334. Dumas, P. Y. *et al.* Incidence and risk factors of EBV reactivation after unrelated cord blood transplantation: A Eurocord and Société Française de Greffe de Moelle-Thérapie Cellulaire collaborative study. *Bone Marrow Transplantation* **48**, 253–256 (2013).
- 335. Alexandersson, A. *et al.* Viral infections and immune reconstitution interaction after pediatric allogeneic hematopoietic stem cell transplantation. *Infectious Diseases* **51**, 772–778 (2019).
- 336. Kinch, A. *et al.* Long-term outcome of Epstein–Barr virus DNAemia and PTLTD with the use of preemptive rituximab following allogeneic HSCT. *Leukemia & Lymphoma* **59**, 1172–1179 (2018).
- 337. Düver, F. *et al.* Viral reactivations following hematopoietic stem cell transplantation in pediatric patients - A single center 11-year analysis. *PLoS ONE* **15**, (2020).
- 338. Orentas, R. J. *et al.* Monitoring and modulation of Epstein-Barr virus loads in pediatric transplant patients. *Pediatric Transplantation* **7**, 305–314 (2003).

339. Duke, E. R., Boshier, F. A. T., Boeckh, M., Schiffer, J. T. & Cardozo-Ojeda, E. F. Mathematical modeling of within-host, untreated, cytomegalovirus infection dynamics after allogeneic transplantation. *Viruses* **13**, (2021).
340. Smets, F. *et al.* Ratio between Epstein-Barr viral load and anti-Epstein-Barr virus specific T-cell response as a predictive marker of posttransplant lymphoproliferative disease. *Transplantation* **73**, 1603–1610 (2002).
341. Heslop, H. E. *et al.* Long-term outcome of EBV-specific T-cell infusions to prevent or treat EBV-related lymphoproliferative disease in transplant recipients. *Blood* **115**, 925–935 (2010).
342. Long, H. M., Meckiff, B. J. & Taylor, G. S. The T-cell Response to Epstein-Barr Virus—New Tricks From an Old Dog. *Frontiers in Immunology* **10**, 1–11 (2019).
343. Prockop, S. *et al.* Off-the-shelf EBV-specific T cell immunotherapy for rituximab-refractory EBV-associated lymphoma following transplantation. *Journal of Clinical Investigation* **130**, 733–747 (2020).
344. Margetts, B. K. Monitoring Viral Infections & Immune Repertoires in Transplanted Children : A Statistical Approach. (2019).
345. Hoshino, Y. *et al.* Long-Term Administration of Valacyclovir Reduces the Number of Epstein-Barr Virus (EBV)-Infected B Cells but Not the Number of EBV DNA Copies per B Cell in Healthy Volunteers. *Journal of Virology* **83**, 11857–11861 (2009).
346. G. A., F., R., G. & H. H., H. Viral dynamics in transplant patients: implications for disease. *Lancet Infectious Diseases* **7**, 460–472 (2007).
347. Gustafsson, Å. *et al.* Epstein-Barr virus (EBV) load in bone marrow transplant recipients at risk to develop posttransplant lymphoproliferative disease: Prophylactic infusion of EBV-specific cytotoxic T cells. *Blood* **95**, 807–814 (2000).
348. Wang, W. Y. *et al.* Plasma EBV DNA clearance rate as a novel prognostic marker for metastatic/recurrent nasopharyngeal carcinoma. *Clinical Cancer Research* **16**, 1016–1024 (2010).
349. Yates, A. *et al.* Revisiting estimates of CTL killing rates in vivo. *PLoS ONE* **2**, (2007).
350. Asquith, B. *et al.* A functional CD8+ cell assay reveals individual variation in CD8+ cell antiviral efficacy and explains differences in human T-lymphotropic virus type 1 proviral load. *Journal of General Virology* **86**, 1515–1523 (2005).
351. Klenerman, P. *et al.* Cytotoxic T lymphocytes and viral turnover in HIV type 1 infection. *Proceedings of the National Academy of Sciences of the United States of America* **93**, 15323–15328 (1996).



352. Hadinoto, V. *et al.* On the dynamics of acute EBV infection and the pathogenesis of infectious mononucleosis. *Blood* **111**, 1420–1427 (2008).
353. Zhu, C. B. *et al.* Outcome of Rituximab-Based Treatment for Post-Transplant Lymphoproliferative Disorder After Allogeneic Hematopoietic Stem Cell Transplantation: A Single-Center Experience 2380 4 2 42.© *Ann Transplant* **24**, 175–184 (2019).
354. Pukownik, E. *et al.* Impact of CMV and EBV on immune recovery after allogeneic hematopoietic cell transplantation in children. *Anticancer Research* **38**, 6009–6013 (2018).
355. Mould, D. & Upton, R. Basic Concepts in Population Modeling, Simulation, and Model-Based Drug Development—Part 2: Introduction to Pharmacokinetic Modeling Methods. *CPT: Pharmacometrics and Systems Pharmacology* 1–14 (2013).doi:10.1038/psp.2013.14
356. FDA The US Food and Drug Administration. Biosimilar Product Information - FDA Approved Biosimilar Products. (2022).at <<https://www.fda.gov/drugs/biosimilars/biosimilar-product-information>>
357. EMA European Medicines Agency. Medicines - Centrally authorised biosimilar medicines. (2022).at <<https://www.ema.europa.eu/en/human-regulatory/overview/biosimilar-medicines-overview>>
358. EMA Biosimilars in the EU - Information guide for healthcare professionals. *European Medicines Agency* 1–40 (2019).at <[https://www.ema.europa.eu/en/documents/leaflet/biosimilars-eu-information-guide-healthcare-professionals%7B/\\_%7Den.pdf](https://www.ema.europa.eu/en/documents/leaflet/biosimilars-eu-information-guide-healthcare-professionals%7B/_%7Den.pdf)>
359. Barbier, L. *et al.* The Efficacy, Safety, and Immunogenicity of Switching Between Reference Biopharmaceuticals and Biosimilars: A Systematic Review. *Clinical Pharmacology and Therapeutics* **108**, 734–755 (2020).
360. Center for Drug Evaluation and Research (CDER), (CBER), C. for B. E. & Research *Considerations in Demonstrating Interchangeability With a Reference Product-Guidance for Industry.* 1–20 (2019).at <<https://www.fda.gov/Drugs/GuidanceComplianceRegulatoryInformation/Guidances/default.htm>and/or<https://www.fda.gov/BiologicsBloodVaccines/GuidanceComplianceRegulatoryInformation/Guidances/default.htm>>
361. Nava-Parada, P., Shelbaya, A. & Nabhan, C. Rituximab biosimilars in hematologic malignancies: The need for a real-world approach. *Future Oncology* **16**, 2017–2027 (2020).
362. Cheesman, S. Introduction of Biosimilar Rituximab: A Hospital Perspective. *HemaSphere* E515 (2021).doi:10.1097/HS9.0000000000000515

- 363. Park, W. *et al.* Efficacy and Safety of Switching from Innovator Rituximab to Biosimilar CT-P10 Compared with Continued Treatment with CT-P10: Results of a 56-Week Open-Label Study in Patients with Rheumatoid Arthritis. *BioDrugs* **31**, 369–377 (2017).
- 364. Shim, S. C. *et al.* Efficacy and safety of switching from rituximab to biosimilar CT-P10 in rheumatoid arthritis: 72-week data from a randomized Phase 3 trial. *Rheumatology (United Kingdom)* **58**, 2193–2202 (2019).
- 365. Tony, H. P. *et al.* Brief Report: Safety and Immunogenicity of Rituximab Biosimilar GP 2013 After Switch From Reference Rituximab in Patients With Active Rheumatoid Arthritis. *Arthritis Care and Research* **71**, 88–94 (2019).
- 366. Urru, S. A. M., Spila Alegiani, S., Guella, A., Traversa, G. & Campomori, A. Safety of switching between rituximab biosimilars in onco-hematology. *Scientific Reports* **11**, 1–5 (2021).
- 367. Cohen, S. B. *et al.* Extension Study of PF-05280586, a Potential Rituximab Biosimilar, Versus Rituximab in Subjects With Active Rheumatoid Arthritis. *Arthritis Care and Research* **70**, 1598–0606 (2018).
- 368. Burmester, G. *et al.* A Randomized, Double-Blind Study Comparing Pharmacokinetics and Pharmacodynamics of Proposed Biosimilar ABP 798 With Rituximab Reference Product in Subjects With Moderate to Severe Rheumatoid Arthritis. *Clinical Pharmacology in Drug Development* **9**, 1003–1014 (2020).
- 369. Otremba, B., Borchardt, J., Kuske, A., Hollnagel-Schmitz, M. & Losch, F. O. Real-world use and acceptance of rituximab biosimilars in non-Hodgkin lymphoma in an oncologist network in Germany. *Future Oncology* **16**, 1001–1012 (2020).
- 370. Melville, A. R. *et al.* Real-world experience of effectiveness of non-medical switch from originator to biosimilar rituximab in rheumatoid arthritis. *Rheumatology (Oxford, England)* **60**, 3679–3688 (2021).
- 371. Deng, W. *et al.* Rituximab biosimilar HLX01 versus reference rituximab in the treatment of diffuse large B-cell lymphoma: Real-world clinical experience. *Journal of Oncology Pharmacy Practice* (2022).doi:10.1177/10781552221110470
- 372. Riva, N. *et al.* Intensive Safety Monitoring of Rituximab (Biosimilar Novex® and the Innovator) in Pediatric Patients With Complex Diseases. *Frontiers in Pharmacology* **12**, 1–14 (2022).
- 373. Roy, P. S. *et al.* Comparison of the efficacy and safety of Rituximab (Mabthera™) and its biosimilar (Reditux™) in diffuse large B-cell lymphoma patients treated with chemotherapy: A retrospective analysis. *Indian Journal of Medical and Paediatric Oncology* **34**, 292–298 (2013).

- 374. Jurczak, W. *et al.* Rituximab biosimilar and reference rituximab in patients with previously untreated advanced follicular lymphoma (ASSIST-FL): primary results from a confirmatory phase 3, double-blind, randomised, controlled study. *The Lancet Haematology* **4**, e350–e361 (2017).
- 375. Kim, W. S. *et al.* Efficacy, pharmacokinetics, and safety of the biosimilar CT-P10 compared with rituximab in patients with previously untreated advanced-stage follicular lymphoma: a randomised, double-blind, parallel-group, non-inferiority phase 3 trial. *The Lancet Haematology* **4**, e362–e373 (2017).
- 376. Ogura, M. *et al.* Efficacy, pharmacokinetics, and safety of the biosimilar CT-P10 in comparison with rituximab in patients with previously untreated low-tumour-burden follicular lymphoma: a randomised, double-blind, parallel-group, phase 3 trial. *The Lancet Haematology* **5**, e543–e553 (2018).
- 377. Jiang, B. *et al.* Pharmacokinetics and safety of IBI301 versus rituximab in patients with CD20+ B-cell lymphoma: a multicenter, randomized, double-blind, parallel-controlled study. *Scientific Reports* **10**, 1–9 (2020).
- 378. Song, Y., Wang, J., Wang, Y. & Wang, Z. Ruxolitinib in Patients With Chronic Active Epstein-Barr Virus Infection: A Retrospective, Single-Center Study. *Frontiers in Pharmacology* **12**, 1–7 (2021).
- 379. Menon, H. *et al.* Pharmacokinetic and Pharmacodynamic Properties of a Biosimilar Rituximab (Reditux®) Are Identical to the Innovator Brand MabThera®– Experience from a Tertiary Cancer Centre in Western India. *Blood* **124**, 2246–2246 (2014).
- 380. Gota, V. *et al.* Population pharmacokinetics of Reditux™, a biosimilar Rituximab, in diffuse large B-cell lymphoma. *Cancer Chemotherapy and Pharmacology* **78**, 353–359 (2016).
- 381. Candelaria, M. *et al.* Comparative assessment of pharmacokinetics, and pharmacodynamics between RTX83™, a rituximab biosimilar, and rituximab in diffuse large B-cell lymphoma patients: a population PK model approach. *Cancer Chemotherapy and Pharmacology* **81**, 515–527 (2018).